

**University of Miami
Scholarly Repository**

Open Access Dissertations

Electronic Theses and Dissertations

2015-11-09

Identification and Tracking of Coherent Agulhas Current Rings

Yan Wang

University of Miami, ywang.nt@gmail.com

Follow this and additional works at: https://scholarlyrepository.miami.edu/oa_dissertations

Recommended Citation

Wang, Yan, "Identification and Tracking of Coherent Agulhas Current Rings" (2015). *Open Access Dissertations*. 1528.
https://scholarlyrepository.miami.edu/oa_dissertations/1528

This Open access is brought to you for free and open access by the Electronic Theses and Dissertations at Scholarly Repository. It has been accepted for inclusion in Open Access Dissertations by an authorized administrator of Scholarly Repository. For more information, please contact repository.library@miami.edu.

UNIVERSITY OF MIAMI

IDENTIFICATION AND TRACKING OF COHERENT AGULHAS CURRENT
RINGS

By

Yan Wang

A DISSERTATION

Submitted to the Faculty
of the University of Miami
in partial fulfillment of the requirements for
the degree of Doctor of Philosophy

Coral Gables, Florida

December 2015

©2015
Yan Wang
All Rights Reserved

UNIVERSITY OF MIAMI

A dissertation submitted in partial fulfillment of
the requirements for the degree of
Doctor of Philosophy

IDENTIFICATION AND TRACKING OF COHERENT AGULHAS CURRENT
RINGS

Yan Wang

Approved:

Maria J. Olascoaga, Ph.D.
Associate Professor of Applied Marine Physics

Francisco J. Beron-Vera, Ph.D.
Research Associate Professor of Applied Marine Physics

Michael G. Brown, Ph.D.
Professor of Applied Marine Physics

Lisa M. Beal, Ph.D.
Professor of Meteorology and Physical Oceanography

Gustavo J. Goni, Ph.D.
Oceanographer
National Oceanic and Atmospheric Administration
Miami, Florida

Dean of the Graduate School

WANG, YAN
Identification and Tracking of Coherent
Agulhas Current Rings

(Ph.D., Applied Marine Physics)
(December 2015)

Abstract of a dissertation at the University of Miami.

Dissertation supervised by Professor Maria J. Olascoaga.
No. of pages in text. (105)

Recent advancements in nonlinear dynamical systems theory have led to the development of a methodology, called geodesic eddy detection, for the objective (i.e., frame-independent) framing and tracking of coherent Lagrangian eddies in two-dimensional unsteady flows. Such eddies have material boundaries that do not stretch or fold over long periods of time, thereby providing an explicit mechanism of transport of fluid and distinguished properties, such as temperature and salinity. Eddies identified from Eulerian criteria (e.g., as regions enclosed by streamlines where rotation dominates over strain instantaneously) do not possess this property as such criteria either depend on the choice of reference frame or fail to reveal long-term material response of the flow field. Applying geodesic eddy detection on surface currents derived from the over two-decade-long record of satellite altimetry measurements, we isolated coherent Lagrangian Agulhas Current rings capable of traversing the South Atlantic basin with no noticeable signs of filamentation. The rings are found to acquire material coherence from incoherent fluid away from the Agulhas retroflection region in the South Atlantic, revealing that their genesis mechanism differs substantially from the commonly accepted picture in which rings are shed from the Agulhas retroflection as a result of occasional occlusions. While ability of Agulhas rings in transporting fluid over long

distances is confirmed, this is found to be more restricted than suggested by earlier assessments. First, coherent transport estimates are found to be small compared to estimates from Eulerian analysis. The reason for this is that Eulerian analysis significantly overestimates the volume of the coherently transported fluid. Second, the coherent transport estimates are smaller than the total Agulhas leakage reported in numerical studies. These conclusions remain unaltered by the discovery that Agulhas rings can be shielded by Atlantic Ocean water as a result of successive short-term material coherence regain events. In fact, while the volume of fluid trapped by these short-term shields is larger than that from a long-term material coherence assessment, the fraction of such volume traceable into the Indian Ocean is in general rather small.

To my parents.

Acknowledgments

I would like to thank my mentors, Josefina Olascoaga and Javier Beron-Vera, for introducing me to the field of Lagrangian ocean dynamics. Their endless support and inspiration have helped me through. I am sincerely grateful to my committee, Mike Brown, Lisa Beal, and Gustavo Goni, for stimulating me to think beyond the horizon. This thesis has been made possible thanks to support from NSF grant CMG0825547 and NASA grant NNX10AE99G.

YAN WANG

University of Miami

December 2015

Contents

List of Figures	viii
List of Tables	xviii
CHAPTER 1 Introduction	1
1.1 Mesoscale eddies and the Agulhas Current rings	1
1.2 Traditional eddy detection methods	5
1.3 Geodesic eddy detection	7
1.4 Organization	8
CHAPTER 2 Objective eddy detection	10
2.1 Background	10
2.2 The issue with Eulerian eddy detection	14
2.3 Objective Lagrangian eddy detection	18
2.3.1 Mathematical Setup	18
2.3.2 Eddy boundaries as extremum curves of absolute deformation .	22
2.3.3 Eddy boundaries as stationary curves of relative deformation .	28
2.3.4 Equivalence of the two formulations in the incompressible case	35
CHAPTER 3 Objective detection of Agulhas rings	36

3.1	Overview	36
3.2	Background	36
3.3	Methodology	40
3.3.1	Dynamical systems setup	40
3.3.2	Transport barriers as geodesics	41
3.3.3	Shear barriers	45
3.3.4	Eddy boundaries	46
3.3.5	Velocity data	47
3.3.6	Numerical implementation	48
3.3.7	Numerical details	49
3.4	Results	50
3.5	Concluding remarks	62
CHAPTER 4 Coherent transport across the South Atlantic		64
4.1	Overview	64
4.2	Background	65
4.3	Methodology	67
4.4	Results	71
4.5	Concluding remarks	81
CHAPTER 5 Life cycle of a material Agulhas Current ring		83
5.1	Overview	83
5.2	Background	83
5.3	Methodology	85
5.4	Preliminary results	87
5.5	Concluding remarks	94

CHAPTER 6 Conclusions **96**

Bibliography **99**

List of Figures

1.1	A plankton bloom trapped inside an eddy in the Drake passage captured by SeaWiFS. Image provided by the SeaWiFS Project, NASA/Goddard Space Flight Center, and ORBIMAGE.	2
1.2	A snapshot of near-surface speeds around Africa in a high-resolution model nested in a global, coarse-resolution model. From A. Biastoch, <i>Modelling the Agulhas Current and Its Coupling with the Atlantic Circulation</i> (presentation file).	3
2.1	Eddy structures in nature. (a) A vortex in the north pole of Saturn's weather layer captured by NASA's Cassini spacecraft in November 2012 (NASA/JPL). (b) Jupiter's Great Red Spot captured by NASA's Voyager 1 in February 1979 (NASA/JPL). (c) Tropical storm Halong in the western Pacific captured by the MODIS on the Terra satellite in July 2002. (d) A plankton bloom trapped within a vortex-like structures in the ocean south of Africa captured by MODIS on NASA's Terra Satellite in December 2011.	11
2.2	The topology of a center and a KAM torus in classical dynamical systems theory . From Haller [2014].	13

2.3	(top) Evolution of a passive tracer initialized within a closed streamline of the wave field with instantaneous streamlines overlaid, (middle) streamlines of the same wave field observed in a reference frame co-moving with it, and (bottom) evolution of a passive tracer initialized inside and outside the transport barrier inferred from the moving reference frame and advected by the original wave field.	16
2.4	(top) A planar unsteady velocity field identified as an eddy by most Eulerian criteria. By being transformed into a frame in which the flow becomes steady, however, the velocity field exhibit a steady saddle flow with no closed transport barriers. Top panel adopted from Haller [2005]. (bottom) A blob of passive tracer initialized within the innermost closed streamline is not trapped inside but continuously stretched by the flow over time. Bottom panel credit Francisco J. Beron-Vera. . .	17
2.5	Evolution of a material curve under the flow map in phase space.	19
2.6	Evolution of an infinitesimal perturbation to a fluid particle trajectory. .	20
2.7	The geometrical meaning of the eigenvalues and eigenvectors of the Cauchy-Green Strain tensor	21
2.8	Minimal stretching property for a closed transport barrier (a KAM curve) in a two-dimensional temporally time T -periodic flow, for large enough iteration numbers of the Poincare map. Note that fixed-endpoint perturbations to the curve γ_0 stretch longer than γ_{nT} , whether or not they were initially longer than γ_0 . From Haller and Beron-Vera [2012].	23

2.9 (left) A material line γ_0 of initial condition in a two-dimensional dynamical system, with the unit normal vector n_0 and unit tangential vector e_0 at point x_0 on it. (right) The initial curve γ_0 is carried and deformed by the flow map into curve γ_t (x_0 mapped to x_t), with the initial unit normal n_0 transformed into vector $DF_{t_0}^t(x_0)n_0$ ($DF_{t_0}^t(x_0)n_0$ denotes the deformation gradient tensor). The material shear at point x_t , σ , is the projection of $DF_{t_0}^t(x_0)n_0$ onto the unit tangential vector e_t locally.	24
2.10 Schematic of an elliptic transport barrier. A closed shearline γ_{t_0} , computed from flow data over $[t_0, t_0 + T]$ plays the role of a generalized KAM curve. Dashed line indicates a hypothetical translated and rotated position of γ_{t_0} for reference. The advected material line γ_{t_0+T} has the same arclength, and encloses the same area as γ_{t_0} does. From Haller and Beron-Vera [2012].	27
2.11 (left) Typical material belt exhibits inhomogeneity after a finite time interval in unsteady flows due to the sensitivity of initial condition difference across the belt. (right) Exceptional material belts within which material loops stretch by the same factor within a finite time interval, hence exhibiting no leading order variations in material strain across the belt. From Haller and Beron-Vera [2013].	29
2.12 (left) In two dimensional fluid flows, coherent Lagrangian eddies necessarily contain at least one Green-Lagrangian singularity where the Cauchy-Green strain tensor becomes identity matrix. (right) Out of all members of nested λ -loops, the outermost one is defined as the boundary of a coherent Lagrangian eddy	33

3.1 A planar unsteady velocity field identified as an eddy by Eulerian criteria. In an appropriate rotating frame, however, the velocity field becomes a steady saddle flow with no closed transport barriers. From Haller [2005].	38
3.2 A fluid domain at time t_0 , $D(t_0)$, deformed under the flow map, $F_{t_0}^t$: $\mathbf{x}_0 \mapsto \mathbf{x}(t; \mathbf{x}_0, t_0)$, into a domain $D(t)$ at time $t \neq t_0$ along fluid particle trajectories. From Beron-Vera, Wang et al., [2013].	41
3.3 Minimal stretching property of a material curve γ_{t_0} , for times t sufficiently larger than t_0 , in a steady circular shear flow among material curves with the same endpoints, $\hat{\gamma}_{t_0}$ and $\bar{\gamma}_{t_0}$. Note that $\hat{\gamma}_{t_0}$ and $\bar{\gamma}_{t_0}$ stretch longer than γ_t , regardless of whether they are initially shorter or longer than γ_{t_0} . From Beron-Vera, Wang et al., [2013].	42

3.6 Identification of a coherent material eddy boundary on $t_0 = 24$ November 2006 from geodesic eddy detection with detection time scale $T = t - t_0 = 90$ d. Marked in red, the eddy boundary is obtained as an average-geodesic-deviation-minimizing member of a nested family of limit cycles of the Lagrangian shear vector field χ_+ . The full limit cycle family is shown in blue in the upper panel, with grey arrows indicating the χ_+ vector field. The middle panel shows the first return (Poincare) map, $x \mapsto P(x)$, onto a section Σ locally transverse to χ_+ vector field. Dots indicate the fixed points of the Poincare map, $P(x) = x$, corresponding to each of the limit cycles. The bottom panel shows the distribution of the average geodesic deviation over the limit cycles. From Beron-Vera, Wang et al., [2013].	51
3.7 (left) Selected snapshots of the 90-day evolution of fluid inside eddies identified by geodesic eddy detection; (middle left) the method of Chelton et al. [2011b] with $U/c > 1$ over at least 90 days; (middle right) the OkuboWeiss (OW) criterion; and (right) the criterion of Mézic et al. [2010]. From Beron-Vera, Wang et al., [2013].	53
3.8 Selected snapshots of the 540-day evolution of fluid inside (left) a geodesic eddy and (right) an SSH eddy. The instantaneous SSH contour that defines the SSH eddy, which has $U/c > 1$ over at least 540 days, is indicated. From Beron-Vera, Wang et al., [2013].	55

4.3 (left column) Trajectories and (right column) mean translation speeds and diameters of coherent material eddies in the Agulhas corridor as detected from altimetry-derived velocities over 19922013 with lifetimes (top row) 90, (middle row) 180, and (bottom row) 360days. (bottom left) Detection domain (solid rectangle) and the reference section used in the construction of the coherent transport time series of Figure 4.6 (dashed line). Selected bathymetry levels (in km) are indicated in the top left along with two relevant topographic features. From Wang et al. [2015b].	72
4.4 (top) Initial and final positions of an idealized coherent Lagrangian eddy. (bottom) Instantaneous, two-dimensional flux T (red curve) caused by eddy penetration through the dashed line ($\Sigma : x = 5.0$) in top panel over time.	74
4.5 A material eddy detected from $T = 90$ day integration contains an inner 360 day eddy core (red). Fluid (blue) trapped between the outermost 90 day boundary and inner 360 day boundary stays compact for at least 90 days. Over extended time period, however, this part of fluid disperse quickly. While the 360 day eddy core still stays compact, even beyond its integrating time length.	75
4.6 (top) Instantaneous and (bottom) annual average time series of transport produced by 360-day coherent material eddies crossing the reference section indicated by the dashed segment in the bottom left of Figure 4.3. Gray-shaded bar portions correspond to transport of Indian Ocean water trapped inside the eddies. From Wang et al. [2015b].	77

4.7 Snapshots of the long-term evolution of two 360-day coherent material eddies with (left column) typical and (right column) exceptional genesis and demise stages. The boundaries of the eddies while they constitute coherent material eddies are indicated in black. Indicated in red are passive tracers that completely fill these eddies during their coherent material stage. From Wang et al. [2015b].	79
5.1 Monthly positions of an Agulhas ring over more than 2 years. Colored contours denotes the boundaries of coherent sets, going from green to red as time progresses. Blue shading indicates the bathymetric features. From Froyland et al. [2015].	88
5.2 (a) Nested family of coherent Lagrangian eddy boundaries extracted from altimetry-derived velocity by applying geodesic eddy detection on $t_0 = 31$ March 1999 inside the region indicated by a rectangle. Each member of the family has a different Lagrangian coherence time scale T ranging from 30 d (outermost) to 40 d (innermost) in steps of 30 d. Selected isobaths (in km) are indicated in gray. The outset is a blowup of the indicated region. (b–f) Advedted images under the flow (i.e., evolution) of the coherent Lagrangian eddy boundaries in (a) on selected dates. An advected boundary is depicted red when it is within its theoretical Lagrangian coherence horizon and in a blue tone when is beyond it. (g) As a function of longitude, area of the largest domain enclosed by advected boundaries within their theoretical Lagrangian coherence horizon. From Wang et al. [2015a].	90

5.3 (a) Streamlines of the altimetric sea surface height (SSH) field in each rectangular region indicated in Figure 5.2a–f plus the streamline snapshot when no short-term coherence is detectable any more. (b) As a function of longitude, maximum SSH anomaly in each such region. From Wang et al. [2015a].	91
5.4 (a) In blue, selected advected positions of the second-to-outermost material loop in fig:evola, corresponding to the Lagrangian ring boundary with coherence time scale $T = 60$ d detected on 31 March 1999. In red, short-time boundaries detected on the dates the advected loop positions are shown. From 31 March 1999 to 18 February 2001, $T = 30$ d, and from 18 February 2001 to 1 September 2001, $T = 15$ d. (b) Area enclosed by the short-time boundaries as a function of longitude. From Wang et al. [2015a].	93

List of Tables

Chapter 1

Introduction

1.1 Mesoscale eddies and the Agulhas Current rings

A long-standing question in physical oceanography concerns the role of mesoscale eddies in transport. Mesoscale eddies are commonly recognized as swirling bodies of water in the ocean [Robinson, 1983], with horizontal spatial scales between 50 and 300 km and temporal scales ranging from several weeks to years [Chelton et al., 2007; Chelton et al., 2011b]. Such coherent structures are increasingly believed to play a crucial role in transporting mass, heat, salt, carbon dioxide, and other biogeochemical tracers over long distances across the world oceans, profoundly modifying the marine ecosystems, large-scale ocean circulations, and long-term global climate [Dong et al., 2014; Zhang et al., 2014]. Figure 1.1 shows a high concentration of biological tracer trapped and carried by an eddy in the Drake Passage.

A case of particular interest illustrating the significance of oceanic eddy transport is that of Agulhas Current rings, the largest in the world ocean [Olson and Evans, 1986], and their role in carrying the Agulhas leakage over long distances. The Agulhas Current is one of the strongest western boundary currents flowing along the eastern Africa coast driven by the positive curl of wind stress field over the subtropical Indian Ocean [Beal

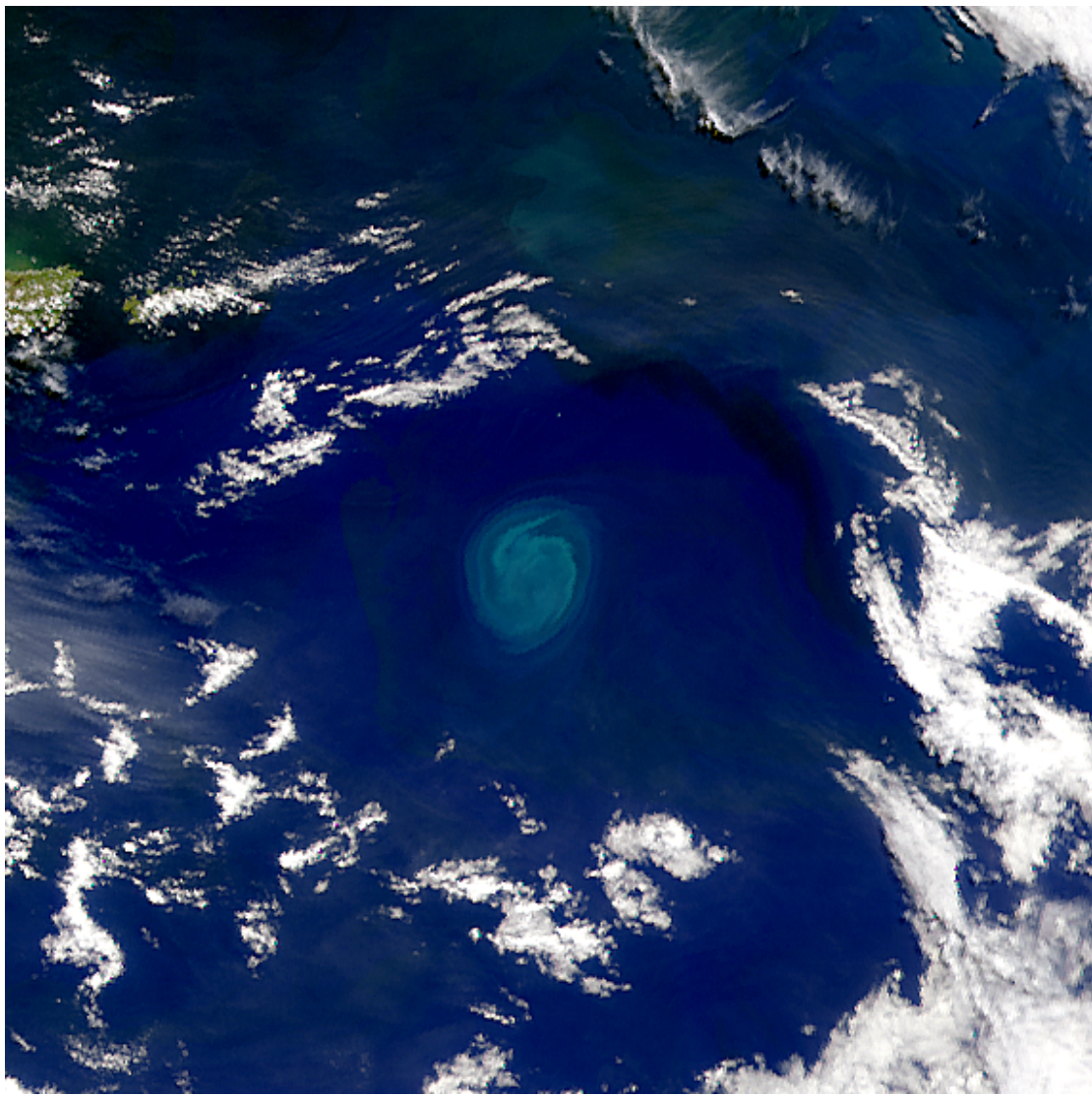


Figure 1.1: A plankton bloom trapped inside an eddy in the Drake passage captured by SeaWiFS. Image provided by the SeaWiFS Project, NASA/Goddard Space Flight Center, and ORBIMAGE.

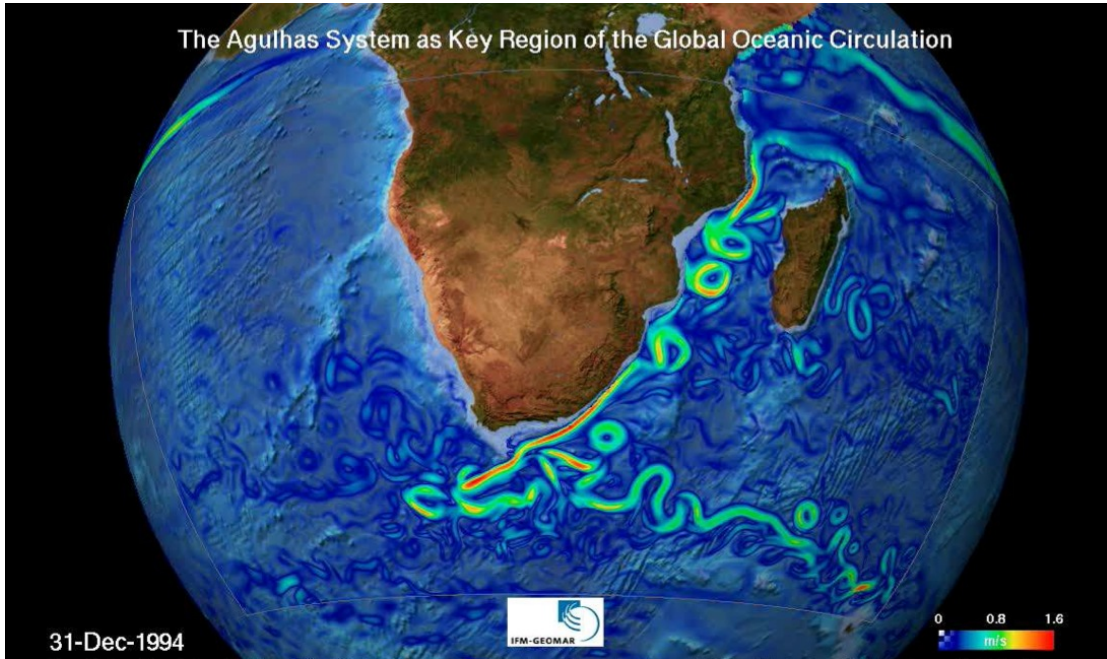


Figure 1.2: A snapshot of near-surface speeds around Africa in a high-resolution model nested in a global, coarse-resolution model. From A. Biastoch, *Modelling the Agulhas Current and Its Coupling with the Atlantic Circulation* (presentation file).

et al., 2011]. Beyond the southern tip of Africa, the current is forced by inertia to overshoot the continental shelf to the latitude where the wind stress curl vanishes [Beal et al., 2011; de Ruijter et al., 1999]. As a result, a substantial part of the current loops back into the Indian Ocean to match the Sverdrup regime far to the east [de Ruijter et al., 1999]. This loop (Figure 1.2), known as the Agulhas Retroflection, is observed to occasionally occlude on itself and shed large anticyclonic eddies, which, along with other forms (e.g., filaments, cyclonic eddies, etc.) of Indian Ocean water intrusion into the South Atlantic, constitute the Agulhas leakage.

With sources of excessive heat and salt from the Indian Ocean, the Agulhas leakage has been suggested to be fundamental in regulating the Atlantic Meridional Overturning Circulation (AMOC) and therefore long-term global climate [Biastoch et al., 2009; Beal et al., 2011]. Gordon [1986] proposes that the Agulhas leakage constitutes the

warm water route of the global overturning circulation systems, and, by carrying large amount of salt, preconditions the Atlantic thermocline water for deep convection, which further stimulates the formation of North Atlantic Deep Water (NADW). Idealized numerical simulations [Weijer et al., 2002] show that northward advection of positive salinity anomalies from the Agulhas Current strengthens the AMOC by increasing the meridional pressure gradient of the Atlantic. Furthermore, due to an apparent poleward shift of the southern hemisphere westerlies [Biastoch et al., 2009], the leakage has been speculated to be increasing, leading to the conjecture that the weakening of AMOC due to continuous accumulation of freshwater around the Arctic region in a warming climate could be mitigated by the leakage [Beal et al., 2011].

The amount of Agulhas leakage carried by Agulhas rings, however, has been highly uncertain. Combining drifter and float data with altimetry record of Schouten et al. [2000], Richardson [2007] proposes that transport by Agulhas rings, which amounts up to 10–13 Sv ($1 \text{ Sv} = 10^6 \text{ m}^3 \text{ s}^{-1}$), forms a large portion of the total leakage, around 15 Sv. This estimate is based on the assumption of fixed annual ring shedding frequency and ring size. Byrne et al. [1995], through tracking satellite altimetric sea surface height (SSH) anomalies, reports that Agulhas rings experience intense amplitude reduction during crossing the South Atlantic basin. The original study of Schouten et al. [2000] also shows that Agulhas rings decay fast within the Cape Basin immediately after shedding events, and that over 60% of initial total ring volume is lost in the South Atlantic. Using numerical simulations, Doglioli et al. [2006] suggest that no more than 15% of the leakage is trapped in rings based on the analysis of spinning characteristics of numerical Lagrangian particles in the Cape Basin. van Sebille et al. [2010] made a more comprehensive analysis in a model and showed that Agulhas rings only trap leakage temporarily in the Agulhas region and experience fast decay within the Cape Basin.

The results from these numerical simulations are supported by Dencausse et al. [2011], who use over 14 years of altimetry SSH observations to conclude that leakage carried by rings decreases from about 8.5 Sv to 1.4 Sv in the Cape Basin due to fast ring decay.

1.2 Traditional eddy detection methods

An important reason for the uncertainty around the ring transport in previous studies is that Agulhas rings are isolated features that change volumes over time. As a result, ring transport is highly dependent on the reference location where transport is evaluated [Dencausse et al., 2011]. Using the initial sizes and shedding frequencies of rings leads to transport values applicable to locations around the Agulhas retroflection only [Richardson, 2007]. Both numerical [van Sebille et al., 2010] and observational [Dencausse et al., 2011] studies show that such values drop significantly as the reference locations are moved westward due to the fast decay and dissipation of rings.

Moreover, most of these previous studies depend on diverse and nonobjective eddy detection methods, namely, the definition of eddy boundaries are chosen ambiguously based on different criteria influenced by the reference frame chosen. Using these criteria to calculate ring transport leads to inaccurate results. This is seen in the study of de Steur et al. [2004], who define three types of ring boundaries, which are: (1) a specific pressure level around a ring, (2) the kinematic separatrix of the streamfunction under a reference frame comoving with a ring, and (3) the maximum density gradient level (corresponding to the maximum swirl velocity) around a ring. Similar eddy boundaries are widely used in observational studies [Olson and Evans, 1986; Goni et al., 1997; Garzoli et al., 1999; Chelton et al., 2007; Chelton et al., 2011b; Dong et al., 2014]. By tracking the local behavior of Lagrangian (i.e., material) tracer in a numerical model, however, de Steur et al. [2004] find that the tracer does not evolve consistently with

these boundaries. We argue that this is not a manifestation of incapability of eddies in trapping fluid, as suggested by the authors, but rather the fact that none of these boundaries are necessarily Lagrangian, and, more importantly, observer independent or objective. Indeed, trapping of fluid parcels by an eddy and any other Lagrangian response of a flow field are objective, which requires that the detection methods able to isolate such responses to be objective as well [Peacock et al., 2015].

The noisy results yielded by most Eulerian eddy detection methods necessitate the use of filtering and threshold parameters. Applying such detection methods to satellite altimetry record, Souza et al. [2011a] report up to 50% variance in the number of eddies detected, dependent on the choice of parameters and filtering methods. This implies that Lagrangian eddy behaviors revealed by Eulerian predictions are highly uncertain. Analysis of spinning characteristics of numerical Lagrangian particles [Doglioli et al., 2006] yields statistical characteristics of an eddy field influenced by eddy splitting, merging, and eddy-eddy interaction processes. The statistical nature of this method also makes it difficult to locate eddy boundaries in a Lagrangian fashion unambiguously.

Recent studies [Zhang et al., 2014; Dong et al., 2014] emphasize that mesoscale eddies transport considerable amounts of mass and heat on a global scale by trapping fluid parcels during migration. Following these results, Agulhas rings may provide an express lane for the Agulhas leakage to the North Brazil Current, given that these rings may cross the South Atlantic basin in less than 3 years [Gordon and Haxby, 1990]. Agulhas leakage transported as such may modulate the stratification of the Atlantic [Weijer et al., 2002] with a faster time scale compared to advection by wind-driven gyres [Rühs et al., 2013]. The goal of this thesis is to identify Agulhas rings capable of trapping Agulhas leakage over long distances across the South Atlantic and quantify the associated mass transport in an objective manner.

1.3 Geodesic eddy detection

To accurately track and quantify the leakage trapped by Agulhas rings, a Lagrangian eddy detection method is crucial. Such a method is provided by *geodesic eddy detection*, a technique rooted in nonlinear dynamical systems theory. The basis for this eddy detection method, provided by Haller and Beron-Vera [2012], is the geodesic theory of transport barriers. Such a theory seeks transport barriers, or Lagrangian Coherent Structures (LCS), as extremum curves of absolute deformation. These curves turn out to be geodesics of the Cauchy-Green strain tensor, an objective measure of deformation. Elliptic LCS, in particular, are closed material lines maximizing the local Lagrangian shear pointwise in an unsteady, two-dimensional flow. Beron-Vera et al. [2012] define Lagrangian eddy boundaries as the outermost member in nested families of closed lines of this type which is most closely shadowed by least-stretching Cauchy-Green geodesics. Eddy boundaries defined as such have the property that their initial arclength is regained in the incompressible flow case. Constancy of arclength and enclosed area preservation renders these boundaries exceptionally coherent: they leave no room for filamentation. Later, Haller and Beron-Vera [2013, 2014] seek elliptic LCS as stationary curves of relative deformation. Such elliptic LCS are also geodesics of a generalized Green-Lagrangian strain tensor, another objective measure of deformation. Particularly, they form the centrepieces of material belts across which averaged material strain does not change at leading order. These very special material lines also resist exponential stretching induced by turbulence. Unlike the previous material lines, they do not necessarily restore their arclength. Coherent Lagrangian eddy boundaries are defined as the outermost members in nested families of curves of this type.

1.4 Organization

The remainder of this thesis contains results from two peer-reviewed articles (Chapters 3 and 4) and a preprint (Chapter 5), preceded by a detailed exposition of the methodology employed (Chapter 2), and followed by general conclusions (Chapter 6). Chapters 3–5 are self-contained, including the essential theory required to understand their content. Chapter 2, which provides mathematical details of geodesic eddy detection, may thus in principle be safely skipped and consulted occasionally if needed for more in depth details.

More specifically, in chapter 3, we apply the geodesic eddy detection in a region of the South Atlantic and compare the results with two other widely used Eulerian eddy diagnostic methods and a recent Lagrangian criterion to highlight the significance of objectivity in quantifying eddy transport. We show that geodesic eddy detection outperforms most contemporary approaches in revealing the true material structures of oceanic eddies that can preserve their coherence for several months. Independent observations (satellite derived chlorophyll) further support our results and suggest that geodesically detected eddies are capable of trapping non-passive tracers in the ocean. This study lays a foundation for objectively quantifying material transport of Agulhas rings over an extended time period.

In chapter 4, we apply the geodesic eddy detection method to the over two-decade-long (1993–2013) satellite altimetry SSH record. Our goal is to determine the role of rings in coherently transporting Agulhas leakage across the South Atlantic. Specifically, by varying the coherence time scale in geodesic eddy detection, we calculate the translational speeds, diameters, and annual detection frequencies of Agulhas rings and determine the relationship of these parameters with ring lifetimes. More importantly,

geodesic eddy detection allows us to track the most robust rings both backward and forward in time, from their stages of genesis to full loss of material coherence. We isolate the rings able to reach the vicinity of the Brazil coast and estimate their potential contribution to the warm water route of the overturning circulation. Gordon and Haxby [1990] proposed that long-lived Agulhas rings may enter the Brazil current system and potentially modify the AMOC by being transported into the northern hemisphere, while Schouten et al. [2000] found that the subtropical gyre is likely to absorb these long-lived features and carry their fluid southward. We will quantitatively test these pathways in this chapter.

Finally, in chapter 5, we present results from a preliminarily study of the life cycle of a material Agulhas ring by applying geodesic eddy detection on a monthly basis as the ring traverses the South Atlantic subtropical gyre. At the time of writing our most relevant finding is that the ring evolves as a quite coherent material entity for a period of about 2 years after the initial coherence is lost upon crossing the Walvis Ridge. This is attributed to the continual development of short-term coherent material boundaries shielding the ring, preventing its interior from being mixed with the ambient turbulent flow. We show that such coherence regaining cannot be inferred from Eulerian analysis. This finding complements the study on the ability of Agulhas rings in transporting fluid across the South Atlantic.

Chapter 2

Objective eddy detection

2.1 Background

Coherent eddies or vortices are ubiquitous in nature (Figure 2.1). Close inspection of such coherent structures lead to the physical assumption that eddies are enclosed by hidden, elliptical or cylindrical material barriers that forbid effective mixing between the eddy interior and ambient flows. For instance, storms in planetary weather layers (Figures 2.1a and 2.1c) are distinguished by locking high momentum and energy. The Great Red Spot (Figure 2.1b), a gigantic vortex within Jupiter's weather layer, contains gases with distinct chemical constitutions that do not seem to mix with the surrounding fluid. Satellite images also constantly capture strong signals of plankton activities confined inside vortex-like features in the ocean (Figure 2.1d). As a result, eddies are often viewed as isolated islands of fluid travelling through an otherwise incoherent flow field [Provenzale, 1999; Haller and Beron-Vera, 2013].

Defining coherent eddy boundaries as closed material lines or surfaces that permit zero volume flux is not optimal, as all material lines, whether closed or not, are like that [Haller and Beron-Vera, 2012]. Like other types of coherent structures, coherent eddies admit distinct expressions in almost all scalar diagnostics of fluid dynamics [Haller,

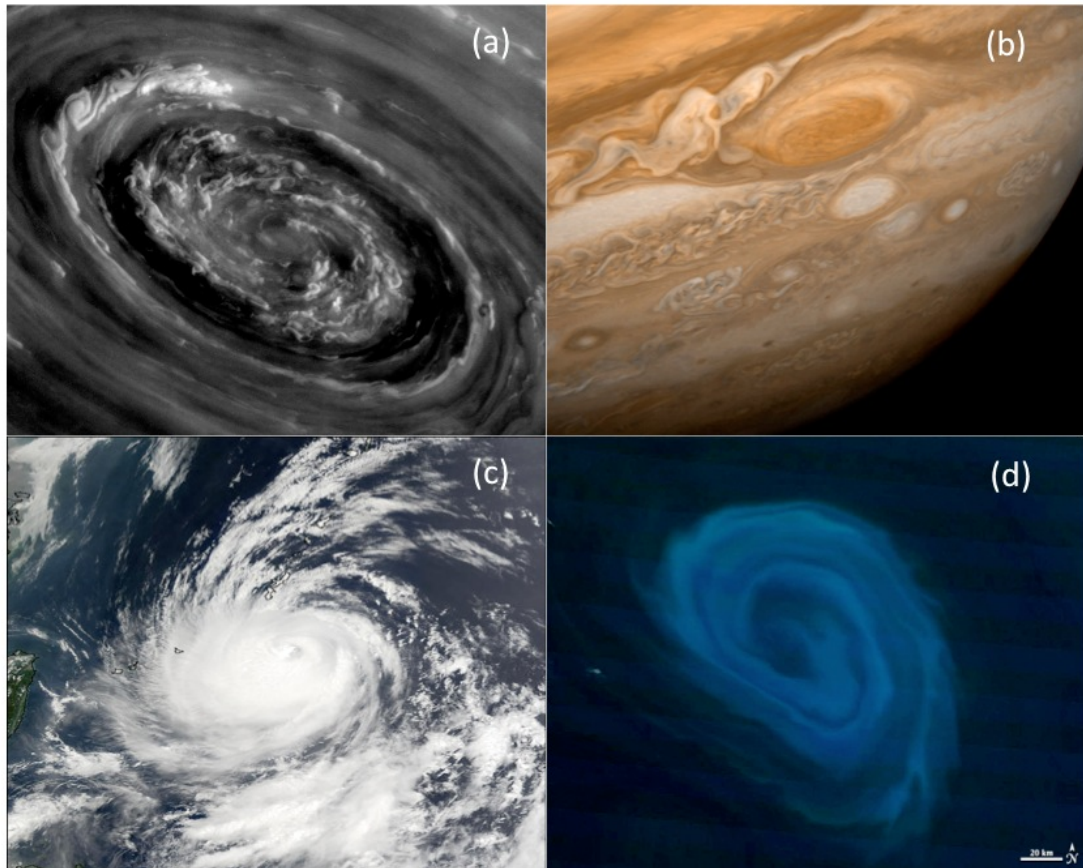


Figure 2.1: Eddy structures in nature. (a) A vortex in the north pole of Saturn's weather layer captured by NASA's Cassini spacecraft in November 2012 (NASA/JPL). (b) Jupiter's Great Red Spot captured by NASA's Voyager 1 in February 1979 (NASA/JPL). (c) Tropical storm Halong in the western Pacific captured by the MODIS on the Terra satellite in July 2002. (d) A plankton bloom trapped within a vortex-like structures in the ocean south of Africa captured by MODIS on NASA's Terra Satellite in December 2011.

2014]. For instance, specific dynamical properties, such as dominant concentration of vorticity have been favored as major characteristics of eddies [McWilliams, 1984; Okubo, 1970; Weiss, 1991; van Sebille et al., 2010]. In the geophysical case, potential vorticity anomalies have been tracked to study oceanic eddies globally [Zhang et al., 2014]. Besides dynamical properties, special geometrical features of velocity field (e.g., closed streamlines) are also observed to reside in coherent eddies [Chelton et al., 2007; Chelton et al., 2011b; Dong et al., 2014]. In turn, such expressions are constantly used to track the motions of coherent eddies and quantify the transport induced by eddy movements.

However, expressions in scalar field do not reveal the hidden barriers that create the coherence of eddies and therefore should be treated as a necessary instead of a sufficient condition for existence of coherent eddies. Indeed, even a simple parallel shear flow admits high concentration of vorticity. Refined criteria based on Eulerian signatures of the eddy field, such as the Okubo-Weiss criterion [Okubo, 1970; Weiss, 1991], which seeks eddy regions with vorticity dominating over shear and strain, may only frame eddy evolution in short term due to the instantaneous nature of Eulerian signatures. A more severer issue associated with such Eulerian eddy detection methods is that their criteria are not objective: Eulerian signatures of a flow field can change dramatically under the change of reference frames [Haller, 2005]. Yet eddy coherence, as a material response of a flow field, should not depend on the choice of reference frame [Haller, 2014; Peacock et al., 2015].

The classical theory of dynamical systems provides a comprehensive characterization of material coherence for analyzing idealized flows. Specifically, closed streamlines around fixed points (i.e., points where velocity vanishes) of *centers* and *KAM curves* (Figure 2.2) constitute the material boundaries of coherent eddies in steady and

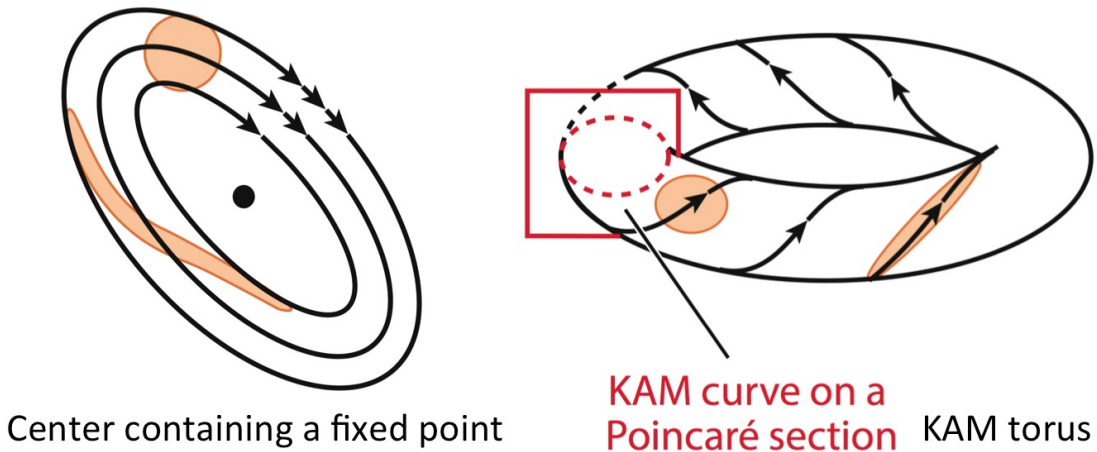


Figure 2.2: The topology of a center and a KAM torus in classical dynamical systems theory . From Haller [2014].

time (quasi)periodic flows. Over infinitely long time, these idealized eddy boundaries, along with other types of recurrent structures (e.g., hyperbolic manifolds and jet currents), dominate tracer patterns and become the root cause of coherence of the entire flow field [Beron-Vera, 2015]. However, those who apply such theoretical tools soon find that recurrent structures are unrealistic in real flows because (1) such flows are highly unsteady, admitting no recurrent structures, and (2) real eddy features do not create permanent coherence. Indeed, no fixed point or KAM curve may exist in oceanic flows. Meanwhile, real eddy features have only finite lifetimes.

The geodesic theory of transport barriers [Haller and Beron-Vera, 2012], on the other hand, provides an objective (i.e., frame-independent) framework for detecting coherent material eddies in two-dimensional unsteady flows. This theory led to the development of a method, called the *geodesic eddy detection*, which seeks eddy boundaries as special closed material lines or surfaces that do not deform at leading order over a finite time interval in turbulence, which cannot be achieved by Eulerian eddy diagnostics [Haller and Beron-Vera, 2012, 2013; Beron-Vera, Wang et al., 2013]. Eddies framed as

such are able to travel with absolutely no leakage over their lifetimes.

In section 2.2 of this chapter, we use two simple analytical examples to highlight the issue of non-objectivity associated with Eulerian eddy criteria. Then we proceed to review the mathematical details of geodesic theory of transport barriers in section 2.3, which is divided into two parts. In the first part we define eddy boundaries as material lines based on their absolute deformation [Beron-Vera, Wang et al., 2013], while in the second we seek eddy boundaries as material lines based on their relative deformation [Haller and Beron-Vera, 2013, 2014]. Finally, we prove that under certain circumstance, these two definitions of eddy boundaries are consistent with each other.

2.2 The issue with Eulerian eddy detection

We begin by considering the incompressible two-dimensional flow with the streamfunction defined as

$$\psi = \sin y \cos(x - ct), \quad (2.1)$$

where c is a constant parameter. Such flow can be regarded as being produced by a Rossby wave travelling in a zonal channel.

According to Eulerian criteria (e.g., regions with nested closed streamlines), this flow field contains a periodic chain of eddy pairs with alternating polarities comoving to the right, regardless of the magnitude of wave phase speed c . Yet passive tracer initialized within one of these “eddies” is not trapped inside but stretched along the channel (Figure 2.3 top panels).

It is also simple to prove that the zonal flux through any fixed meridional section across the channel is zero at all times, independent of c . As such, another tempting yet unverified conclusion could be that this flow does not contain material eddies, despite the apparent eddy chain structure described by the streamlines.

However, true material structures in a time dependent system can neither be uncovered by instantaneous Eulerian flow information (e.g., geometry of streamlines) nor inferred from its net flux across a fixed section. Revealing such hidden structures requires, in most analytical cases, transforming the flow field into a distinguished reference frame under which the field becomes steady. In this case, such a distinguished frame is the one co-moving zonally with the same constant speed c , namely, $(X, y) = (x - ct, y)$. In this frame, the (steady) streamfunction takes the form:

$$\Psi(X, y) = cy + \sin y \cos X. \quad (2.2)$$

As shown in the middle panel of Figure 2.3, varying the phase speed c gives rise to different flow structures. In particular, as c is increased from 0.1 (middle-left) to 0.5 (middle-middle) to 1 (middle-right), the flow transforms from eddy-dominant to eddy-jet-coexisting to jet-dominant fields, respectively. In steady flows, streamlines coincide with trajectories of fluid parcels and are thus true material lines. This is further verified in the bottom panel of Figure 2.3, where a blob of passive tracer (red) initialized within a closed isoline of (2.2) at $t = 0$ (when $x = X$) is found to preserve its initial shape under the original system (2.1) with $c = 0.5$. In contrast, tracer (blue) initially residing outside of any closed isoline of (2.2) is controlled by meandering jets and advected in opposite direction under (2.1). In effect, distinct material structures moving in different directions lead to the zero zonal net flux mentioned above.

The second example, proposed by Haller [2005], is an exact solution of the Navier-Stokes equation with the velocity field expressed as

$$v(x, t) = \begin{bmatrix} \sin 4t & 2 + \cos 4t \\ -2 + \cos 4t & -\sin 4t \end{bmatrix} x, \quad (2.3)$$

where $v(x, t)$ denotes the two-dimensional velocity field and x is two-dimensional lo-

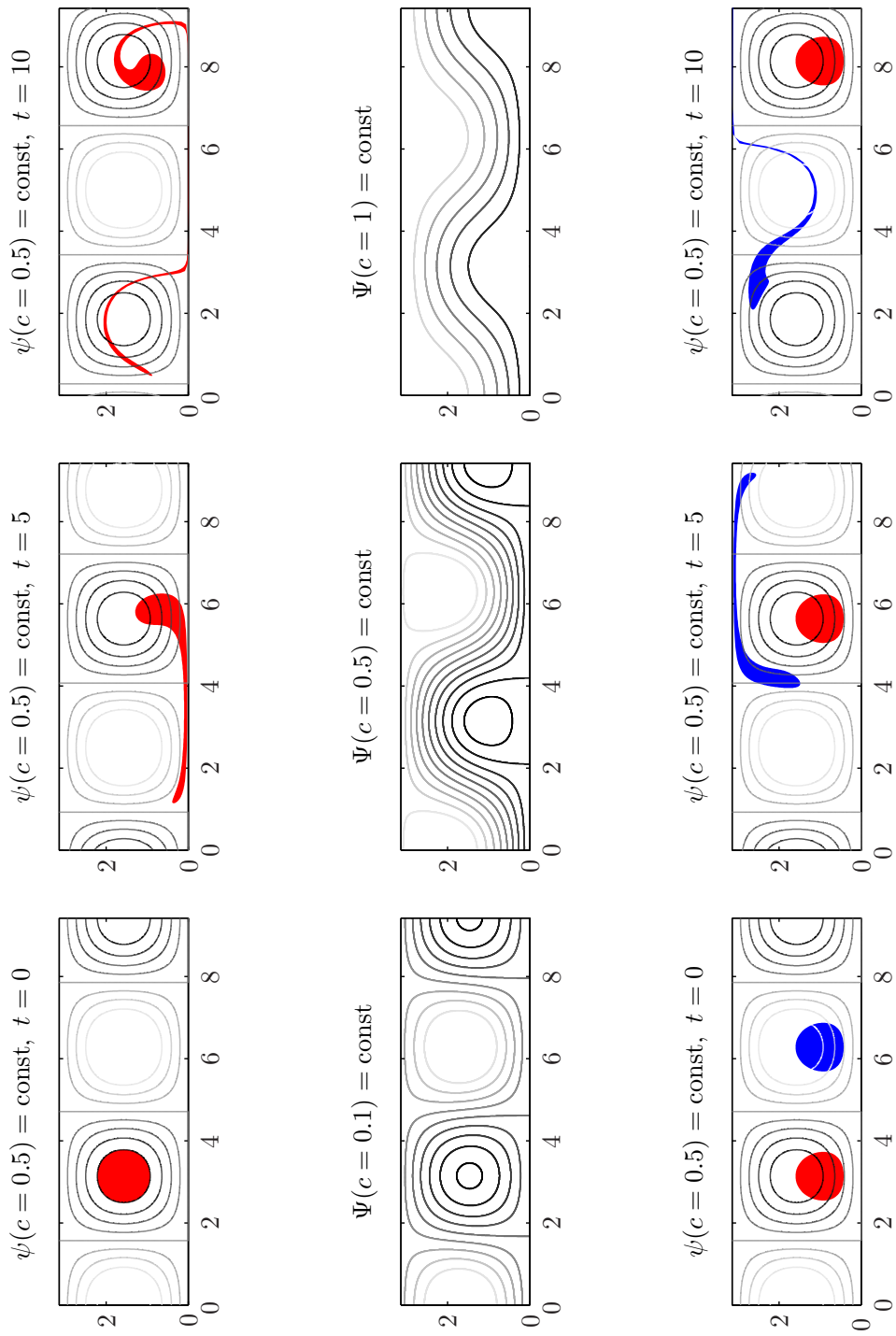


Figure 2.3: (top) Evolution of a passive tracer initialized within a closed streamline of the wave field with instantaneous streamlines overlaid, (middle) streamlines of the same wave field observed in a reference frame co-moving with it, and (bottom) evolution of a passive tracer initialized inside and outside the transport barrier inferred from the moving reference frame and advected by the original wave field.

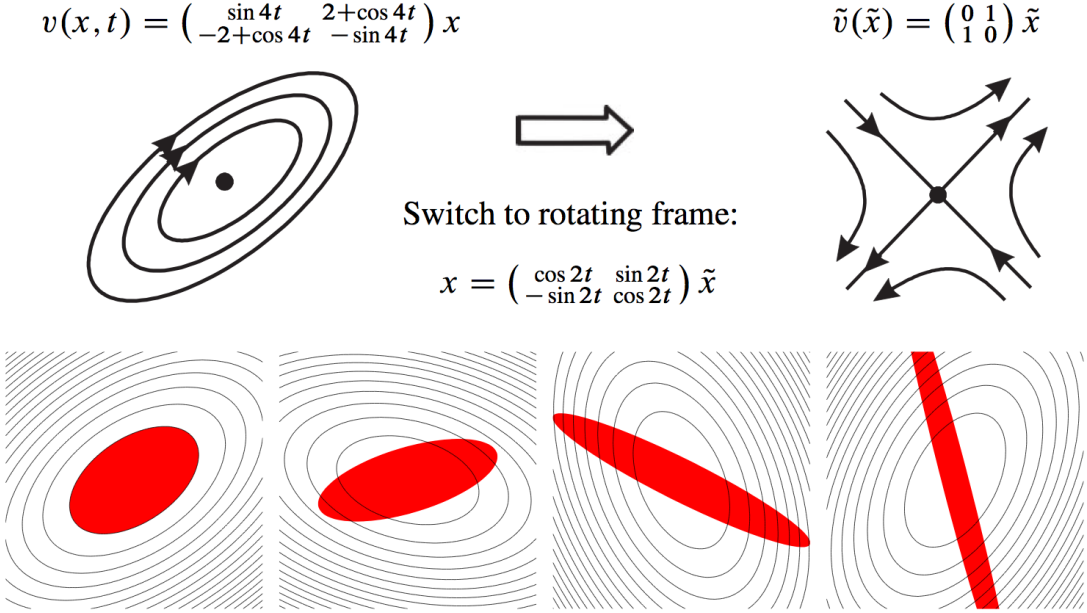


Figure 2.4: (top) A planar unsteady velocity field identified as an eddy by most Eulerian criteria. By being transformed into a frame in which the flow becomes steady, however, the velocity field exhibit a steady saddle flow with no closed transport barriers. Top panel adopted from Haller [2005]. (bottom) A blob of passive tracer initialized within the innermost closed streamline is not trapped inside but continuously stretched by the flow over time. Bottom panel credit Francisco J. Beron-Vera.

cation. System (2.3) highlights the issues with Eulerian eddy detection methods, according to which an eddy exists for all time, in particular, streamlines stay closed and vorticity dominates over strain and shear at all times. Yet tracer initialized within an inner closed streamline turns out to be controlled by a rotating saddle structure (Figure 2.4). Indeed, by transforming (2.3) into a reference frame under which the flow field becomes steady (Figure 2.4 upper panels), one readily observes a saddle structure within the flow with no closed transport barriers [Haller, 2005].

It should be realized that the above two examples are idealized cases. In realistic geophysical fluid flows, no distinguished reference frame exists: such flows remain unsteady in any reference frame [Lugt, 1979]. Conclusions about flow structures and

material transport, therefore, should not depend on the choice of reference frame. The issue with nonobjective eddy detection methods is critical to consider when estimating eddy-induced transport.

2.3 Objective Lagrangian eddy detection

This section presents the mathematical details of geodesic eddy detection [Haller and Beron-Vera, 2012, 2013, 2014; Beron-Vera, Wang et al., 2013], which brings the desired objectivity into eddy framing.

2.3.1 Mathematical Setup

Consider a two-dimensional unsteady flow field with velocity $v(x, t)$, where x refers to spatial position in \mathbb{R}^2 and t is time. The trajectories of fluid particles within this field satisfy the first order ordinary differential equation:

$$\frac{dx}{dt} = v(x, t). \quad (2.4)$$

The flow map, defined by

$$F_{t_0}^t := x(t; t_0, x_0), \quad (2.5)$$

takes an initial fluid particle at location x_0 and time t_0 to its later position $x(t; t_0, x_0)$ at time t . For instance, a material curve γ_0 at t_0 is mapped or advected by the flow into the curve $\gamma_t = F_{t_0}^t(\gamma_0)$, as illustrated in Figure 2.5.

For a smooth velocity field $v(x, t)$, the derivative of the flow map with respect to the initial positions $DF_{t_0}^t$ is an invertible tensor field [Arnold, 1973], conventionally called deformation gradient. The deformation gradient serves as the fundamental matrix solution of the equation of variations,

$$\dot{y} = Dv(F_{t_0}^t(x_0), t)y, \quad (2.6)$$

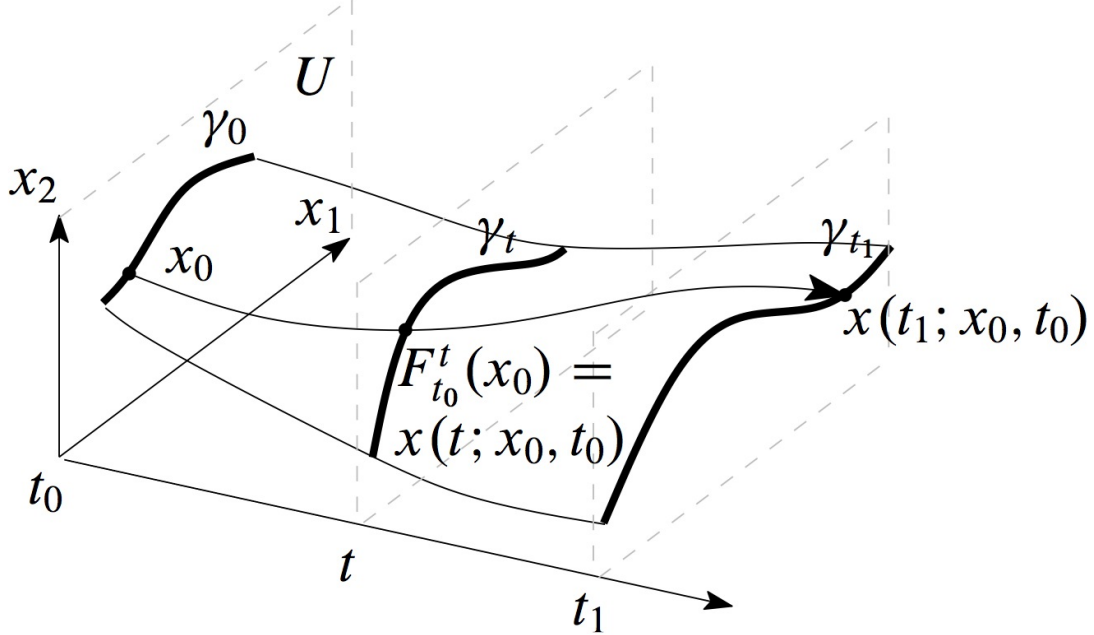


Figure 2.5: Evolution of a material curve under the flow map in phase space.

where $y(t)$ is an infinitesimal perturbation to a trajectory (Figure 2.6). Specifically,

$$y(t) = DF_{t_0}^t y(t_0). \quad (2.7)$$

Therefore square of the *distance* between initially nearby particles,

$$[y(t)]^2 = [DF_{t_0}^t(x_0)y(t_0)]^2 = y(t_0) \cdot C_{t_0}^t(x_0)y(t_0), \quad (2.8)$$

where

$$C_{t_0}^t(x_0) = DF_{t_0}^t(x_0)^\top DF_{t_0}^t(x_0) \quad (2.9)$$

is the right Cauchy-Green strain tensor.

Clearly, C is symmetric. Also, because DF is invertible, C is positive definite, $u^\top Cu = (DFu)^2 > 0$ for all $u \neq 0$. So (2.8) is physically sensible.

Another important property of C is objectivity. To see this consider the coordinate transformation between two frames unsteadily moving and rotating relatively to each

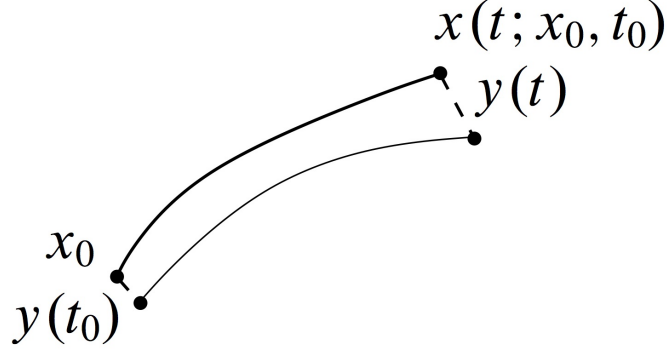


Figure 2.6: Evolution of an infinitesimal perturbation to a fluid particle trajectory.

other:

$$x \mapsto \bar{x} = Q(t)x + c(t), \quad (2.10)$$

where Q is a rotation (i.e., $Q^\top = Q^{-1}$ and $\det Q = 1$). Then consider the deformation gradient $G = DF_{t_0}^t(x_0) = \frac{\partial x}{\partial x_0}$ and the right Cauchy Green strain tensor $C = G^\top G$ in the x frame. Under (2.10) the deformation gradient becomes $\bar{G} = \frac{\partial \bar{x}}{\partial x} \frac{\partial x}{\partial x_0} = QG$, where a fixed set of reference configuration (i.e., material coordinates) x_0 applies to all reference frames as the continuum body itself is invariant [Truesdell and Noll, 2004]. Finally, the right Cauchy-Green tensor in the frame \bar{x} is $\bar{C} = \bar{G}^\top \bar{G} = (QG)^\top (QG) = G^\top Q^\top QG = G^\top G = C$. That is, C is not affected by the coordinate transformation, so is objective or frame invariant.

The frame-invariance of Cauchy-Green strain tensor has fundamental significance when it is used for extracting coherent structures in continuum medium, as the final results of material response are consistent for different observers in different reference frames. In oceanic applications, material features, such as a mesoscale eddy or a front, identified on the basis of Cauchy-Green strain tensor are self-consistent, regardless of whether the observation is processed from a satellite, on a ship, or along the coast [Peacock et al., 2015; Peacock and Haller, 2013].

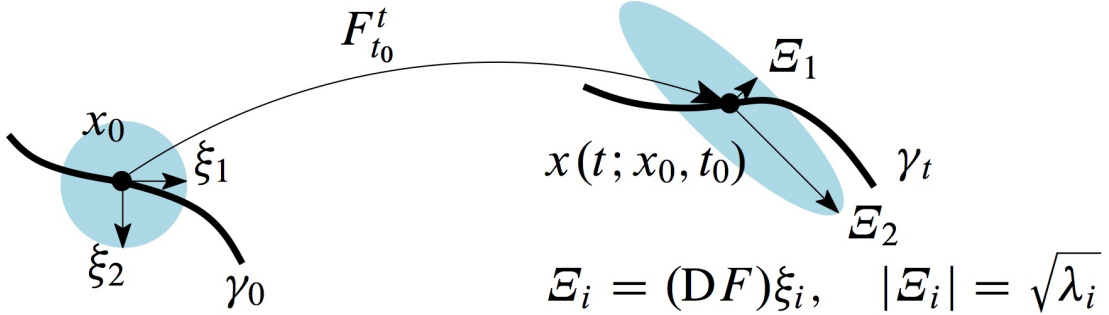


Figure 2.7: The geometrical meaning of the eigenvalues and eigenvectors of the Cauchy-Green Strain tensor

The eigenvalues $\lambda_i(x_0)$ and normalized eigenvectors $\xi_i(x_0)$ of $C_{t_0}^t$ satisfy

$$C_{t_0}^t \xi_i = \lambda_i \xi_i, \quad |\xi_i| = 1, \quad i = 1, \dots, n; \quad 0 < \lambda_1 \leq \dots \leq \lambda_n, \quad \xi_i \perp \xi_j, \quad i \neq j. \quad (2.11)$$

Geometrically, ξ_i and λ_i are interpreted as follows (Figure 2.7): an infinitesimally small circle of initial conditions at t_0 is carried and deformed by the flow map into a small ellipse at time t , the i th principal axis of which is aligned with the vector $\mathrm{D}F_{t_0}^t \xi_i$ and has the length $\sqrt{\lambda_i}$ times the radius of the initial circle.

Finally, another important symmetric tensor in classic continuum mechanics is the Green-Lagrangian strain tensor, defined as

$$E(x_0) = \frac{1}{2} [C(x_0) - I], \quad (2.12)$$

where I is identity matrix. We suppress the dependence of tensors C and E on the finite time window $[t_0, t]$ here for notational simplicity. Note that

$$E(x_0)\xi_i = \frac{1}{2} [C(x_0)\xi_i - I\xi_i] = \frac{1}{2} (\lambda_i - 1) \xi_i. \quad (2.13)$$

Therefore, a tensor E and its corresponding tensor C share the same set of (normalized) eigenvectors. Meanwhile, the eigenvalues of E are $\mu_i = \frac{1}{2}(\lambda_i - 1)$. As such, tensor E is not necessarily positive definite. Indeed, for instance, in two-dimensional incompressible flows, we usually have $\lambda_1 < 1 < \lambda_2$ at an initial location, therefore $\mu_1 < 0 < \mu_2$.

It should be noted that E is also invariant to change of reference frames (i.e., objective) owing to the objectivity of both C and reference configuration of the continuum body.

Geometrically, unlike λ_i, μ_i of E measure the difference between an infinitesimally small circle of initial conditions at time t_0 with its advected image under the flow map F at time t .

2.3.2 Eddy boundaries as extremum curves of absolute deformation

I. Formulation

In classical nonlinear dynamical systems theory, KAM curves are characterized as elliptical, closed material lines that resume their initial position periodically or quasiperiodically and exhibit strong twisting (i.e., shear) locally. As such, they can be viewed as idealized coherent eddy boundaries in incompressible two-dimensional (quasi)periodic flows. A material segment of a KAM curve generally experiences the least absolute stretching over several periods compared to its neighbouring curves that share the same endpoints of the segment. Its neighbouring curves are stretched exponentially fast due to the strong twisting around the reference torus segment (Figure 2.8).

In a two-dimensional unsteady flow defined over a finite time interval, locating at time t_0 the positions of material lines that will stretch the least over the time interval $[t_0, t]$ leads to a variational problem. As shown in Haller and Beron-Vera [2012], the solutions of this problem are distinguished material curves at time t_0 that turn out to be minimal geodesics (shortest paths) of the metric $g(u, v)(x_0) = u \cdot C_{t_0}^t(x_0)v$ generated by the Cauchy-Green strain tensor $C_{t_0}^t(x_0)$.

Among all geodesics passing through x_0 , the locally least-stretching geodesic at x_0 is of particular interest. This geodesic is tangent to the direction of minimal strain, ξ_1 , at x_0 .

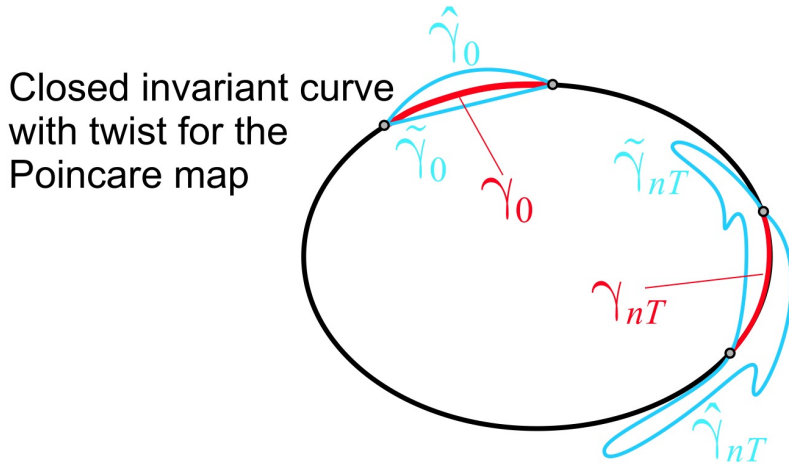


Figure 2.8: Minimal stretching property for a closed transport barrier (a KAM curve) in a two-dimensional temporally time T -periodic flow, for large enough iteration numbers of the Poincare map. Note that fixed-endpoint perturbations to the curve γ_0 stretch longer than γ_{nT} , whether or not they were initially longer than γ_0 . From Haller and Beron-Vera [2012].

Typical geodesics in a turbulent flow are still stretched by a relatively large amount, even though they are stretched less than any other curve connecting their endpoints. Most geodesics, therefore, do not act as observable transport barriers. Observable barriers, however, must necessarily run close to locally least-stretching geodesics. This means that at each point x_0 of an observable transport barrier, both the tangent and the curvature of the barrier must be close to the tangent and curvature of the locally least-stretching geodesic through x_0 . For short, we say that such a barrier is a material line that is *geodesically shadowed* over the time interval $[t_0, t]$.

Inspired by the local behavior of classical KAM curves, Haller and Beron-Vera [2012] seek maximizers of *Lagrangian shear* along a closed material line that is geodesically shadowed in an objective fashion.

Consider a parametrized material curve $\gamma_0 = \{x_0 = r(s) \subset U, s \in [s_1, s_2]\}$ at initial time t_0 , where s is arclength. The unit normal vector n_0 of this curve on any

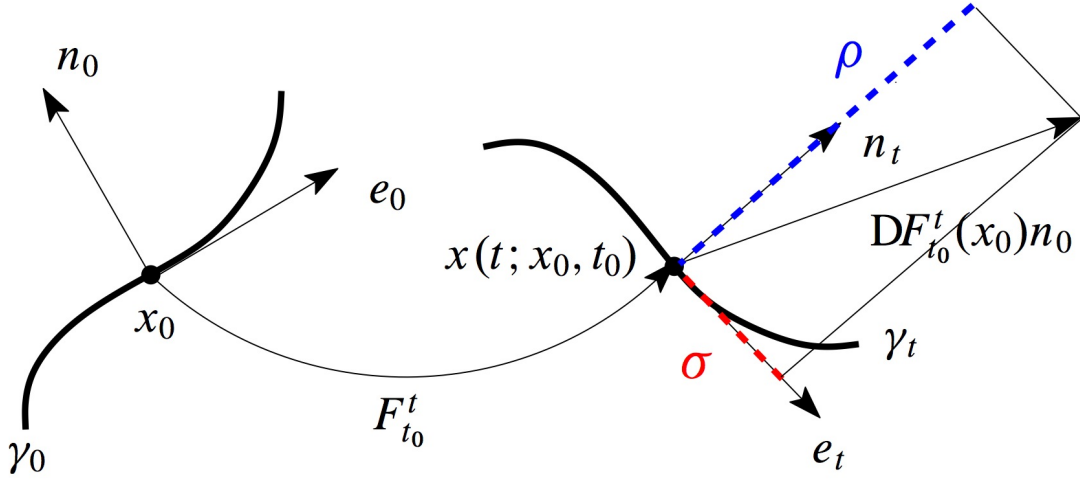


Figure 2.9: (left) A material line γ_0 of initial condition in a two-dimensional dynamical system, with the unit normal vector n_0 and unit tangential vector e_0 at point x_0 on it. (right) The initial curve γ_0 is carried and deformed by the flow map into curve γ_t (x_0 mapped to x_t), with the initial unit normal n_0 transformed into vector $DF_{t_0}^t(x_0)n_0$ ($DF_{t_0}^t(x_0)n_0$ denotes the deformation gradient tensor). The material shear at point x_t , σ , is the projection of $DF_{t_0}^t(x_0)n_0$ onto the unit tangential vector e_t locally.

point $x_0 \in \gamma_0$ can be expressed in terms of the unit tangent vector e_0 of this curve on the same point as

$$n_0 = \Omega e_0, \quad (2.14)$$

where Ω is an orthogonal, counterclockwise rotation tensor. It is also simple to prove that the tangent space $T_{x_t}\gamma_t$ along the trajectory $x_t = F_{t_0}^t(x_0)$ of the evolving material curve $\gamma_t = F_{t_0}^t(\gamma_0)$ is the linear span of $DF_{t_0}^t(x_0)e_0$ by the chain rule

$$\frac{dF_{t_0}^t(r(s))}{ds} = DF_{t_0}^t r'(s) = DF_{t_0}^t e_0. \quad (2.15)$$

Therefore, a unit tangent vector at x_t on $T_{x_t}\gamma_t$ can be expressed as

$$e_t = DF_{t_0}^t(x_0)e_0 / |DF_{t_0}^t(x_0)e_0|. \quad (2.16)$$

Haller and Beron-Vera [2012] define the Lagrangian shear, $\sigma_{t_0}^t(x_0)$, as the normal

projection of the linearly transformed unit normal vector $\text{DF}_{t_0}^t(x_0)n_0$ onto the unit tangent vector e_t of the advected curve γ_t (Figure 2.9).

As noted by Haller and Beron-Vera [2012], there is no necessarily explicit reference to the underlying material line γ_t , yet one can still compute $\sigma_{t_0}^t$ with respect to any initial point x_0 and any initial tangent vector e_0 as

$$\sigma_{t_0}^t(x_0) = \text{DF}_{t_0}^t(x_0)n_0 \cdot e_t \equiv \frac{\Omega e_0 \cdot C_{t_0}^t(x_0)e_0}{\sqrt{e_0 \cdot C_{t_0}^t(x_0)e_0}}. \quad (2.17)$$

The Lagrangian shear (2.17) naturally has two signs: positive $\sigma_{t_0}^t$ values correspond to clockwise shear in the local coordinate frame $[\xi_1(x_0), \xi_2(x_0)]$, whereas negative $\sigma_{t_0}^t$ values correspond to counterclockwise shear in the same local coordinate frame.

We proceed to seeking the local extrema of $\sigma_{t_0}^t(x_0; e_0)$. Without loss of generality, we rewrite the unit tangent vector e_0 as linear combinations of the local coordinate basis vectors as

$$e_0 = \alpha\xi_1 + \beta\xi_2, \quad (2.18)$$

with the coefficients α and β yet to be determined. Note that ξ_1 and ξ_2 are normalized and orthogonal vectors, therefore we have

$$|e_0|^2 = \alpha^2 + \beta^2 = 1. \quad (2.19)$$

Substituting (2.18) into (2.17), we obtain

$$\begin{aligned} \sigma_{t_0}^t(x_0, \alpha, \beta) &= \frac{[\Omega(\alpha\xi_1 + \beta\xi_2)] \cdot [C_{t_0}^t(\alpha\xi_1 + \beta\xi_2)]}{\sqrt{(\alpha\xi_1 + \beta\xi_2) \cdot [C_{t_0}^t(\alpha\xi_1 + \beta\xi_2)]}} \\ &= \frac{(\alpha\xi_2 - \beta\xi_1) \cdot [C_{t_0}^t(\alpha\xi_1 + \beta\xi_2)]}{\sqrt{(\alpha\xi_1 + \beta\xi_2) \cdot [C_{t_0}^t(\alpha\xi_1 + \beta\xi_2)]}} \\ &= \frac{\alpha\beta(\lambda_2 - \lambda_1)}{\sqrt{\alpha^2\lambda_1 + \beta^2\lambda_2}}, \end{aligned} \quad (2.20)$$

where we have fixed the relative direction of local basis vector as $\xi_2 = \Omega\xi_1$.

At extrema of $\sigma_{t_0}^t(x_0)$, we have

$$\begin{aligned}\frac{\partial\sigma}{\partial\alpha} &= \frac{\beta(\lambda_2 - \lambda_1)(\alpha^2\lambda_1 + \beta^2\lambda_2) - \alpha\beta(\lambda_2 - \lambda_1)\alpha\lambda_1}{(\alpha^2\lambda_1 + \beta^2\lambda_2)^{3/2}} = 2\lambda\alpha \\ \frac{\partial\sigma}{\partial\beta} &= \frac{\alpha(\lambda_2 - \lambda_1)(\alpha^2\lambda_1 + \beta^2\lambda_2) - \alpha\beta(\lambda_2 - \lambda_1)\beta\lambda_2}{(\alpha^2\lambda_1 + \beta^2\lambda_2)^{3/2}} = 2\lambda\beta,\end{aligned}\quad (2.21)$$

where λ here is a Lagrange multiplier introduced by the condition (2.19). Equivalently, we have

$$\begin{aligned}(\lambda_2 - \lambda_1)\frac{\beta^3\lambda_2}{(\alpha^2\lambda_1 + \beta^2\lambda_2)^{3/2}} &= 2\lambda\alpha \\ (\lambda_2 - \lambda_1)\frac{\alpha^3\lambda_1}{(\alpha^2\lambda_1 + \beta^2\lambda_2)^{3/2}} &= 2\lambda\beta\end{aligned}\quad (2.22)$$

The quotient of the two equations in (2.22) yields

$$\frac{\alpha}{\beta} = \pm\sqrt[4]{\frac{\lambda_2}{\lambda_1}}. \quad (2.23)$$

Combining (2.19) with (2.23) gives the following two directions for e_0 :

$$\chi_{\pm} = \sqrt{\frac{\sqrt{\lambda_2}}{\sqrt{\lambda_1} + \sqrt{\lambda_2}}}\xi_1 \pm \sqrt{\frac{\sqrt{\lambda_1}}{\sqrt{\lambda_1} + \sqrt{\lambda_2}}}\xi_2. \quad (2.24)$$

By calculating the second derivatives of $|\sigma_{t_0}^t(x_0)|^2$ with respect to α and β , one readily verifies that χ_{\pm} indeed admit local extrema instead of other types of stationary values of $\sigma_{t_0}^t(x_0)$, which are given by

$$\sigma_{t_0}^t(x_0, \chi_{\pm}) = \pm\frac{\sqrt{\lambda_2(x_0)} - \sqrt{\lambda_1(x_0)}}{\sqrt[4]{\lambda_1(x_0)\lambda_2(x_0)}}. \quad (2.25)$$

Haller and Beron-Vera [2012] define orbits of (2.24) as *shearlines*.

Note that

$$\chi_{\pm} \cdot C_{t_0}^t \chi_{\pm} = \frac{\sqrt{\lambda_2}\lambda_1}{\sqrt{\lambda_1} + \sqrt{\lambda_2}} + \frac{\lambda_2\sqrt{\lambda_1}}{\sqrt{\lambda_1} + \sqrt{\lambda_2}} = \sqrt{\lambda_1\lambda_2}. \quad (2.26)$$

In the incompressible flow case, $\lambda_1\lambda_2 = 1$, so a shearline resumes its initial arclength over the finite time interval $[t_0, t]$. In addition, the mapping $F_{t_0}^t$ is area preserving for

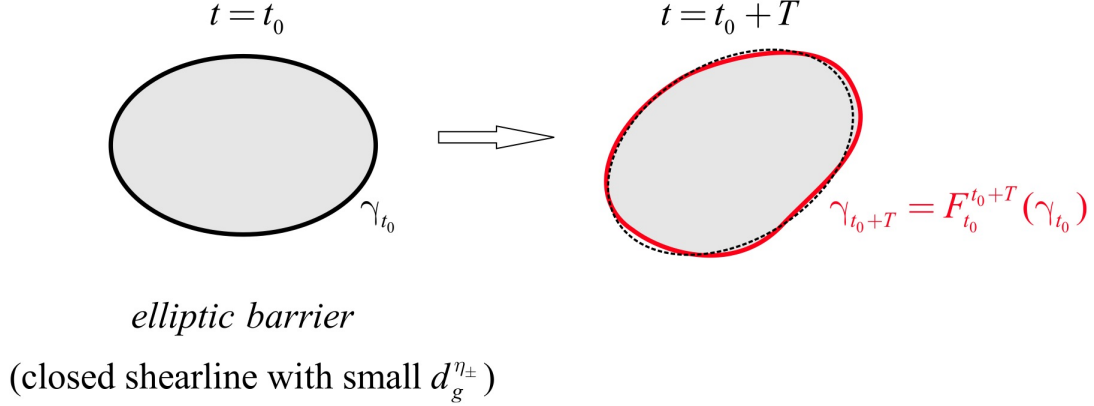


Figure 2.10: Schematic of an elliptic transport barrier. A closed shearline γ_{t_0} , computed from flow data over $[t_0, t_0 + T]$ plays the role of a generalized KAM curve. Dashed line indicates a hypothetical translated and rotated position of γ_{t_0} for reference. The advected material line γ_{t_0+T} has the same arclength, and encloses the same area as γ_{t_0} does. From Haller and Beron-Vera [2012].

all time in such case. This implies that a *closed* shearline in a two-dimensional incompressible flow will preserve its enclosed area and resume its arclength under the flow map $F_{t_0}^t$. In (quasi)periodic dynamical systems, such a simultaneous preservation of enclosed area and arclength reassumption makes the KAM curves extraordinarily robust, thereby qualifying as boundaries of idealized eddies. For this particular reason, Haller and Beron-Vera [2012] classify closed shearlines as generalized KAM curves in aperiodic flows, and define the member of a nested family of such lines that is most closely geodesically shadowed as the boundary of a coherent Lagrangian eddy. Eddy boundaries defined as such have particular significance, namely, while a closed shearline may be substantially translated and rotated by the flow map $F_{t_0}^t$, it can only be deformed slightly, because both its enclosed area and arclength must be preserved from the initial to final times (Figure 2.10).

II Numerical algorithm

Here we introduce the numerical algorithm for extracting eddy boundaries as closed shearlines:

1. Fix a finite time interval $[t_0, t]$ over which shearlines are to be computed. Construct the flow map $F_{t_0}^t$ by integrating equation (2.4) over a grid \mathcal{G}_0 of initial conditions x_0 .
2. Calculate the Cauchy-Green strain tensor field $C_{t_0}^t(x_0)$, and its eigenvalues fields λ_i and eigenvector fields ξ_i using finite differencing over \mathcal{G}_0 .
3. Calculate shearlines by solving the ordinary differential equations (2.24), locate each eddy candidate region filled with limit cycles of (2.24).
4. Extract limit cycles of (2.24) with the aid of a Poincaré section.
5. Find the limit cycle that is most closely shadowed by the least-stretching Cauchy-Green geodesic in the sense that the geodesic deviation,

$$d_g^{\chi\pm}(\mathbf{x}_0) = |1 - \alpha_1| + \left| \left(\alpha_1 + \frac{\lambda_1}{\lambda_2} - 1 \right) \kappa_1 \mp \alpha_2 \kappa_2 \mp \frac{\nabla \alpha_1 \cdot \chi_\pm}{\alpha_2} - \frac{\nabla \lambda_1 \cdot \xi_2}{2\lambda_2} \right|,$$

where $\kappa_i(\mathbf{x}_0) = \nabla \xi_i(\mathbf{x}_0) \xi_i(\mathbf{x}_0) \cdot \xi_j(\mathbf{x}_0)$ and $i \neq j$, is minimized in the family of limit cycles.

6. To obtain the location of a coherent Lagrangian eddy at later times, advect the eddy boundary by the flow map $F_{t_0}^t$.

2.3.3 Eddy boundaries as stationary curves of relative deformation

On the basis of previous work [Haller and Beron-Vera, 2012], Haller and Beron-Vera [2013, 2014] provide a generalized framework, geodesic theory of elliptic Lagranigan

Coherent Structures (LCS), for locating coherent Lagrangian eddies in two dimensional unsteady flows. Here we review the details of this theory as well as the eddy detection method based on it.

I Formulation

Consider a closed material belt initialized in a two-dimensional flow field with aperiodic time dependence (Figure 2.11 left panel). Typically, the centrepiece loop γ (red) and its neighbouring curves (green) of this belt will be stretched at exponentially fast but very different rates under the flow map $F_{t_0}^t(\gamma)$ due to the high sensitivity of initial conditions in turbulent flow. Over a finite time interval, one readily observes the inhomogeneity across the belt, as material strain experienced by γ is different from its neighboring curves.

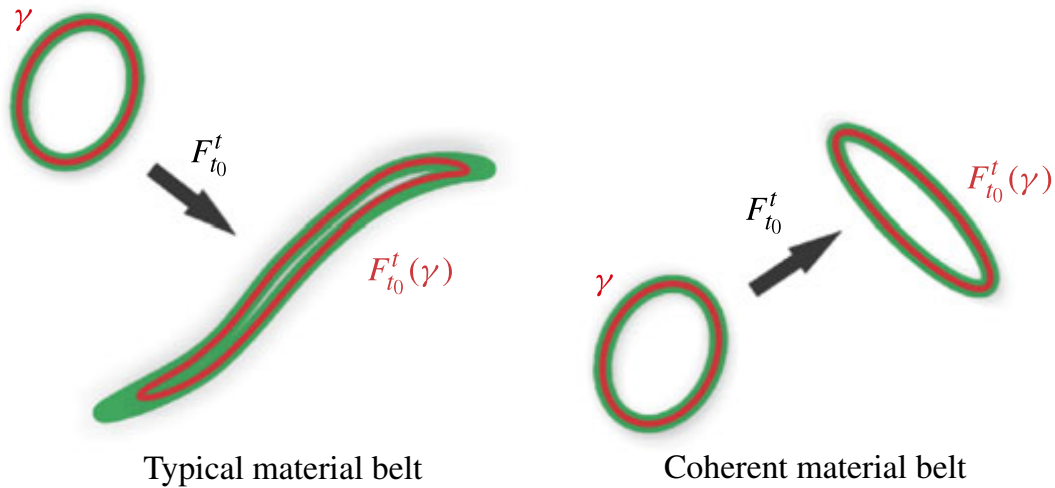


Figure 2.11: (left) Typical material belt exhibits inhomogeneity after a finite time interval in unsteady flows due to the sensitivity of initial condition difference across the belt. (right) Exceptional material belts within which material loops stretch by the same factor within a finite time interval, hence exhibiting no leading order variations in material strain across the belt. From Haller and Beron-Vera [2013].

The geodesic theory of elliptic LCS [Haller and Beron-Vera, 2013, 2014], on the

other hand, seeks coherent Lagrangian eddy boundaries as material loops embedded in coherent material belts of fluid elements that resist the aforementioned inhomogeneity induced by the ambient turbulent flow, exhibiting no leading order change in averaged material strain (Figure 2.11 right panel). As a result, they do not stretch into, or break away from the enclosed fluid region.

To describe this coherence principle more mathematically, assume $\varepsilon > 0$ as a minimal threshold over which difference in averaged material strain of nearby loops can be physically observed over a finite time interval $[t_0, t]$. According to the smooth dependence on initial fluid positions [Arnold, 1973], a strain difference of $O(\varepsilon)$ is observable within an $O(\varepsilon)$ width of material belt around a typical closed loop γ . Yet we expect the $O(\varepsilon)$ strain variation to vanish in exceptional material belts.

Consider a smooth, parametrized curve of initial conditions

$$\gamma(t_0) = \gamma_0 = \{x_0 = r(s) \subset U, s \in [s_1, s_2]\}, \quad (2.27)$$

where s is an arbitrary parameter (e.g., arclength) and U refers to an open domain of interest; γ_0 is carried forward by the flow map into its later position

$$\gamma(t) = \gamma_t = F_{t_0}^t(\gamma_0). \quad (2.28)$$

We then denote the length of γ_0 and γ_t as l_{t_0} and l_t , respectively, which can be expressed as

$$l_{t_0} = \sqrt{r'(s) \cdot r'(s)}, \quad l_t = \sqrt{r'(s) \cdot C_{t_0}^t(r(s))r'(s)}, \quad (2.29)$$

The integrated material strain along γ over $[t_0, t]$ is given by

$$Q(\gamma) = \oint \frac{l_t}{l_{t_0}} ds. \quad (2.30)$$

The special material belts of interest must have $Q(\gamma + \varepsilon h) = Q(\gamma) + O(\varepsilon^2)$, where εh represents a small perturbation to γ . This requires that the first variation of Q must

vanish on γ :

$$\delta Q(\gamma) = 0. \quad (2.31)$$

In other words, γ is a stationary solution of (2.30).

As noted by Haller and Beron-Vera [2013], the calculus of variations (2.31) leads to Euler-Lagrange equations that provide no immediate insight. Instead of solving them directly, Haller and Beron-Vera [2013] take advantage of the Noether's theorem.

In effect, because the Lagrange $L(r, r') = \sqrt{\frac{r' \cdot C(r)r'}{r' \cdot r'}}$ does not depend explicitly on s (the time-like variable), the energy (Hamiltonian) must be preserved:

$$L - r' \cdot \partial_{r'} L \equiv L = \text{const}. \quad (2.32)$$

Therefore, the stationary curves of averaged material strain must satisfy

$$l_t^2(r, r') - \lambda^2 l_{t_0}^2(r) = 0 \quad (2.33)$$

for some choice of parameter $\lambda > 0$. Material loops of this type are uniformly stretched by the same factor λ over the time interval $[t_0, t]$ and serve as perfectly coherent centre-pieces of observably coherent material belts.

Haller and Beron-Vera [2013] show that material loops satisfying (2.33) are also null *geodesics* of the Lorentzian metric

$$g_\lambda(u, v) = u \cdot E_\lambda v, \quad E_\lambda = \frac{1}{2}[C(x_0) - \lambda^2 I], \quad \lambda > 0 \quad (2.34)$$

where E_λ denotes a generalization of the classic Green-Lagrangian strain tensor E (2.12). Similar to E , E_λ is symmetric and generally not positive definite. Geometrically, it measures the deviation of an ellipse generated by a flow map that acts on an infinitesimal circle of initial conditions from the circle obtained by simply expanding the same initial condition isotropically by factor λ [Haller, 2014].

We next substitute (2.29) into (2.33) and obtain

$$\mathbf{r}' \cdot C_{t_0}^t \mathbf{r}' - \lambda^2 \mathbf{r}' \cdot \mathbf{r}' = 0. \quad (2.35)$$

We then write the vector \mathbf{r}' as linear combinations of the right Cauchy-Green tensor eigenvectors as $\mathbf{r}' = \alpha \xi_1 + \beta \xi_2$, and make $\mathbf{r}'^2 = \alpha^2 + \beta^2 = 1$ (so \mathbf{r}' is a unit vector), both of which, after substitution into (2.35), yield:

$$\alpha = \pm \sqrt{\frac{\lambda_2 - \lambda^2}{\lambda_2 - \lambda_1}}, \quad \beta = \pm \sqrt{\frac{\lambda^2 - \lambda_1}{\lambda_2 - \lambda_1}}, \quad \lambda_1 < \lambda^2 < \lambda_2 \quad (2.36)$$

The problem reduces to seeking limit cycles of the ordinary differential equations:

$$\mathbf{r}'(s) = \eta_\lambda^\pm(\mathbf{r}(s)), \quad \eta_\lambda^\pm = \sqrt{\frac{\lambda_2 - \lambda^2}{\lambda_2 - \lambda_1}} \xi_1 \pm \sqrt{\frac{\lambda^2 - \lambda_1}{\lambda_2 - \lambda_1}} \xi_2. \quad (2.37)$$

Such limit cycles, named λ -loops, are found to occur in non-intersecting families [Haller and Beron-Vera, 2013].

Note that ξ_1 and ξ_2 are also eigenvectors of tensor E_λ and become ill-defined at locations where $\lambda_1 = \lambda_2$. Null-geodesics therefore cannot be extended to points where $E_\lambda = 0$. Topologically (detailed proof is in Appendix D of [Haller and Beron-Vera, 2013]), a family of limit cycles of η_λ constitutes an annular, singularity-free region, but necessarily encircle clusters of singularities around their center. In the incompressible context where $\lambda_1 \lambda_2 = 1$, the Cauchy-Green strain tensor at a singularity point becomes identity matrix (Figure 2.12 left panel).

The limit cycles of (2.37) will either grow or shrink under changes in λ over the time window $[t_0, t]$. We define the outermost member of a family of such limit cycles as the coherent Lagrangian eddy boundary (Figure 2.12 right panel). This boundary is optimal inasmuch as immediately outside of it, no coherent material belts may exist. Typically, the limit cycles only exist for $\lambda \simeq 1$.

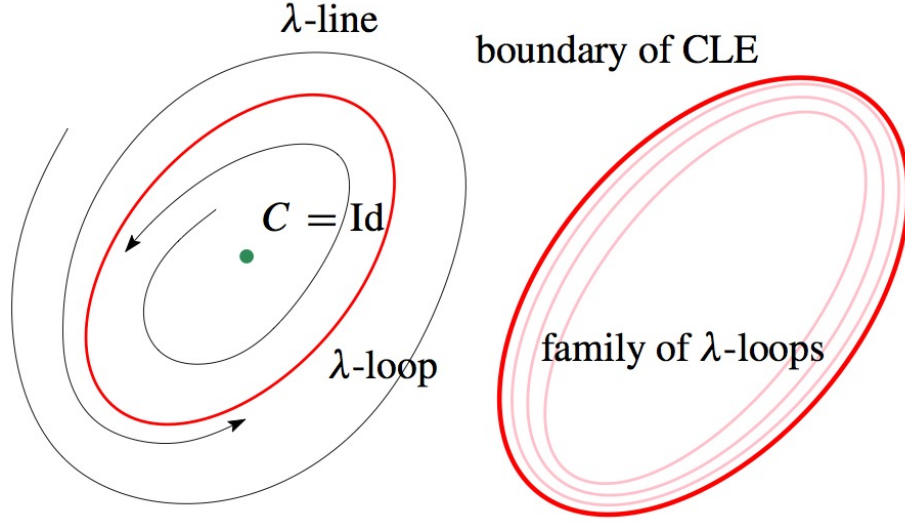


Figure 2.12: (left) In two dimensional fluid flows, coherent Lagrangian eddies necessarily contain at least one Green-Lagrangian singularity where the Cauchy-Green strain tensor becomes identity matrix. (right) Out of all members of nested λ -loops, the outermost one is defined as the boundary of a coherent Lagrangian eddy

II Numerical algorithm

Numerically, the geodesic eddy detection can be implemented as following steps [Haller and Beron-Vera, 2013] :

1. Fix a grid \mathcal{G}_0 of initial conditions and a time scale T over which geodesic eddies are to be detected. For each initial condition $x_0 \in \mathcal{G}_0$, integrate the differential equation (2.4) from an initial time t_0 to time $t = t_0 + T$ to obtain a discrete approximation of flow map $F_{t_0}^t(x_0)$ over \mathcal{G}_0 .
2. Using finite differencing to obtain the deformation gradient field $DF_{t_0}^t(x_0)$, then compute the Cauchy-Green strain tensor field $C_{t_0}^t(x_0)$ and its eigenvalue and eigenvector fields, $\lambda_i(x_0)$ and $\xi_i(x_0)$.
3. Locate singularities of $E_\lambda(x_0)$, which limit cycles of (2.37) must encircle. For an incompressible flow, such singularities can be isolated as intersections of the

level curves $C_{12} = 0$ with the level curves $C_{11} - C_{22} = 0$, where C_{ij} denotes the ij th entry of $C_{t_0}^t(x_0)$.

4. Locate candidate regions for geodesic eddies whose sizes are in the range of interest. Specifically, fix a length scale L for eddy radii of interest, then isolate clusters of singularities encircled by annular, singularity-free regions of radius larger than L .
5. In the candidate region seek the outermost possible limit cycle of (2.37) with the aid of a Poincaré section. If such a limit cycle exists for $\lambda = 1$, a primary geodesic eddy is found.
6. If no limit cycle is found for $\lambda = 1$, then search for the outermost possible limit cycle with $\lambda \neq 1$ by varying λ appropriately. If a limit cycle is found, a secondary geodesic eddy is located. If no limit cycle is found for any λ , the candidate region does not contain a geodesic eddy.
7. To track the motion of geodesic eddies in time, obtain their time- t positions by applying the flow map $F_{t_0}^t$ to their boundaries detected at time t_0 .

2.3.4 Equivalence of the two formulations in the incompressible case

When $\lambda = 1$ (absolutely no stretching), in the incompressible flow case ($\lambda_1\lambda_2 = 1$) it follows that:

$$\begin{aligned}
 \eta_1^\pm &= \sqrt{\frac{\lambda_2 - 1}{\lambda_2 - \lambda_1}} \xi_1 \pm \sqrt{\frac{1 - \lambda_1}{\lambda_2 - \lambda_1}} \xi_2 \\
 &= \sqrt{\frac{(\lambda_2 - 1)\lambda_2}{\lambda_2^2 - 1}} \xi_1 \pm \sqrt{\frac{(1 - \lambda_1)\lambda_1}{1 - \lambda_1^2}} \xi_2 \\
 &= \sqrt{\frac{\lambda_2}{1 + \lambda_2}} \xi_1 \pm \sqrt{\frac{\lambda_1}{1 + \lambda_1}} \xi_2 \\
 &= \sqrt{\frac{\sqrt{\lambda_2}}{\sqrt{\lambda_1} + \sqrt{\lambda_2}}} \xi_1 \pm \sqrt{\frac{\sqrt{\lambda_1}}{\sqrt{\lambda_1} + \sqrt{\lambda_2}}} \xi_2 \\
 &\equiv \chi_\pm.
 \end{aligned} \tag{2.38}$$

In other words, in incompressible two-dimensional flows, closed shearlines coincide with $\lambda = 1$ loops.

The difference between closed shearlines and λ -loops can be generalized as following: (1) shearlines are extracted based on the *local* behavior of fluid structures, whereas λ -loops are stationary solutions to a *global* variational principle [Haller, 2014]; (2) in incompressible flows, shearlines do not include λ -loops with $\lambda \neq 1$ (i.e., coherent Lagrangian eddy boundaries experiencing minor stretching or shrinking). As a result, shearline detection isolates coherent Lagrangian eddies with more restrictions but yields the most robust eddy candidates in the incompressible case. In contrast, λ -loops permit minor deformation of eddies. Eddies bounded by λ -loops are therefore more suitable for quantifying transport as well as detailed analysis of material growth and decay in a long run, which is explored in chapters 4–5.

Chapter 3

Objective detection of Agulhas rings

3.1 Overview

Mesoscale oceanic eddies are routinely detected from instantaneous velocities derived from satellite altimetry data. While simple to implement, this approach often gives spurious results and hides true material transport. Here it is shown how geodesic transport theory, a recently developed technique from nonlinear dynamical systems, uncovers eddies objectively. Applying this theory to altimetry-derived velocities in the South Atlantic reveals, for the first time, Agulhas rings that preserve their material coherence for several months, while ring candidates yielded by other approaches tend to disperse or leak within weeks. These findings suggest that available velocity-based estimates for the Agulhas leakage, as well as for its impact on ocean circulation and climate, need revision. This chapter is published in Journal of Physical Oceanography [Beron-Vera, Wang et al., 2013].

3.2 Background

Oceanic eddies are commonly envisaged as whirling bodies of water that preserve their shape, carrying mass, momentum, energy, thermodynamic properties, and biogeochem-

ical tracers over long distances [e.g., Robinson, 1983]. While this widespread view on eddies is fundamentally Lagrangian (material), most available eddy detection methods are Eulerian (velocity-based).

Eulerian detection of mesoscale eddies (with diameters ranging from 50 to 250 km) is routinely applied to instantaneous velocities derived from satellite altimetry measurements of sea surface height (SSH). In some cases, eddies are identified from the Okubo–Weiss criterion as regions where vorticity dominates over strain [e.g., Isern-Fontanet et al., 2003; Morrow et al., 2004; Chelton et al., 2007; Henson and Thomas, 2008]. In other cases, eddies are sought as regions filled with closed streamlines of the SSH field [e.g., Goni and Johns, 2001; Fang and Morrow, 2003; Chelton et al., 2011b,a], or as features obtained from a wavelet-packet decomposition of the SSH field [Doglioli et al., 2007; Turiel et al., 2007]. These detection methods invariably use instantaneous Eulerian information to reach long-term conclusions about fluid transport. Furthermore, they give different results in reference frames that move or rotate relative to each other.

The problem with the use of instantaneous velocities is their inability to reveal long-range material transport and coherence in unsteady flows [Batchelor, 1964]. An example is shown in Fig. 3.1, where the instantaneous velocity field is classified as eddy-like for all times by each of the Eulerian criteria mentioned above. Specifically, vorticity dominates over strain, and streamlines are closed for all times. Yet actual particle motion turns out to be governed by a rotating saddle point with no closed transport barriers

Figure 3.1 also highlights the issue with frame-dependent eddy detection, whether Eulerian or Lagrangian. Truly unsteady flows have no distinguished reference frames: such flows remain unsteady in any frame [Lugt, 1979]. Conclusions about flow structures, therefore, should not depend on the chosen frame, because it is not a priori known which—if any—frame reveals those structures correctly.

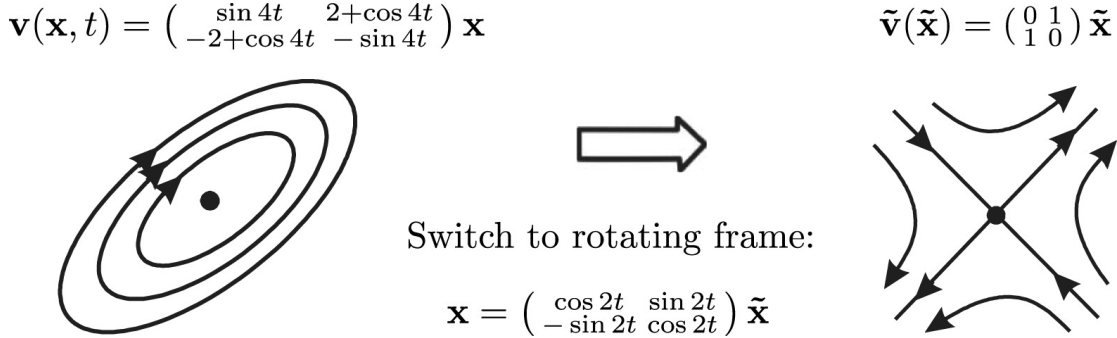


Figure 3.1: A planar unsteady velocity field identified as an eddy by Eulerian criteria. In an appropriate rotating frame, however, the velocity field becomes a steady saddle flow with no closed transport barriers. From Haller [2005].

Beyond conceptual problems, Eulerian eddy detection yields noisy results, necessitating the use of filtering and threshold parameters. Applying such detection methods to altimetry data, Souza et al. [2011b] report variabilities up to 50% in the number of eddies detected, depending on the choice of parameters and filtering methods. A systematic comparison of these varying numbers with actual material transport is difficult because of the sparseness of in-situ hydrographic measurements and Lagrangian data. In particular, most useful drifter trajectory data are only available from dedicated experiments, and satellite ocean color imagery is constrained by cloud cover or the absence of biological activity. This in turn implies that Eulerian predictions for Lagrangian eddy transport have remained largely unverified.

These shortcomings of contemporary eddy detection are important to consider when quantifying transport by eddies. For instance, recent studies suggest that long-range transport by anticyclonic mesoscale eddies (Agulhas rings) pinched off from the Agulhas Current retroflection is a potential moderating factor in global climate change. Known as the largest eddies in the ocean [Olson and Evans, 1986], Agulhas rings transport warm and salty water from the Indian Ocean into the South Atlantic (Agulhas leakage). They may also possibly reach the upper arm of the Atlantic Meridional Over-

turning Circulation (AMOC) when driven northwestward by the Benguela Current and its extension [Gordon, 1986]. Following an apparent southward shift in the subtropical front [Ridgway and Dunn, 2007], the intensity of the Agulhas leakage has been on the rise [Biastoch et al., 2009], leading to speculation that it may counteract the slowdown of the AMOC due to Arctic ice melting in a warming climate [Beal et al., 2011]. To assess this conjecture, an accurate Lagrangian identification of Agulhas rings is critical.

Indeed, most eddies identified from Eulerian footprints will disperse over relatively short times. While some of these dispersing features still drag water in their wakes, the transported water will stretch and fold due to the lack of a surrounding, coherent material boundary. As a consequence, distinguished features of the transported water, such as high temperature and salinity, will be quickly lost due to enhanced diffusion across filamented material boundaries.

Counteracting the effects of melting Arctic ice on AMOC requires a supply of warm and salty water [Beal et al., 2011]. Agulhas rings with persistent and coherent material cores deliver this type of water directly from its source, the Agulhas leakage. By contrast, transient Eulerian ring-like features mostly stir the ocean without creating the clear northwest pathway for temperature and salinity envisioned by Gordon [1986].

In steady flow, coherent material eddies are readily identified as regions of closed streamlines. In near-steady flows with periodic time dependence, the Kolmogorov–Arnold–Moser (KAM) theory [cf., e.g., Arnold et al., 2006] reveals families of nested closed material curves (so-called KAM curves) that assume the same position in the flow after each temporal period. An outermost such KAM curve from a given family, therefore, plays the role of a coherent material eddy boundary. This result extends to near-steady time-quasiperiodic flows, in which KAM curves are quasiperiodically deforming closed material lines [Jorba and Simó, 1996].

Identifying similar material boundaries for coherent eddies in general unsteady flows has been an open problem. Recently, however, Haller and Beron-Vera [2012] developed a new mathematical theory of transport barriers that, among other features, identifies generalized KAM curves (elliptic transport barriers) for arbitrary unsteady flows. Here we use this new theory to devise a methodology, *geodesic eddy detection*, for the objective identification of Lagrangian eddy boundaries in the ocean.

Analyzing altimetry measurements in the eastern side of the South Atlantic subtropical gyre, we find that geodesic eddy detection significantly outperforms available Eulerian and Lagrangian methods in locating long-lived and coherent Agulhas rings. An independent analysis of available satellite ocean color (chlorophyll) data corroborates our results by showing localized and persistent biological activity in an eddy identified using geodesic eddy detection. Our findings suggest that Eulerian estimates of the volume of water transported by Agulhas rings in a coherent manner are significantly exaggerated.

3.3 Methodology

3.3.1 Dynamical systems setup

Consider an unsteady flow on the plane with velocity field $\mathbf{v}(\mathbf{x}, t)$, where $\mathbf{x} = (x, y)$ denotes position and t is time. The evolution of fluid particle positions in this flow satisfies a nonautonomous dynamical system given by the following differential equation:

$$\frac{d\mathbf{x}}{dt} = \mathbf{v}(\mathbf{x}, t). \quad (3.1)$$

Material transport in (3.1) is determined by the properties of the flow map,

$$F_{t_0}^t : \mathbf{x}_0 \mapsto \mathbf{x}(t; \mathbf{x}_0, t_0), \quad (3.2)$$

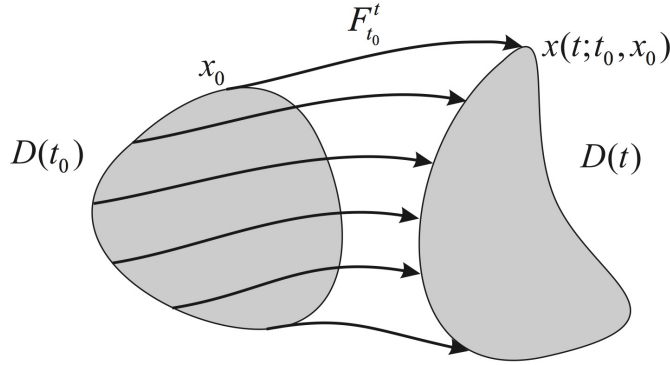


Figure 3.2: A fluid domain at time t_0 , $D(t_0)$, deformed under the flow map, $F_{t_0}^t : \mathbf{x}_0 \mapsto \mathbf{x}(t; \mathbf{x}_0, t_0)$, into a domain $D(t)$ at time $t \neq t_0$ along fluid particle trajectories. From Beron-Vera, Wang et al., [2013].

which takes an initial fluid particle position \mathbf{x}_0 at time t_0 to its later position $\mathbf{x}(t; t_0, \mathbf{x}_0)$ at time $t \neq t_0$, along trajectories of (3.1) (Fig. 3.2).

When obtained from satellite altimetry (cf. section 3.3.5), the velocity field in (3.1) is a temporally aperiodic, highly unsteady finite-time dataset. Material transport in the resulting flow, therefore, cannot be described by classic dynamical systems methods, such as those surveyed by Ottino [1989]. Instead, we adopt the recent approach of Haller and Beron-Vera [2012] by seeking transport barriers in (3.1) near least-stretching material lines.

3.3.2 Transport barriers as geodesics

As noted in Haller and Beron-Vera [2012], the least-stretching behavior of transport barriers is observed in several canonical flow examples where they are known to exist. Examples include steady flow around a stagnation point, steady shear jet flow, and steady circular shear flow.

Of particular relevance for our purposes here is the steady circular shear flow, the prototype of a coherent eddy. The least-stretching property of circular transport barriers in this flow is illustrated in Fig. 3.3. Indeed, for sufficiently long time, perturbations to

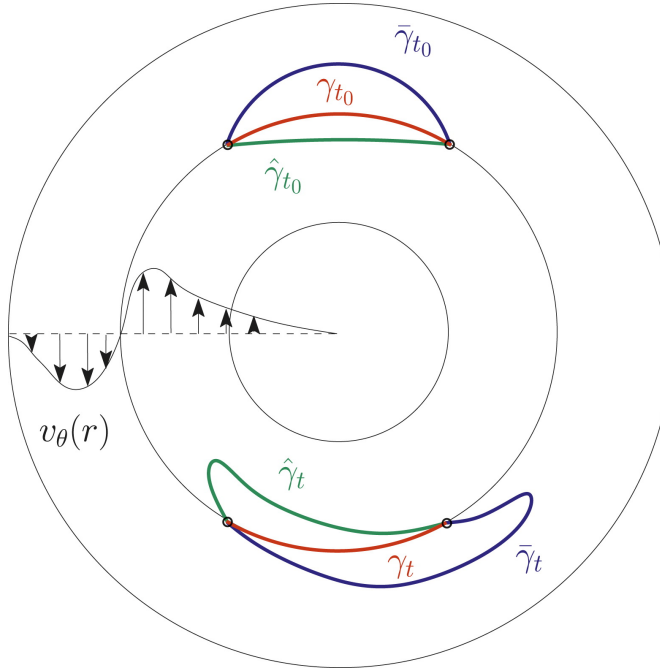


Figure 3.3: Minimal stretching property of a material curve γ_{t_0} , for times t sufficiently larger than t_0 , in a steady circular shear flow among material curves with the same endpoints, $\hat{\gamma}_{t_0}$ and $\bar{\gamma}_{t_0}$. Note that $\hat{\gamma}_{t_0}$ and $\bar{\gamma}_{t_0}$ stretch longer than γ_t , regardless of whether they are initially shorter or longer than γ_{t_0} . From Beron-Vera, Wang et al., [2013].

a reference material curve lying on a closed streamline grow longer than the reference curve, even if the perturbation was initially shorter than this curve.

Similar behavior is seen for KAM curves in near-steady time-periodic and quasiperiodic flows. As noted earlier, nested families of KAM curves in such flows objectively indicate the presence of coherent material eddies. The stretching of material lines off a KAM curve is due to the twist (shear) across the curve, which may be even magnified by the presence of resonance islands.

In a time-aperiodic flow defined over a finite-time interval, locating at time t_0 the positions of material lines that will stretch the least over the time interval $[t_0, t]$ leads to a variational problem. As shown in Haller and Beron-Vera [2012], the solutions of this problem are distinguished material curves at time t_0 that turn out to be minimal

geodesics (shortest paths) of the metric generated by the Cauchy–Green strain tensor,

$$C_{t_0}^t(\mathbf{x}_0) = \nabla F_{t_0}^t(\mathbf{x}_0)^\top \nabla F_{t_0}^t(\mathbf{x}_0), \quad (3.3)$$

where \top denotes transpose and ∇ refers to the spatial gradient operator.

From each point \mathbf{x}_0 in the initial flow configuration, Cauchy–Green geodesics emanate in all possible directions. In fact, any pair of points on the plane are connected by a unique Cauchy–Green geodesic, which is locally the least-stretching material line out of all material lines connecting those two points (Fig. 3.4a).

Among all geodesics passing through \mathbf{x}_0 , the locally least-stretching geodesic at \mathbf{x}_0 is of particular interest. This geodesic is tangent to the direction of minimal strain at \mathbf{x}_0 . More specifically, consider

$$C_{t_0}^t \xi_i(\mathbf{x}_0) = \lambda_i(\mathbf{x}_0) \xi_i(\mathbf{x}_0), \quad 0 < \lambda_1(\mathbf{x}_0) \leq \lambda_2(\mathbf{x}_0), \quad |\xi_i(\mathbf{x}_0)| = 1, \quad i = 1, 2, \quad (3.4)$$

where $\lambda_i(\mathbf{x}_0)$ and $\xi_i(\mathbf{x}_0)$ are the i th eigenvalue and eigenvector of $C_{t_0}^t(\mathbf{x}_0)$, respectively, and $|\cdot|$ denotes Euclidean norm. Then the locally least-stretching geodesic through \mathbf{x}_0 is tangent to the weakest strain eigenvector at \mathbf{x}_0 , $\xi_1(\mathbf{x}_0)$, as shown in Fig. 3.4a.

Typical geodesics in a turbulent flow still stretch by a relatively large amount, even though they stretch less than any other curve connecting their endpoints. Most geodesics, therefore, do not act as observable transport barriers. Observable barriers, however, must necessarily run close to locally least-stretching geodesics. This means that at each point \mathbf{x}_0 of an observable transport barrier, both the tangent and the curvature of the barrier must be close to the tangent and curvature of the locally least-stretching geodesic through \mathbf{x}_0 . For short, we say that such a barrier is a material line that is *geodesically shadowed* over the time interval $[t_0, t]$.

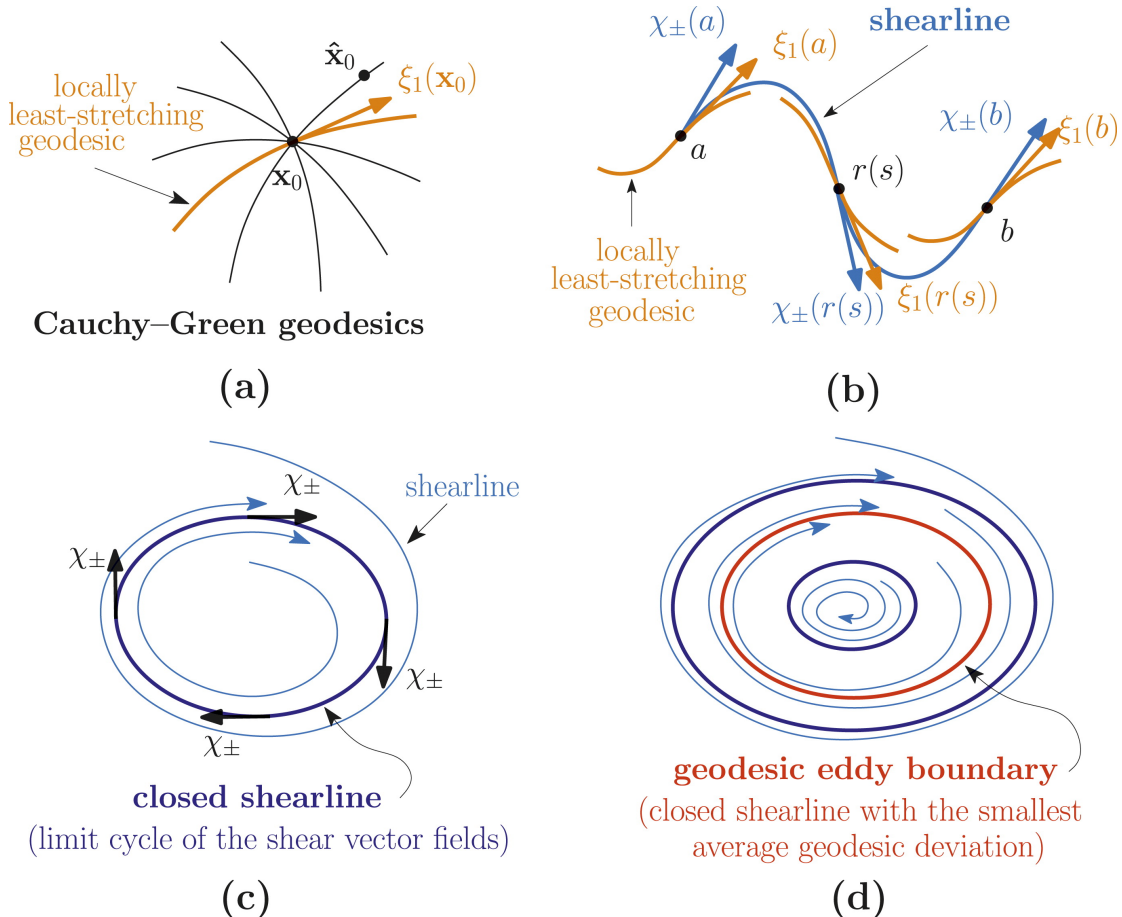


Figure 3.4: (a) Cauchy-Green geodesics emanating from an initial position x_0 , representing least-stretching curves out of all material curves connecting two initial positions, such as x_0 and \hat{x}_0 . The locally least-stretching geodesic at x_0 is tangent to the weakest strain eigenvector ξ_1 of the Cauchy-Green tensor, a quantity commonly used to measure deformation in continuum mechanics. (b) Shearlines are curves tangent to the Lagrangian shear vector fields χ_{\pm} , along which an objective (i.e., frame-independent) measure of shear is maximized. A shear barrier at time t_0 between points a and b is a shearline shadowed by locally least-stretching geodesics. (c) Closed shearlines are limit cycles of the χ_{\pm} vector fields. (d) A geodesic eddy boundary is a member of a nested limit cycle family with the smallest average geodesic deviation. The family may also just consist of one member. From Beron-Vera, Wang, et al., [2013].

3.3.3 Shear barriers

With the behavior of streamlines in the steady circular flow example in mind, it is natural to seek the transport barriers of interest as those maximizing shear. An appropriate frame-independent form of shear in unsteady flows is given by the *Lagrangian shear*, defined as the tangential projection of the linearly advected normal to a material line. As shown in Haller and Beron-Vera [2012], Lagrangian-shear-maximizing transport barriers (or *shear barriers*) over $[t_0, t]$ turn out to be geodesically shadowed trajectories of the Lagrangian shear vector fields

$$\chi_{\pm}(\mathbf{x}_0) = \alpha_1(\mathbf{x}_0)\xi_1(\mathbf{x}_0) \pm \alpha_2(\mathbf{x}_0)\xi_2(\mathbf{x}_0), \quad \alpha_i(\mathbf{x}_0) = \sqrt{\frac{\sqrt{\lambda_j(\mathbf{x}_0)}}{\sqrt{\lambda_1(\mathbf{x}_0)} + \sqrt{\lambda_2(\mathbf{x}_0)}}}, \quad i \neq j. \quad (3.5)$$

Closeness of a trajectory (or *shearline*) of (3.5) to its shadowing least-stretching geodesic at \mathbf{x}_0 can be computed as the sum of their tangent and curvature differences. This sum, the *geodesic deviation* of a shearline, can be proven to be equal to [Haller and Beron-Vera, 2012]

$$d_g^{\chi_{\pm}}(\mathbf{x}_0) = |1 - \alpha_1| + \left| \left(\alpha_1 + \frac{\lambda_1}{\lambda_2} - 1 \right) \kappa_1 \mp \alpha_2 \kappa_2 \mp \frac{\nabla \alpha_1 \cdot \chi_{\pm}}{\alpha_2} - \frac{\nabla \lambda_1 \cdot \xi_2}{2\lambda_2} \right|, \quad (3.6)$$

where

$$\kappa_i(\mathbf{x}_0) = \nabla \xi_i(\mathbf{x}_0) \xi_i(\mathbf{x}_0) \cdot \xi_j(\mathbf{x}_0), \quad i \neq j, \quad (3.7)$$

is the curvature of the curve tangent to the i th strain eigenvector field at \mathbf{x}_0 (Fig. 3.4b).

Shear barriers are either open curves (*parabolic barriers*) or closed curves (*elliptic barriers*). While sets of parabolic barriers generalize the concept of a shear jet to arbitrary unsteady flow, elliptic barriers generalize the concept of a KAM curve. As limit cycles of the shear vector field (Fig. 3.4c), elliptic barriers are robust with respect to perturbations of the underlying velocity data, and hence smoothly persist under moderate noise and small changes to the observational time interval $[t_0, t]$.

3.3.4 Eddy boundaries

If elliptic barriers occur in a nested family, the outermost barrier is the physically observed eddy boundary, enclosing the largest possible coherent water mass in the region. Outermost elliptic barriers, however, also tend to be the most sensitive to errors and uncertainties in the velocity data.

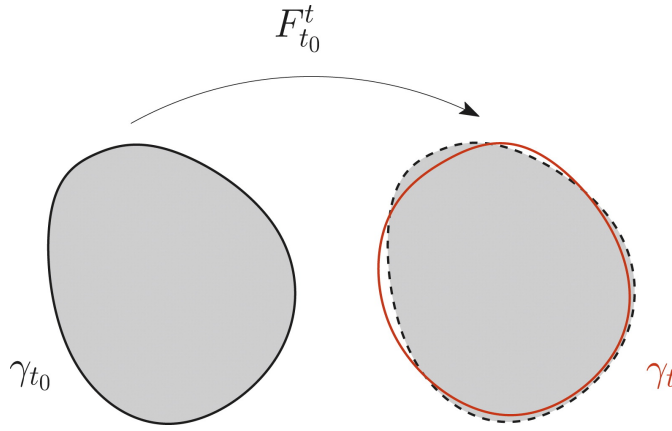


Figure 3.5: Schematics of a closed shearline γ_{t_0} computed using flow data over the time interval $[t_0, t]$. The dashed curve indicates a translated and rotated position of γ_{t_0} for reference. If the flow is incompressible, the advected material line γ_t has the same arclength, and encloses the same area, as γ_{t_0} . From Beron-Vera, Wang, et al., [2013].

To obtain a robust eddy boundary, we select the member of a nested family of closed shearlines which has the lowest average geodesic deviation, $\langle d_g^{\chi\pm} \rangle$, in the family (Fig. 3.4d). As discussed in Haller and Beron-Vera [2012], $\langle d_g^{\chi\pm} \rangle$ along an elliptic barrier measures how much the barrier extraction procedure has converged over the time interval $[t_0, t]$. Accordingly, an elliptic barrier with the lowest $\langle d_g^{\chi\pm} \rangle$ value in a nested family of barriers is the best eddy barrier candidate. As such, it is also the least susceptible to errors and uncertainties. Based on these considerations, *geodesic eddy detection* comprises the algorithmic steps described in section 3.3.6.

We finally note that, in incompressible flows, elliptic barriers have two important

conservation properties: 1) they preserve the area they enclose, and 2) they reassume their initial arclength at time t (Fig. 3.5) [Haller and Beron-Vera, 2012]. These two properties make elliptic barriers ideal boundaries for coherent eddy cores.

3.3.5 Velocity data

Eulerian eddy detection is routinely applied to satellite altimetry measurements, a unique source of SSH data for global monitoring of mesoscale variability available continually since the early 1990s [Fu et al., 2010]. The basis for this is the assumption of a geostrophic balance in which the pressure gradient is caused by differences in SSH, with the resulting currents reflecting an integral dynamic effect of the density field above the thermocline.

The velocity field $\mathbf{v}(\mathbf{x}, t)$ in (3.1) is thus assumed to be of the form:

$$\mathbf{v}(\mathbf{x}, t) = \left(-\frac{g}{f} \frac{\partial \eta(\mathbf{x}, t)}{\partial y}, \frac{g}{f} \frac{\partial \eta(\mathbf{x}, t)}{\partial x} \right). \quad (3.8)$$

Here $\mathbf{x} = (x, y)$ denotes position on a plane with Cartesian x (y) zonal (meridional) coordinate; $\eta(\mathbf{x}, t)$ denotes SSH; f is the Coriolis parameter (twice the local vertical component of the Earth's angular velocity); and g is the acceleration of gravity. While we choose to work on a planar domain here for simplicity, the underlying geodesic transport theory also applies to flows on a sphere [Haller and Beron-Vera, 2012].

The background η -component is steady, given by a mean dynamic topography constructed from altimetry data, in-situ measurements, and a geoid model [Rio and Hernandez, 2004]. The perturbation η -component is transient, given by altimetric SSH anomaly measurements provided weekly on a 0.25° -resolution longitude–latitude grid. This perturbation component is referenced to a 7-yr (1993–1999) mean, obtained from the combined processing of a constellation of available altimeters [Le Traon et al., 1998].

3.3.6 Numerical implementation

Geodesic eddy detection for the flow defined by (3.1) and (3.8) involves the following computational steps:

1. Fix a grid \mathcal{G}_0 of initial positions in the flow domain of interest, and time scale T over which coherent eddies are to be tracked. For each initial condition $\mathbf{x}_0 \in \mathcal{G}_0$, integrate the nonautonomous dynamical system (3.1) from an initial time t_0 to time $t = t_0 + T$. This leads to a discrete approximation of the flow map $F_{t_0}^t$ (3.2) over the grid \mathcal{G}_0 .
2. Compute the deformation gradient field $\nabla F_{t_0}^t(\mathbf{x}_0)$. Using central differences over a rectangular \mathcal{G}_0 this can be achieved as follows. Let $\mathbf{x}_t^{i,j} = (x_t^{i,j}, y_t^{i,j})$ denote the image under the flow map $F_{t_0}^t$ of a point $\mathbf{x}_0^{i,j} = (x_0^{i,j}, y_0^{i,j}) \in \mathcal{G}_0$. Then

$$\nabla F_{t_0}^t(\mathbf{x}_0^{i,j}) = \begin{bmatrix} \frac{x_t^{i+1,j} - x_t^{i-1,j}}{x_0^{i+1,j} - x_0^{i-1,j}} & \frac{x_t^{i,j+1} - x_t^{i,j-1}}{y_0^{i,j+1} - y_0^{i,j-1}} \\ \frac{y_t^{i+1,j} - y_t^{i-1,j}}{x_0^{i+1,j} - x_0^{i-1,j}} & \frac{y_t^{i,j+1} - y_t^{i,j-1}}{y_0^{i,j+1} - y_0^{i,j-1}} \end{bmatrix}. \quad (3.9)$$

3. Construct the Cauchy–Green strain tensor field $C_{t_0}^t(\mathbf{x}_0)$ defined in (3.3), and compute its eigenvalue and eigenvector fields, $\lambda_i(\mathbf{x}_0)$ and $\xi_i(\mathbf{x}_0)$, as defined in (3.4).

The following are explicit formulas:

$$\lambda_1 = \frac{1}{2}T - \sqrt{\frac{1}{4}T^2 - D}, \quad \lambda_2 = \frac{1}{2}T + \sqrt{\frac{1}{4}T^2 - D}, \quad (3.10)$$

where T and D denote trace and determinant of $C_{t_0}^t(\mathbf{x}_0)$, respectively, and

$$\xi_1 = \begin{bmatrix} 0 & 1 \\ -1 & 0 \end{bmatrix} \xi_2, \quad \xi_2 = \begin{pmatrix} C_{12} \\ \frac{\sqrt{(C_{11} - \lambda_2)^2 + C_{12}^2}}{C_{11} - \lambda_2} \\ \frac{\sqrt{(C_{11} - \lambda_2)^2 + C_{12}^2}}{C_{11} - \lambda_2} \end{pmatrix}, \quad (3.11)$$

where C_{ij} is the ij th entry of $C_{t_0}^t(\mathbf{x}_0)$.

4. Compute the trajectories of the shear vector fields $\chi_{\pm}(\mathbf{x}_0)$, defined in (3.5), by solving the differential equation

$$\frac{d\mathbf{x}_0(s)}{ds} = \left(\chi_{\pm}(\mathbf{x}_0(s)) \cdot \frac{d\mathbf{x}_0(s - \Delta)}{ds} \right) \chi_{\pm}(\mathbf{x}_0(s)), \quad (3.12)$$

with Δ denoting the integration step in s . The factor multiplying $\chi_{\pm}(\mathbf{x}_0(s))$ in (3.12) removes orientational discontinuities in $\chi_{\pm}(\mathbf{x}_0(s))$ arising from the lack of a global orientation for $\xi_i(\mathbf{x}_0)$ [cf. Haller and Beron-Vera, 2012, for details].

5. In the phase portrait of $\chi_{\pm}(\mathbf{x}_0)$, locate all nested families of limit cycles. Such closed shearlines can be located as fixed points of Poincare maps defined on one-dimensional sections locally transverse to trajectories of (3.12). To construct a Poincare map, one considers a trajectory with initial condition on the section and observes the location at which this trajectory first returns to the section; a fixed point is given by an initial condition that is mapped onto itself [cf., e.g., Ottino, 1989, Section 5.5].
6. In each nested family of limit cycles, locate a *geodesic eddy boundary* at time t_0 as the limit cycle with the lowest average geodesic deviation $\langle d_g^{\chi_{\pm}}(\mathbf{x}_0) \rangle$, with $d_g^{\chi_{\pm}}(\mathbf{x}_0)$ defined in (3.6).
7. To track geodesic eddies in time, find their time t positions by applying the flow map $F_{t_0}^t$ to geodesic eddy boundaries identified at time t_0 .

3.3.7 Numerical details

All trajectory integrations in this paper were carried using a stepsize-adapting fourth-order Runge–Kutta method. The interpolations involved were obtained from a cubic scheme. Differentiation was executed using finite differences on an auxiliary grid of

four points neighboring each point in a regular grid of size 2000^2 . Geodesic eddy detection was initialized by searching for regions possibly including closed shearlines. This process was started on a coarser grid of points covering the whole geographical domain of interest. Once a potential geodesic eddy region was identified, a refined calculation in that region was conducted. This involved launching shearlines on a straight segment of 2500 grid points. The Poincare section was appropriately located across the region to construct a first return map onto this segment for the computation of limit cycles.

3.4 Results

We consider a region of the South Atlantic subtropical gyre, bounded by longitudes [14°W, 9°E] and latitudes [39°S, 21°S], which encompasses possible routes of Agulhas rings (dashed rectangle in each panel of Figs. 3.7 and 3.8). The same region has been analyzed by Beron-Vera et al. [2008], who showed that the finite-time Lyapunov exponent, a widely used Lagrangian diagnostic [Haller, 2001; Peacock and Dabiri, 2010], does not reveal coherent material eddies. More recently, the same area was also studied by Lehahn et al. [2011], who reported observations of a nearly isolated mesoscale chlorophyll patch, traversing the region in the period from November 2006 to September 2007.

We apply geodesic eddy detection to altimetry-derived currents (cf. section 3.3.5) in the selected region starting on $t_0 = 24$ November 2006, with the detection time scale set to $T = t - t_0 = 90$ d. Following the algorithmic steps described in section 3.3.6, with numerical details given in section 3.3.7, geodesic eddy detection isolates two coherent material eddies (denoted *geodesic eddies*). The boundary of the first eddy is obtained as a limit cycle of the $\chi^+(\mathbf{x}_0)$ shear vector field, with an anticyclonic polarity. The

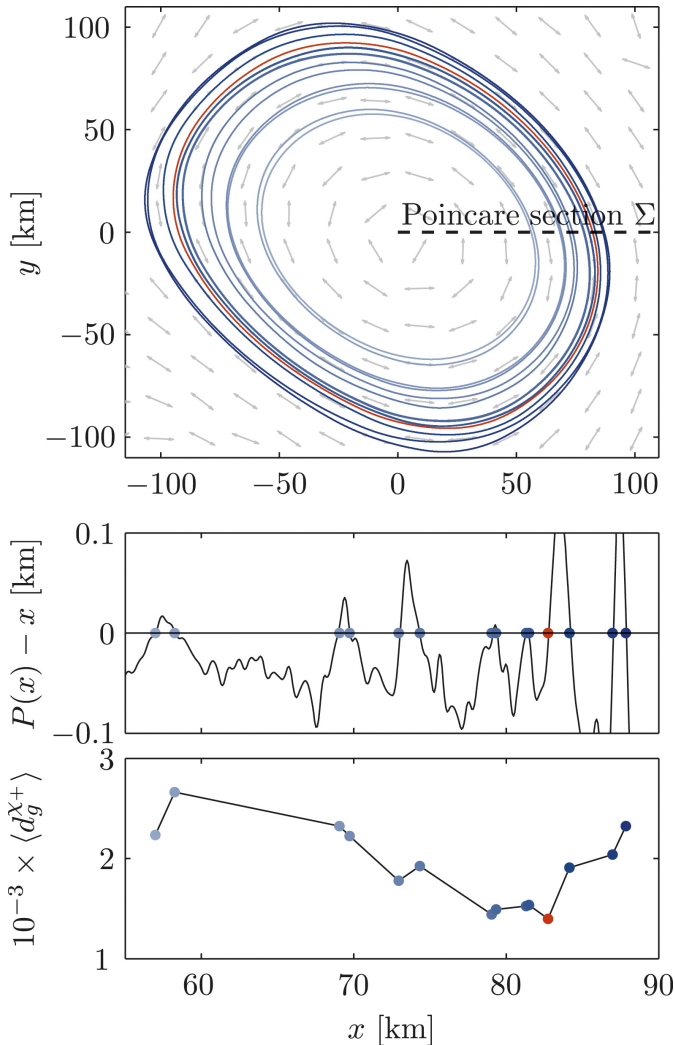


Figure 3.6: Identification of a coherent material eddy boundary on $t_0 = 24$ November 2006 from geodesic eddy detection with detection time scale $T = t - t_0 = 90$ d. Marked in red, the eddy boundary is obtained as an average-geodesic-deviation-minimizing member of a nested family of limit cycles of the Lagrangian shear vector field χ_+ . The full limit cycle family is shown in blue in the upper panel, with grey arrows indicating the χ_+ vector field. The middle panel shows the first return (Poincare) map, $x \mapsto P(x)$, onto a section Σ locally transverse to χ_+ vector field. Dots indicate the fixed points of the Poincare map, $P(x) = x$, corresponding to each of the limit cycles. The bottom panel shows the distribution of the average geodesic deviation over the limit cycles. From Beron-Vera, Wang et al., [2013].

boundary of the second eddy is recovered as a limit cycle of the $\chi^-(\mathbf{x}_0)$ field, with a cyclonic polarity. The extraction of the anticyclonic eddy boundary is detailed in Fig. 3.6. The geographical locations of the two eddies identified on 24 November 2006 are shown in the upper-left panel of Fig. 3.7, with the anticyclonic eddy indicated in red and the cyclonic eddy in blue.

The remaining panels in the left column of Fig. 3.7 show several later advected positions of the two geodesic eddies to illustrate their coherence. Note the complete lack of material filamentation or leakage from these eddies over 90 d. This can be seen in more detail in the left column of Fig. 3.9, which shows the two eddies on the detection date and 90 d later. Closed material lines like the boundaries of these eddies are highly atypical in an otherwise turbulent flow. Their role is indeed best compared to the role of KAM curves in time-periodic or quasiperiodic flows.

Remarkably, the coherence of the anticyclonic eddy is preserved well over the 90-d period on which our computations were performed (Fig. 3.7, left column). Indeed, this eddy preserves its coherence even 540 d later, exhibiting only translation, rotation, and minor deformation without noticeable leakage, stretching or folding. The remarkable coherence of this eddy can attributed to its interior being foliated by a large number of nested closed shearlines. The inner shearlines are less exposed to the ambient turbulent mixing than the outer ones, thereby providing a stability buffer for the eddy. By contrast, the boundary of the cyclonic eddy is the only member of a family of nested closed shearlines. With the stability buffer absent, the boundary of this eddy exhibits filamentation immediately after 90 d.

For comparison, the remaining columns of Fig. 3.7 illustrate the accuracy of the two most widely used Eulerian eddy diagnostics and one recent Lagrangian eddy diagnostic on the same dataset.

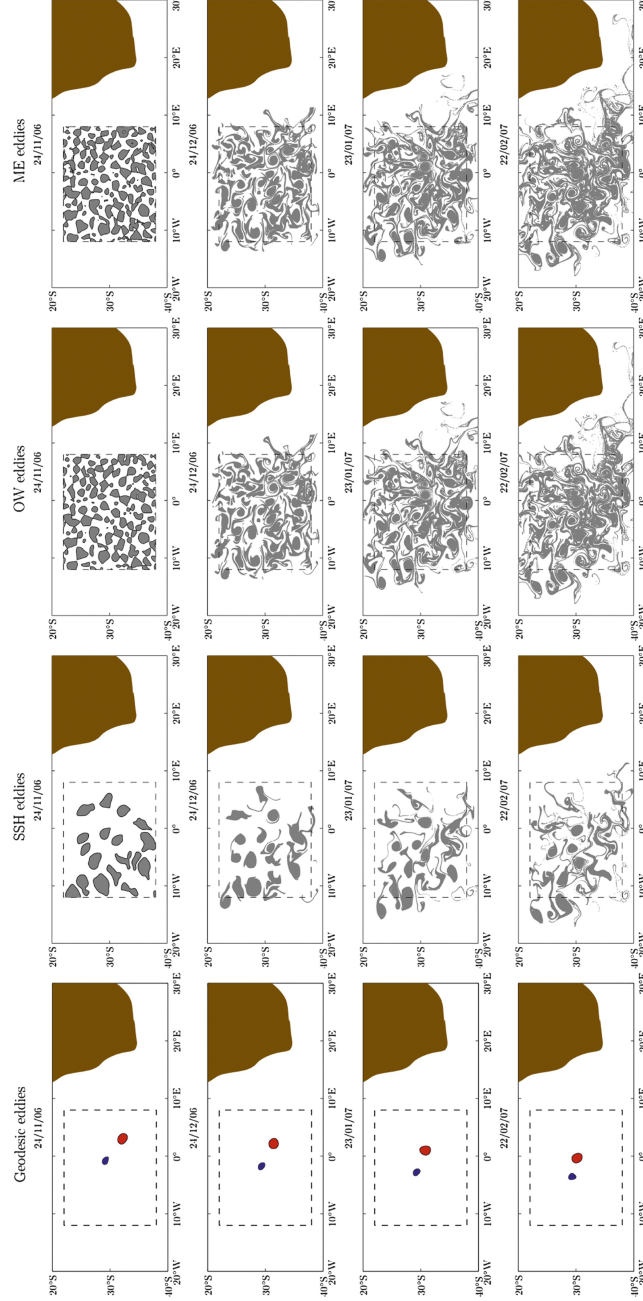


Figure 3.7: (left) Selected snapshots of the 90-day evolution of fluid inside eddies identified by geodesic eddy detection; (middle left) the method of Chelton et al. [2011b] with $U/c > 1$ over at least 90 days; (middle right) the OkuboWeiss (OW) criterion; and (right) the criterion of Mézic et al. [2010]. From Beron-Vera, Wang et al., [2013].

The middle-left column of Fig. 3.7 shows the material evolution of eddies (denoted *SSH eddies*) obtained from the method of Chelton et al. [2011b], who argue that closed SSH contours can play roughly the same role in inhibiting transport as closed streamlines do in steady flows. Chelton et al. [2011b] suggest that this should be the case when the rotational speed of the eddy, U , dominates its translational speed, c [cf. also Early et al., 2011]. More specifically, Chelton et al. [2011b] propose that $U/c > 1$ should signal the presence of a coherent eddy, as opposed to a linear wave ($U/c < 1$). However, as revealed by the Lagrangian evolution of closed SSH contours in the upper-middle row of Fig. 3.7 (all with $U/c > 1$ over at least 90 d), most such contours rapidly stretch and fold, exhibiting leakage and filamentation that disqualifies them as physically reasonable coherent material eddy boundaries. Only two SSH eddies approximate coherent geodesic eddies on 24 November 2006 (Fig. 3.9, middle-left column). However, both eddies exhibit almost instantaneous material filamentation beyond that date. The panels in the right column of Fig. 3.8 further demonstrate the inability of an SSH eddy with $U/c > 1$ for a period of at least 540 d to trap and carry within water in a coherent manner. We conclude that the SSH contour approach, with or without the $U/c > 1$ requirement,¹ shows major inaccuracies in detecting material eddies, including the overestimation of coherent material eddy cores, as well as the generation of a large number of false positives.

The middle-right column of Fig. 3.7 documents similar findings for the Okubo–Weiss criterion [Okubo, 1970; Weiss, 1991], the other broadly used frame-dependent Eulerian method for eddy identification. Relative to a reference frame, this method identifies eddies (denoted *OW eddies*) as regions of fluid where vorticity dominates over strain. The regions indicated in black qualify as OW eddies in the Earth’s frame

¹Indeed, $U/c \rightarrow \infty$ in the flow defined in Fig. 3.1.

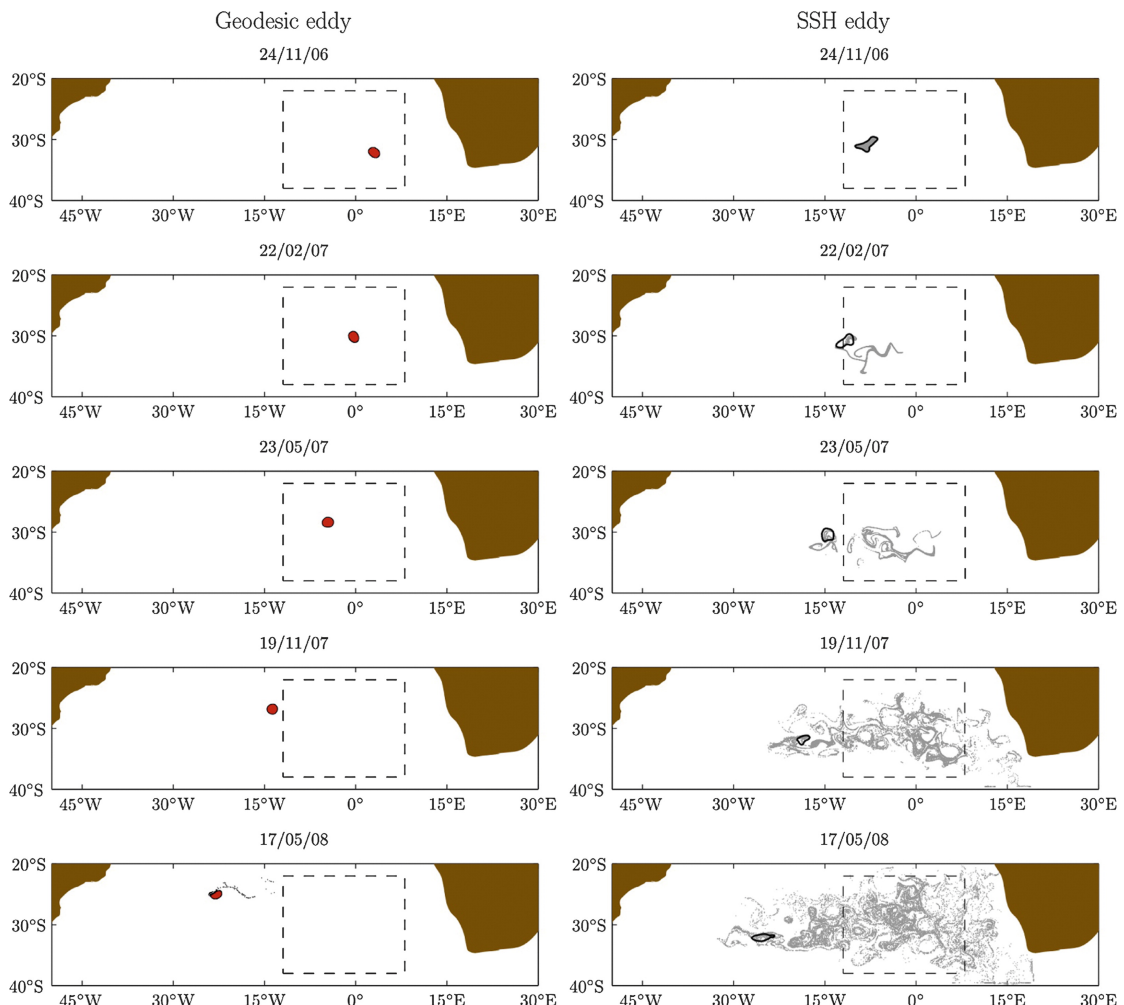


Figure 3.8: Selected snapshots of the 540-day evolution of fluid inside (left) a geodesic eddy and (right) an SSH eddy. The instantaneous SSH contour that defines the SSH eddy, which has $U/c > 1$ over at least 540 days, is indicated. From Beron-Vera, Wang et al., [2013].

on 24 November 2006. In a similar manner to SSH eddies, coherent geodesic eddies on 24 November 2006 are roughly approximated by two OW eddies, which deform rapidly after that date (Fig. 3.9, middle-right column). The remaining OW eddies are false positives for Lagrangian eddies: they undergo intense stretching and filamentation, before fully dispersing a few months later. We conclude that when used for coherent material eddy detection, the Okubo–Weiss approach also shows major inaccuracies. This includes the inability to capture actual coherent eddies accurately, as well as well as the tendency to generate numerous false positives. False negatives also arise once threshold values (not discussed) are introduced for the Okubo–Weiss parameter.

Recent application of Okubo-Weiss criterion in studying the physical-biological interactions of the Southern Ocean also gives rise to combined Eulerian-Lagrangian eddy retention diagnostics [d’Ovidio et al., 2013]. In that study, instantaneous Okubo-Weiss parameters are calculated along trajectories of fluid particles over time, and the change of sign of the parameter signals the trapping inside, or escaping from, a coherent eddy of the fluid. Similar philosophy can be found in the study by van Sebille et al. [2010], who calculate the relative vorticity along fluid particles released from the Agulhas Current flowing into the South Atlantic Ocean in a numerical model, and find out that along-trajectory vorticity keeps decreasing over time, which implies that Agulhas rings decay fast. Another advanced, combined Euler-Lagrangian criterion in isolating oceanic rotational or non-rotational features is the spin parameters (e.g., [Doglioli et al., 2006]), defined as $\Omega = \frac{\langle u'dv' - v'du' \rangle}{2\Delta EKE}$, where EKE denotes the eddy kinetic energy ($\langle u'^2 \rangle + \langle v'^2 \rangle$)/2. An essential difference between the spin parameter calculation and other two methods is that Ω is an average value over a fixed time window, thereby incorporating more Lagrangian information. However, all these methods require Eulerian fingerprints from the flow field, which depends on the reference frame chosen and often fails to reveal

material response, and are therefore yet to be tested on detecting isolated material eddies.

We now proceed to consider the application of the more recent Lagrangian eddy diagnostic of Mézic et al. [2010]. This approach views a fluid region at time t_0 as a *mesoelliptic* region if the eigenvalues of the deformation gradient $\nabla F_{t_0}^t(\mathbf{x}_0)$ are purely imaginary for all \mathbf{x}_0 in that region. Even though this approach is Lagrangian, the eigenvalues of $\nabla F_{t_0}^t(\mathbf{x}_0)$ are frame-dependent, and hence the resulting eddy candidates are not objective. As noted in Mézic et al. [2010], mesoelliptic regions approach Okubo–Weiss elliptic regions as t tends to t_0 . For increasing $T = t - t_0$, mesoelliptic regions (denoted *ME eddies*) tend to rapidly fill the full domain of extraction, as most initial conditions accumulate enough rotation in their evolution to create imaginary eigenvalues for $\nabla F_{t_0}^t(\mathbf{x}_0)$. As a result, identifying ME eddies over time scales longer than a few days becomes unrealistic. Instead, we have chosen to use $T = 4$ d, following Mézic et al. [2010].

Shown in the right column of Fig. 3.7, ME eddies resemble OW eddies closely, as expected. In a fashion similar to OW eddies, only two ME eddies approximate the geodesic eddies detected on 24 November 2006. Just as OW eddies, these ME eddies develop substantial material filamentation beyond that date (Fig. 3.9, right column).

Independent observational evidence for the Lagrangian eddies can be inferred from surface ocean chlorophyll concentration in the South Atlantic. Figure 3.10 shows a sequence of snapshots of chlorophyll concentration derived from the MODIS (Moderate Resolution Imaging Spectroradiometer) sensor aboard the *Aqua* satellite. Note the patch of high chlorophyll concentration, discussed in Lehahn et al. [2011], which translates inside the anticyclonic geodesic eddy detected on 24 November 2006 from this date through 23 May 2007. Due to the lack of filamentation in the ring boundary, the

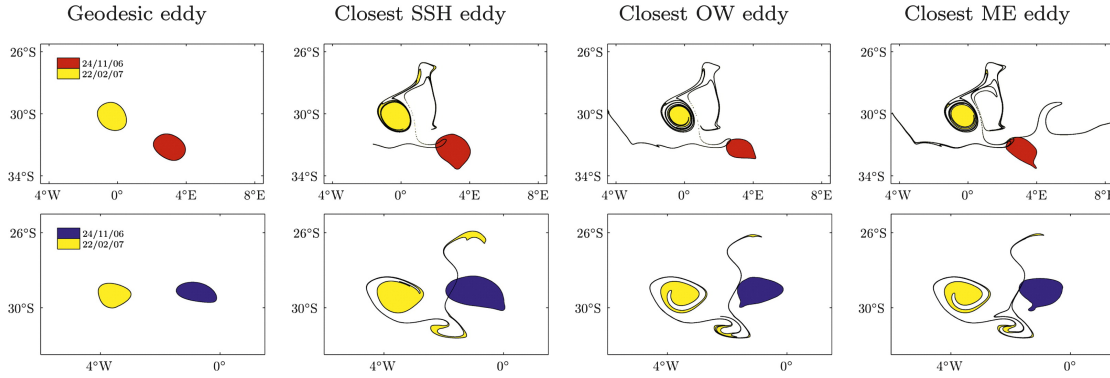


Figure 3.9: Fluid positions of eddy candidates obtained from different detection methods on $t_0 = 24$ Nov 2006 and 90 days later. (middle left, middle right, and right columns) The red and blue eddy candidates by other eddy detection methods are the closest ones to (left) the similarly colored geodesic eddies. From Beron-Vera, Wang et al., [2013].

diffusion of chlorophyll is moderate and remains confined to the periphery of the ring. This observation confirms the ability of Lagrangian eddies to preserve the concentration peaks of diffusive substances over long distances.

We now derive estimates for the volume of water carried by eddies obtained from different methods. For simplicity, we assume that the eddies are quasigeostrophic and equivalent barotropic, with their base lying on the 10°C -isotherm at a depth of 400 m [Garzoli et al., 1999]. We argue that such a ring depth value should be considered as a lower bound. Indeed, Souza et al. [2011a] reported that mature Agulhas ring trapping depth can extend to 1000 m based on float-profiling hydrography. Under these assumptions, we obtain the volume estimates in Table 3.1 for a single day, with other dates giving similar results. The volume estimates are grouped by the polarity of the eddies involved, with anticyclonic eddies being candidates for Agulhas rings.

OW eddies have been reported to overestimate eddy transport rates based on comparisons with other Eulerian estimates [Souza et al., 2011b], as opposed to comparisons with observed material transport. The volume estimates in Table 3.1 show that even other Eulerian indicators, such as closed streamlines of the SSH field with $U/c > 1$

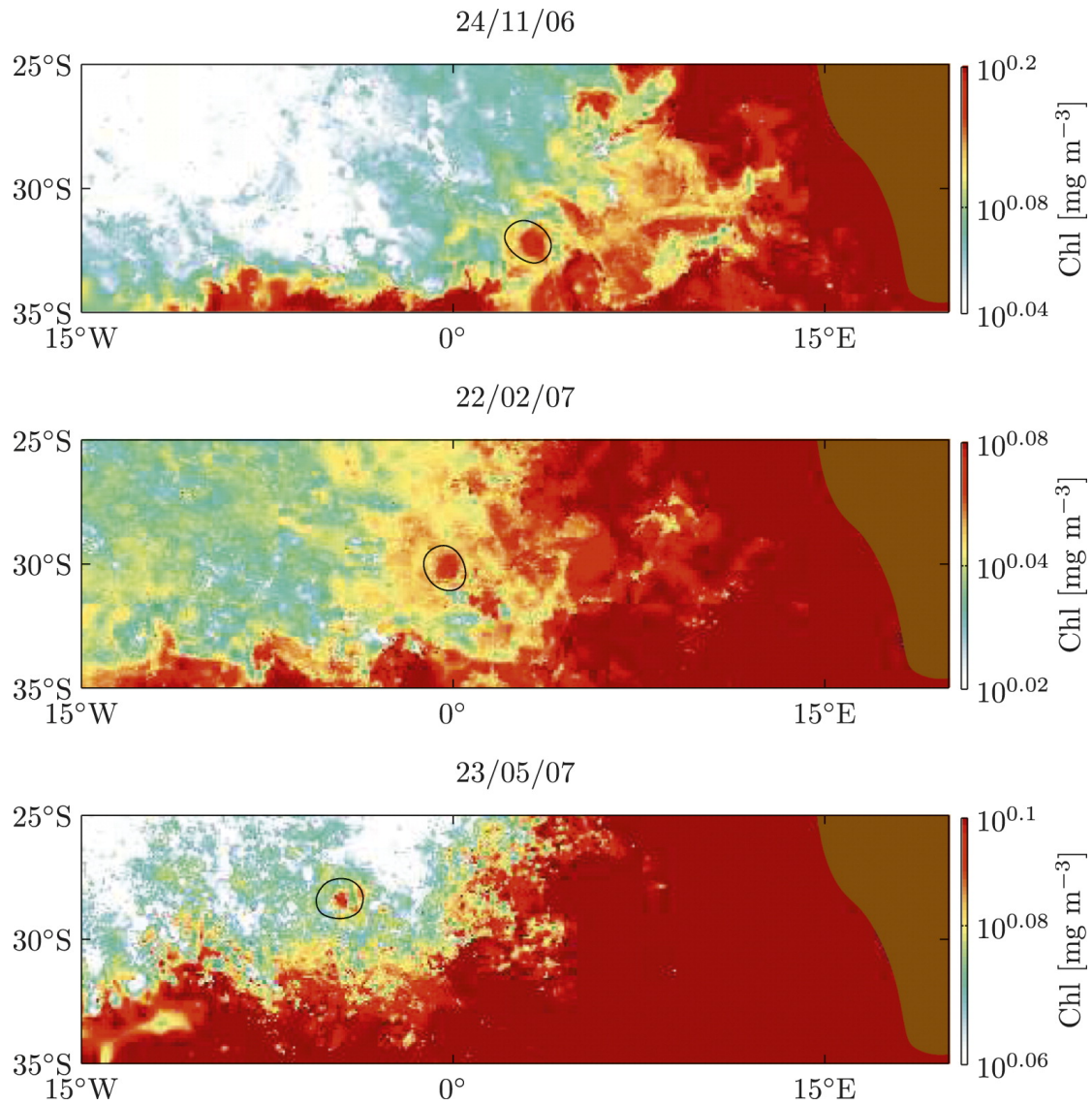


Figure 3.10: Sequence of snapshots of satellite-derived surface ocean chlorophyll concentration with the boundary of the anticyclonic geodesic eddy detected on 24 Nov 2006 overlaid. The color scale varies from figure to figure to aid the visualization of chlorophyll anomalies. From Beron-Vera, Wang et al., [2013].

	Geodesic eddies	SSH eddies	OW eddies	ME eddies
Cyclonic	0.5	11.5	19.2	19.8
Anticyclonic	1.0	23.5	35.4	37.2

Table 3.1: Estimated volume [10^4 km^3] of water warmer than 10°C carried by eddies on 24 November 2006, grouped by their polarity, as identified by different eddy detection methods [Beron-Vera, Wang et al., 2013].

as proposed by Chelton et al. [2011b], significantly overestimate the volume of coherent material eddies. The same observation applies to the Lagrangian indicator introduced by Mézic et al. [2010]. A recent set-theoretical study [Froyland et al., 2012] of a three-dimensional Agulhas ring produced by an ocean general circulation model also yields results similar to those from the Eulerian techniques surveyed here. This provides further illustration that Lagrangian approaches also lead to exaggerated transport estimates, if they fail to capture the frame-independent details of material stretching.

Note that the coherently transported water mass (Table 3.1, left column) is carried mostly by an anticyclonic geodesic eddy. As an impermeable whirling body of water showing minor deformation over roughly a year-and-a-half period, such an eddy represents an exact mathematical construction of what has been (somewhat loosely) defined as a mesoscale ring in oceanography. Furthermore, this particular ring is best referred to as an Agulhas ring, as its backward-time advection (not shown) to the Agulhas retroflection area confirms. Thus, by Table 3.1, actual transport of warm and salty water by (coherent material) Agulhas rings is about one order of magnitude less than what can be deduced from available nonobjective eddy detection methods.

To illustrate the general validity of these conclusions, we present in Table 3.2 the results from a more extended survey of the volume carried by geodesic and SSH eddies in the years 1997, 2002, and 2007. In agreement with the results discussed above, the volume of eddies identified in the Eulerian frame is found to be always significantly

	Year 1997	Year 2002	Year 2007
Geodesic eddies	7 (5)	10 (9)	9 (7)
SSH eddies	63 (29)	62 (36)	57 (27)

Table 3.2: Estimated volume [10^4 km^3] of water warmer than 10°C carried by eddies along the years. Indicated in parenthesis is the volume estimate corresponding to eddies with anticyclonic polarity [Beron-Vera, Wang et al., 2013].

larger than that of geodesic eddies, thereby overestimating the volume of water that can be transported coherently. Clearly, to correctly assess the role of geodesic eddies in the Agulhas leakage, a detailed survey is needed. This should include a backward tracking of the geodesic eddies to determine their origins.

We reiterate that coherent material transport (as opposed to the widespread dispersion of SSH, OW and ME eddies observed in Fig. 3.7) is the relevant metric for quantifying the transport of diffusive quantities, such as salinity and temperature. Indeed, the disintegration of SSH, OW and ME eddy candidates is accompanied by the erosion of salinity and temperature differences between the water they carry in their wake and the water they traverse.

The use of filters, thresholds, and size-limits would undoubtedly reduce the eddy count and transport estimates obtained from nonobjective detection methods. Such post-processing steps, however, are largely heuristic: they exploit the high sensitivity of the underlying nonobjective detection methods to bring them in line with each other, and with sporadic in-situ hydrographic measurements [Souza et al., 2011b]. We stress that geodesic eddy detection has no such tuning parameters, and the underlying mathematics (structural stability of limit cycles) renders its conclusions robust.

3.5 Concluding remarks

We have introduced a new method, geodesic eddy detection, for the objective (frame-independent) identification and tracking of mesoscale eddies in the ocean. In short, geodesic eddy boundaries are limit cycles of the Lagrangian shear vector field that are the closest to least-stretching geodesics of the Cauchy–Green strain tensor. When tracked as material lines, geodesic eddy boundaries in a two-dimensional incompressible flow preserve their enclosed area and arclength, acting as impenetrable islands of minimal deformation in an otherwise turbulent flow. This in turn enables them to preserve the concentration of diffusive tracers they carry for extended periods. By the structural stability of limit cycles, geodesic eddy boundaries are robust with respect to velocity measurement errors and changes in their detection period.

Using geodesic eddy detection, we have isolated highly coherent Agulhas rings that carry warm and salty water over large distances. Remarkably, one geodesic eddy constructed from three months of data was found to show no sign of disintegration up to one year and a half. By comparison, eddies identified by two currently used Eulerian methods and one recent Lagrangian diagnostic showed clear signs of leakage and stretching within weeks. The volume of water that such eddies would transport if they were coherent was found to be about an order of magnitude larger than the volume of water transported by actual coherent material eddies. Satellite observations of a highly coherent chlorophyll patch provided independent confirmation that geodesically detected Agulhas rings carry diffusive substances over large distances.

We argue that geodesically detected Agulhas rings are better positioned to impact AMOC than their counterparts obtained from nonobjective methods. Indeed, the latter rings lack a coherent material boundary and hence the ability to deliver warm and salty

water effectively into the upper arm of AMOC. Our argument does assume that the geodesically detected Agulhas rings are not trapped within the subtropical gyre. A verification of this assumption is currently underway.

The present analysis is based on forward-time integration of the surface velocity field, and hence is appropriate for a historical assessment of eddy formation and transport. In a real-time operational setting, geodesic eddy boundaries are determined from backward integration, i.e., from reverse fluid motion available up to the present time. Undoubtedly, both the forward-time and the backward-time Lagrangian analyses are computationally more demanding than an assessment of the SSH field, either instantaneous or over time. By nature, however, Lagrangian calculations are highly parallelizable, benefiting from up to two orders of magnitude speed-ups on multi-processor clusters [Garth et al., 2007; Conti et al., 2012].

In our view, an investment in additional computational resources is well justified by the objectivity of the results, which promises a better assessment of the role of transport by mesoscale eddies in global ocean circulation and climate.

In the next chapter, we extend geodesic eddy detection to the nearly 20 year long (1992-2013) records of satellite altimetry within the Agulhas corridor [Goni et al., 1997]. The purpose of the study is to quantify long-range transport of Agulhas leakage achieved by coherent Agulhas rings. To this end, the coherence time scale T is also increased from 90 to 360 days. The indication and significance of the obtained material ring transport will be discussed.

Chapter 4

Coherent transport across the South Atlantic

4.1 Overview

This chapter extends the identification and tracking of coherent Lagrangian eddies of the Agulhas Current from a specific time interval in previous chapter to a 20 year long period (1992-2013), aiming to objectively investigate the role of eddies in coherently transporting Agulhas leakage across the South Atlantic. In particular, we apply the geodesic eddy detection to nearly the whole available altimetry record, expand the coherence time scales from 3 months to half and one year, isolate eddies capable of preserving material coherence for the longest time, and assess their stability through their lifetimes. Eddies are found to acquire material coherence near the Walvis Ridge, which implies the impact of intense turbulent diffusion within the Cape Basin to initiation of material coherence. One to four coherent Lagrangian eddies are identified annually with diameters ranging from 40 to 280 km. Among these, 23 are found to contain robust eddy cores of about 50 km in diameter and with at least 30% of core water traceable to the Indian Ocean. These eddy cores travel across the South Atlantic subtropical gyre with minor filamentation, however only one such core is found to pour its contents on the North Brazil Current. While the ability of mesoscale eddies to carry

Agulhas leakage coherently across the South Atlantic is supported by our study, this is much more restricted than suggested by earlier ring transport assessments. This chapter is published in *Geophysical Research Letters* [Wang et al., 2015b].

4.2 Background

Mesoscale eddies are widely viewed as potential agents of long-range water transport (e.g., Robinson [1983]). Agulhas rings, in particular, have long been thought as conduits for the leakage of warm and salty Indian Ocean water into the South Atlantic [de Ruijter et al., 1999; Gordon, 1986; Lutjeharms, 2006; Richardson, 2007; van Sebille and van Leeuwen, 2007] and as such contributors to the maintainance of the meridional overturning circulation in the Atlantic [Gordon, 1986; Weijer et al., 2002; Knorr and Lohmann, 2003; Peeters et al., 2004; Beal et al., 2011]. The role of rings in transporting Agulhas leakage was emphasized by Gordon and Haxby [1990], who argue that the rings, after being shed from the Agulhas retroflection as the result of occasional Indian-Ocean-entrapping occlusions, will enter the Brazil Current system and that their contents can be transferred to the northern hemisphere gyre through the North Brazil Current (Figure 4.1).

This long-range transport view on Agulhas rings has been challenged ever since. Ring signatures inferred from the Geosat ERM data indicates that large volume of water is lost from rings as they reach the western South Atlantic [Byrne et al., 1995]. In parallel, Schouten et al. [2000] argue that the rapid decay of Agulhas rings is evident in the Cape Basin and that ring contributions to the inter-ocean exchange are attributed to ring decay processes instead of ring trapping. By analyzing 14 years of satellite altimetry record, Dencausse et al. [2010] propose that rings plays a more minor role in Agulhas leakage due to their early dissipation in the Cape Basin. Besides observational

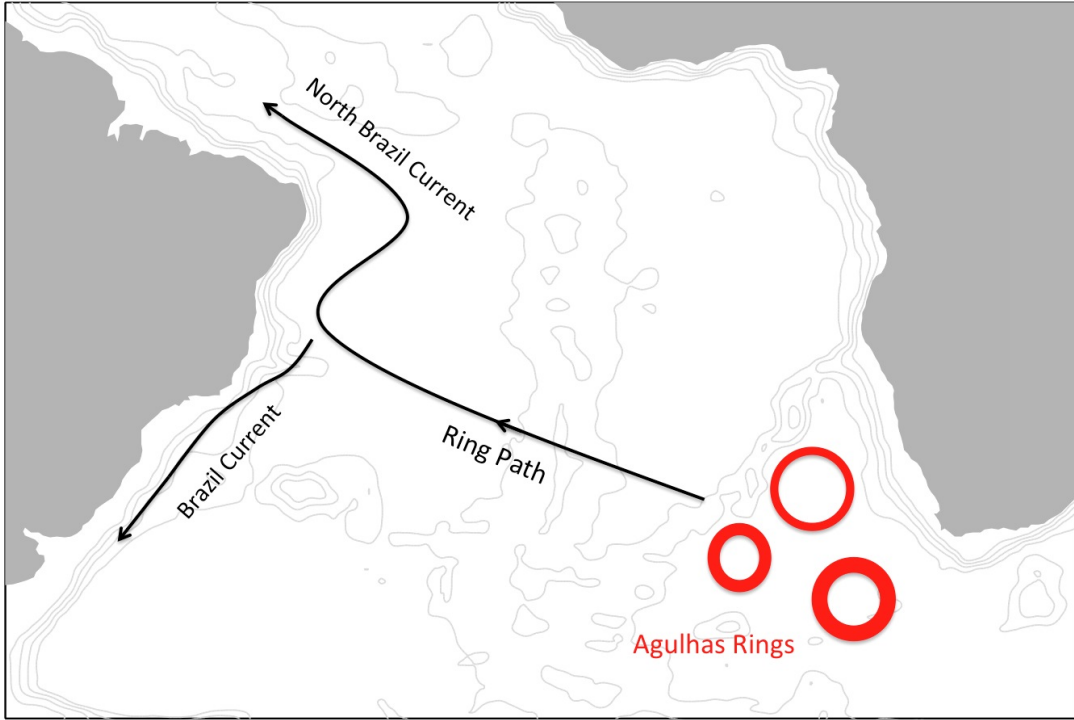


Figure 4.1: Scenario of Gordon and Haxby [1990]: After formation, Agulhas rings cross the South Atlantic basin and enter the brazil Current system. The ring contents can be transferred to northern hemisphere by the North Brazil Current.

studies, numerical experiments impose challenges on long-range transport view of rings as well. de Steur et al. [2004] state that rings are not effective in trapping passive tracers. Lagrangian analysis of numerical particles suggests that majority of the Agulhas leakage is not in rings at all [Doglioli et al., 2006], and the roles of filaments and other non-rotating forms are dominant in Indian Ocean water intrusion into Atlantic [van Sebille et al., 2010]. Most of these conclusions, however, are drawn from Eulerian or combined Eulerian-Lagrangian eddy diagnostics, the shortcomings of which are highlighted in the previous chapter. To objectively test the ability of long-range transport by rings, structures of interest should be unambiguously located, namely, eddies with persistent material cores. In this chapter, we extract mesoscale coherent material eddies

from geostrophic current inferred from the over two decade long record of satellite altimetry measurements of sea surface height (SSH), analyse their life cycles, construct a time series of coherent water transport, and evaluate the significance of the obtained transport estimates. We track, in forward direction till the time of their demise and in backward direction to the time of their genesis, of eddy cores detected with the largest possible coherence time scales. These cores coherently transport the enclosed fluid with no visible leakage through the flow domain for the whole extent of their lifetimes. Eddies revealed from their Eulerian footprints, as is the case of the rings considered by Gordon and Haxby [1990], do not possess this property [Beron-Vera, Wang et al., 2013], which is critical to assess the validity of *Gordon and Haxby's* [1990] long-range transport view on Agulhas rings.

4.3 Methodology

Haller and Beron-Vera [2013, 2014] consider exceptional material loops in turbulent flow that form the centerpieces of thin material belts exhibiting no leading order change in averaged stretching as the widths of the belts are varied. Solutions to this variational problem are material loops such that each of their subsets is stretched by a unique factor λ when the loops are advected from time t_0 to time t . Being uniformly stretching, these λ loops resist the exponential stretching typical material loops experience in turbulence. Represented as closed curves $s \mapsto x_0(s)$, where parameter s is periodic, the λ loops satisfy one of the two equations:

$$\frac{dx_0}{ds} = \sqrt{\frac{\lambda_2(x_0) - \lambda^2}{\lambda_2(x_0) - \lambda_1(x_0)}} \xi_1(x_0) \pm \sqrt{\frac{\lambda^2 - \lambda_1(x_0)}{\lambda_2(x_0) - \lambda_1(x_0)}} \xi_2(x_0) \quad (4.1)$$

Here $0 < \lambda_1(x_0) \leq \lambda_2(x_0)$ and $\xi_i(x_0)\xi_j(x_0) = \delta_{ij}$ are eigenvalues and (normalized) eigenvectors, respectively, of the right Cauchy-Green strain tensor field, $C_{t_0}^t(x_0) := DF_{t_0}^t(x_0)^\top DF_{t_0}^t(x_0)$, a frame-invariant (or objective) measure of deformation where

$F_{t_0}^t(x_0)$ is the flow map that associates times t_0 and t positions of fluid particles, which evolve according to

$$\frac{dx}{dt} = v(x, t), \quad (4.2)$$

where $v(x, t)$ is a two-dimensional velocity field. Closed curves satisfying (4.1) occur in families of nonintersecting limit cycles, necessarily encircling singularities of $C_{t_0}^t(x_0)$, i.e., points where the field is isotropic. The outermost member of a family of λ -loops will be observed physically as the boundary of a coherent material eddy: immediately outside, no coherent belt may exist containing the eddy. Limit cycles of (4.1) tend to exist only for $\lambda \simeq 1$. Material loops characterized by $\lambda = 1$ reassume their initial arclength at time t . This property, along with conservation of enclosed area in the incompressible case, creates extraordinary coherence.

Coherent material eddy detection and tracking are implemented as follows.

1. Fix a domain U and a coherence time scale T over which eddies are to be located.
2. On U set a grid \mathcal{G}_U of initial positions x_0 .
3. For each $x_0 \in \mathcal{G}_U$ integrate (4.2) from t_0 to $t = t_0 + T$, obtaining a discrete approximation of flow map $F_{t_0}^t(x_0)$.
4. Evaluate $DF_{t_0}^t(x_0)$ using finite differences, then construct $C_{t_0}^t(x_0)$, and finally compute the corresponding eigenvalues $\{\lambda_i(x_0)\}$ and eigenvectors $\{\xi_i(x_0)\}$.
5. Locate eddy candidates regions V by isolating singularities of $C_{t_0}^t(x_0)$ surrounded by singularity-free annular regions.
6. In each V repeat the first two steps using a finer grid \mathcal{G}_V and seek the outermost possible limit cycles of (4.1) with the aid of a Poincaré section starting with $\lambda =$

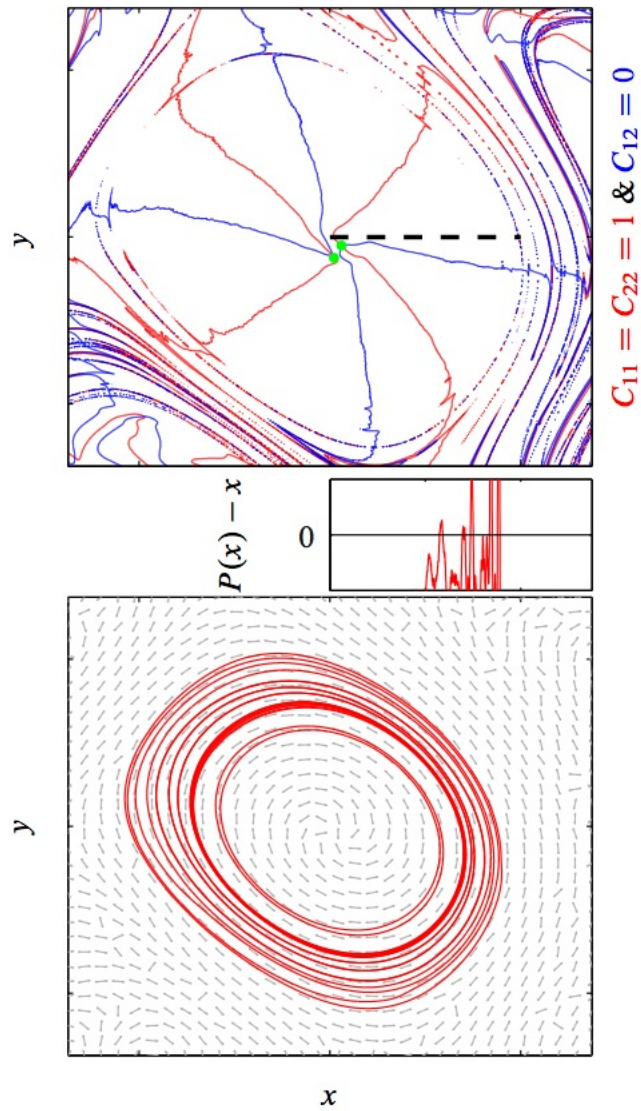


Figure 4.2: (top) A coherent Lagrangian eddy is an annular, singularity-free region which enclose a clutter of singularities (green dots), dotted line is selected the Poincaré section. (bottom) Limit cycles (red closed curves) of system (4.1) fill up the eddy region, and traverse the stationary points, where $P(x) = x$, of the Poincaré section.

1. If no limit cycle is found for any λ (near 1), the candidate region does not contain a coherent material eddy.

7. Finally, advect the boundary of the coherent material eddy detected to track its motion.

Figure 4.2 illustrates the case in which a coherent Lagrangian eddy exists.

We consider again the geostrophic velocity field derived from SSH field distributed by AVISO (Archiving, Validation, and Interpretation of Satellite Oceanographic data); specific products employed are Rio05 mean dynamic topography and DT-MSLA "all sat merged" SSH anomaly, respectively. The mean dynamic topography is constructed from satellite altimetry data, in situ measurements, and a geoid model [Rio and Hernandez, 2004]. The SSH anomaly is provided weekly on a 0.25° resolution longitude-latitude grid. This is referenced to a 20 year (1993–2012) mean, obtained from the combined processing of data collected by altimeters on the constellation of available satellites [Le Traon et al., 1998]. Here the weekly SSH fields are interpolated daily, which reduces trajectory overshooting [Keating et al., 2011]. We choose $U = [20.5^\circ\text{W}, 10.5^\circ\text{E}] \times [29.5^\circ\text{S}, 32.5^\circ\text{S}]$ (indicated by a box in Figure 4.3) as our detection domain. This domain intersects the so-called Agulhas corridor [Goni et al., 1997]. It lies sufficiently away from the Agulhas retroflection to allow coherence to build up and is sufficiently large to capture all eddies possibly shed and to fit the largest such eddies. We set coherence time scales $T = 90, 180$, and 360 days. This results in detection of eddies with maximum diameters decreasing from around 280 km to 100 km. Eddy diameters remain stable for T in the range 30 – 90 days; for T shorter than 30 days or longer than 360 days coherence is difficult to find. This may be qualitatively related to the fact that Lagrangian coherent structures are usually converged from a sufficiently long computa-

tional time interval $[t_0, t_0+T]$ [Haller and Beron-Vera, 2012]. Detections are carried out over 1992–2013 (nearly the entire period of available altimetry measurements) in such a way that U is filled with new eddies at each t_0 , thereby avoiding defective or redundant eddy counting. We set \mathcal{G}_U and \mathcal{G}_V to be regular with square elements of roughly 1.5 and 1 km sides, respectively. All integrations are carried out using a step-size-adapting fourth order Runge-Kutta method with interpolations obtained with a cubic scheme. In the case of (4.1), further care had to be taken by enforcing a unique eigenvector field orientation at each integration step.

4.4 Results

We begin by showing in Figure 4.3 trajectories (left column) and histograms of mean translational speeds and diameters (right column) of coherent material eddies detected from $T = 90$ (top row), 180 (middle row), and 360 (bottom row) day integrations. A total of 59 (4), 47 (1), and 23 (0) anticyclonic (cyclonic) eddies are detected over 1992–2013. Ignored from our records are only 7 (6), 3 (3), and 1 (0) anticyclones (cyclones) that take southwestward directions and dissipate fast as these eddies are not relevant for our purpose. The predominance of anticyclones over cyclones signals enhanced stability for anticyclones consistent with prior results [van Sebille et al., 2010]. Among these eddies, 39, 40, and 19 are found with stretching factor $\lambda = 1$; for all other eddies, λ ranges from 0.9 to 1.1. It should be realised that 180 and 360 day eddies reside inside 90 day eddies at detection time. i.e., 180 and 360 day eddies do not constitute different eddies but rather constitute 90 day eddy coherent material cores. In effect, an eddy boundary detected with a given T typically lies quite close to some member of the family of λ loops that fill an eddy detected with a shorter T . The detection rate is quite irregular, varying from one to four eddies per year. This applies to 90 and

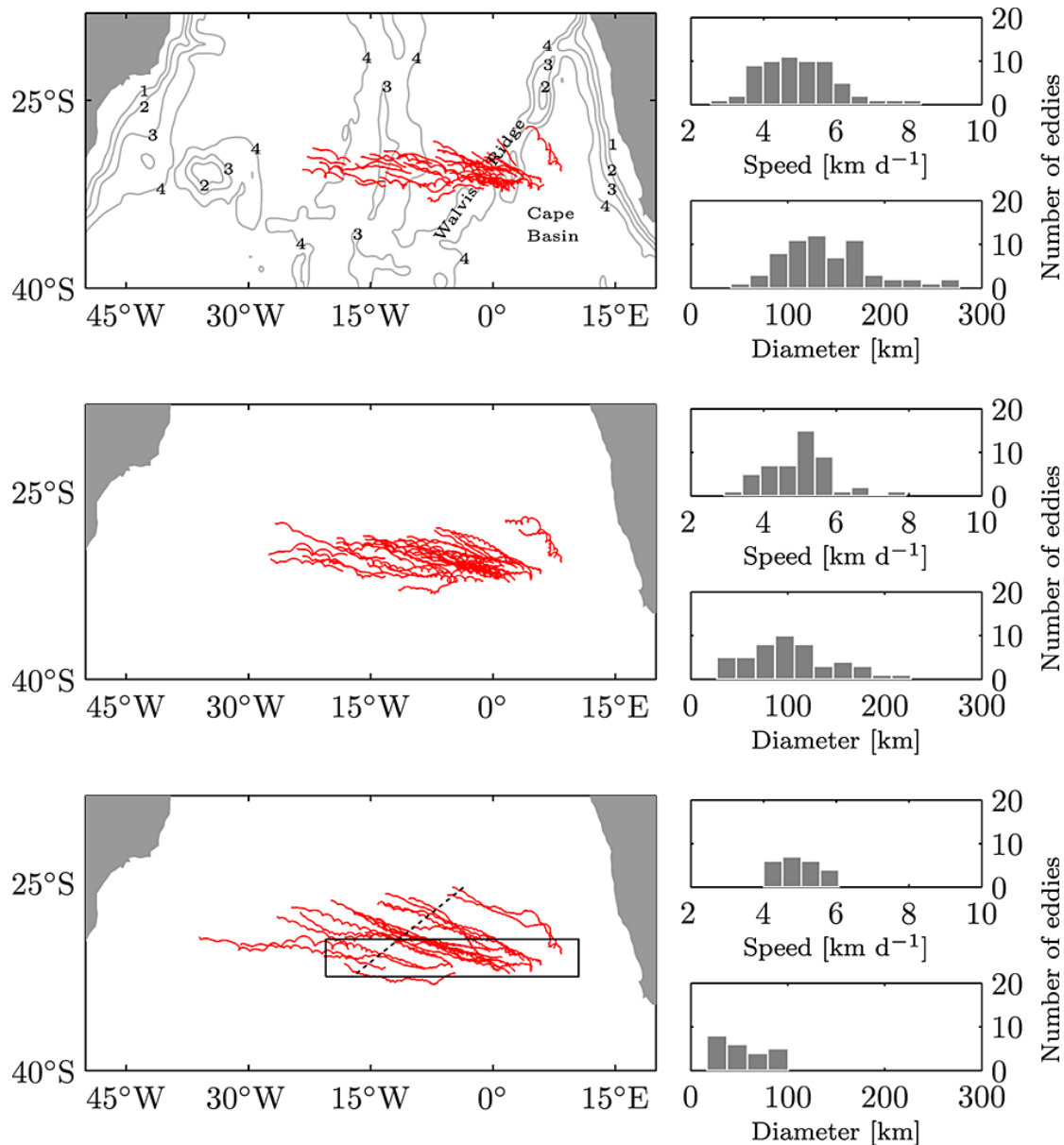


Figure 4.3: (left column) Trajectories and (right column) mean translation speeds and diameters of coherent material eddies in the Agulhas corridor as detected from altimetry-derived velocities over 1992–2013 with lifetimes (top row) 90, (middle row) 180, and (bottom row) 360 days. (bottom left) Detection domain (solid rectangle) and the reference section used in the construction of the coherent transport time series of Figure 4.6 (dashed line). Selected bathymetry levels (in km) are indicated in the top left along with two relevant topographic features. From Wang et al. [2015b].

180 day eddies; it applies to 360 day eddies too when they are present, namely, all years except 1994–1995, 2004, and 2006-2007. The irregularity of the detection rate is indicative of substantial coherent material eddy episodicity rather than artifact created by the altimetry set. Indeed, while earlier years are covered by fewer satellite altimeters than later years, gaps with no eddy detected are present in both earlier and later years. An obvious observation from inspection of the figure is that trajectory lengths increase with T increasing from 90 to 180 to 360 days. In particular, these increase on average from 450 to 900 to 1800 km. This is accompanied by a reduction in eddy size. In effect, mean eddy diameters decrease on average roughly from 140 to 100 to 50 km. This suggests an average eddy decay rate of $40 \text{ km}^2 \text{ d}^{-1}$ in 360 days. Mean eddy translational speeds remain quite stable around 5 km d^{-1} (about twice the speed of long baroclinic Rossby waves) independent of T .

We next proceed to discussing transport estimates. Let Σ be a reference curve and assume that it is traversed by coherent material eddies, episodically and all in the same direction. We define *coherent transport* the contribution by such eddies to the flux across Σ of the two-dimensional velocity supporting the eddies. For a simple, analytical eddy, for instance, the one detected from system (2.1) in chapter 2, the eddy flux at each time step is calculated by integrating the instantaneous velocity inside this eddy along the reference curve Σ (dashed line in top panel Figure 4.4), which yields a time series that approximates a parabola (red solid curve in bottom panel Figure 4.4) for the time interval over which the eddy crosses Σ . Such a parabola-shaped function is then the coherent transport in this case. For an eddy in complex unsteady flows, we approximate this function by a boxcar with amplitude equal to the area of the eddy divided by the length of the time interval over which it crosses Σ . For multiple eddies, a coherent transport time series will be given by a sequence of boxcars with different

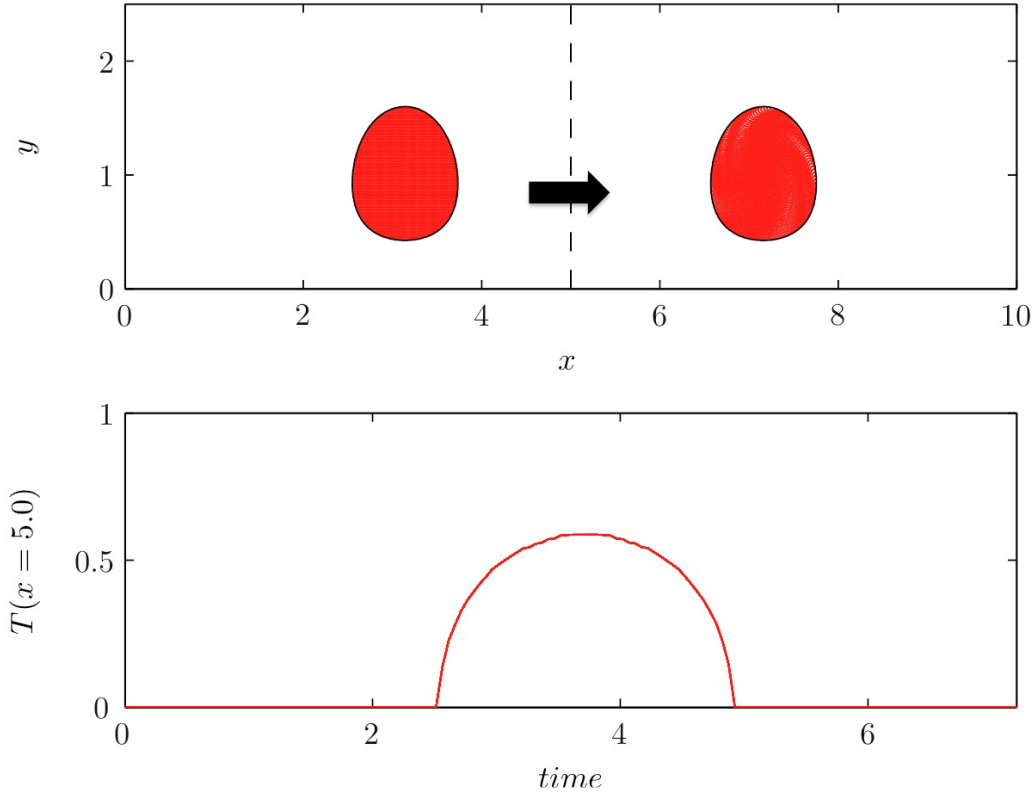


Figure 4.4: (top) Initial and final positions of an idealized coherent Lagrangian eddy. (bottom) Instantaneous, two-dimensional flux T (red curve) caused by eddy penetration through the dashed line ($\Sigma : x = 5.0$) in top panel over time.

amplitudes resulting from superimposing episodic individual eddy contributions. We estimate transport of 360 day eddies only, as they are most capable of coherently carrying water across the South Atlantic. Eddies that can only be detected with shorter T lose coherence more easily. For an eddy containing both a 360 day material eddy core and an outer boundary from a shorter T day integration, the fluid sandwiched between the core and outer boundary tends to disperse fast beyond T , while the eddy core may still stay compact even after 360 days (Figure 4.5).

Figure 4.6 (top) shows a time series of coherent transport estimates over the period 1992–2013 obtained by considering 360 day eddies and Σ as indicated by the dashed

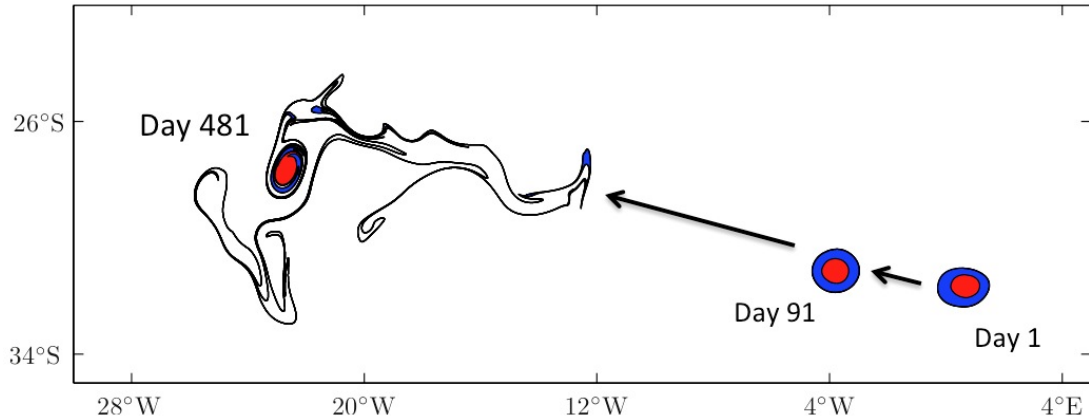


Figure 4.5: A material eddy detected from $T = 90$ day integration contains an inner 360 day eddy core (red). Fluid (blue) trapped between the outermost 90 day boundary and inner 360 day boundary stays compact for at least 90 days. Over extended time period, however, this part of fluid disperse quickly. While the 360 day eddy core still stays compact, even beyond its integrating time length.

segment in Figure 4.3 (bottom left), which is traversed by all identified 360 day eddies (and their residuals, after coherence is lost) in one direction. While transport defined above is two-dimensional in nature, we report three-dimensional transport values measured in Sverdrup (Sv) ($1 \text{ Sv} = 10^6 \text{ m}^3 \text{ s}^{-1}$). These are obtained by multiplying the computed two-dimensional transport values by 1 km. With a certain degree of uncertainty [de Steur et al., 2004], this value is in the range of mature Agulhas ring trapping depths inferred from float-profiling hydrography [Souza et al., 2011a]. A distinguishing feature of the computed transport time series is a large variability, both intra- and interannual. Nonzero transport estimates range approximately from 0.25 to 3 Sv (about 1.5 Sv on average). These varying transport estimates are attributed mainly to varying eddy sizes. Interspersed zero transport gaps last roughly from 3 months to 3 years. These varying length gaps cannot be explained by previously reported Agulhas ring shedding rates of one ring every 2 to 3 months [Byrne et al., 1995; Goni et al., 1997; Schouten et al., 2000]. Rather, they are due to marked eddy episodicity. Gray-shaded bar portions in

Figure 4.6 (top) correspond to transport of water that can be identified with leaking Indian Ocean water into the South Atlantic. The Indian Ocean water fraction carried within eddies is estimated by advecting the eddy boundaries backward in time for as long as at least 90% reversibility is attained (about 1.25 year on average) and computing the proportion of the enclosed fluid found east of 20°E, the longitude at which Indian Ocean and South Atlantic meet [Richardson, 2007]. We note that reversibility is strongly restricted by sensitive dependence on initial conditions. Also, the Agulhas retroflection typically extends west of 20°E [Dencausse et al., 2010]. Therefore, our estimates of Indian Ocean water content should be considered as a lower bound. At least, then, the eddies are found this way to carry on average about 30% of contents that can be unambiguously identified with Indian Ocean water. Accordingly, the transport of Indian Ocean water trapped inside the eddies is found to be approximately 0.5 Sv on average. Rare cases are eddies detected in mid-2002 and early 1996, which carry barely 1 and almost 99% of Indian Ocean water, respectively. The Indian Ocean water transported by these eddies is about 0.01 and 1 Sv, respectively.

Figure 4.6 (bottom) shows a time series of annual coherent transport estimates computed by averaging the (instantaneous) estimates in Figure 4.6 (top) within each year (as in that panel, gray-shaded bar portions correspond to Indian Ocean water transport). The maximum annual transport produced by 360 day coherent material eddies is about 0.3 Sv. Our estimate is 2 orders of magnitude smaller than earlier estimates obtained as total volume of eddies detected during a given year, divided by 1 year [Garzoli et al., 1999; Richardson, 2007; Dencausse et al., 2011; Souza et al., 2011a]. This large difference might be reduced by an order of magnitude if a larger vertical extent for the eddies is assumed. Indeed, van Aken et al. [2003] report vertical extents of 4 km but only for very young Agulhas rings. A reason for this large discrepancy is that our focus

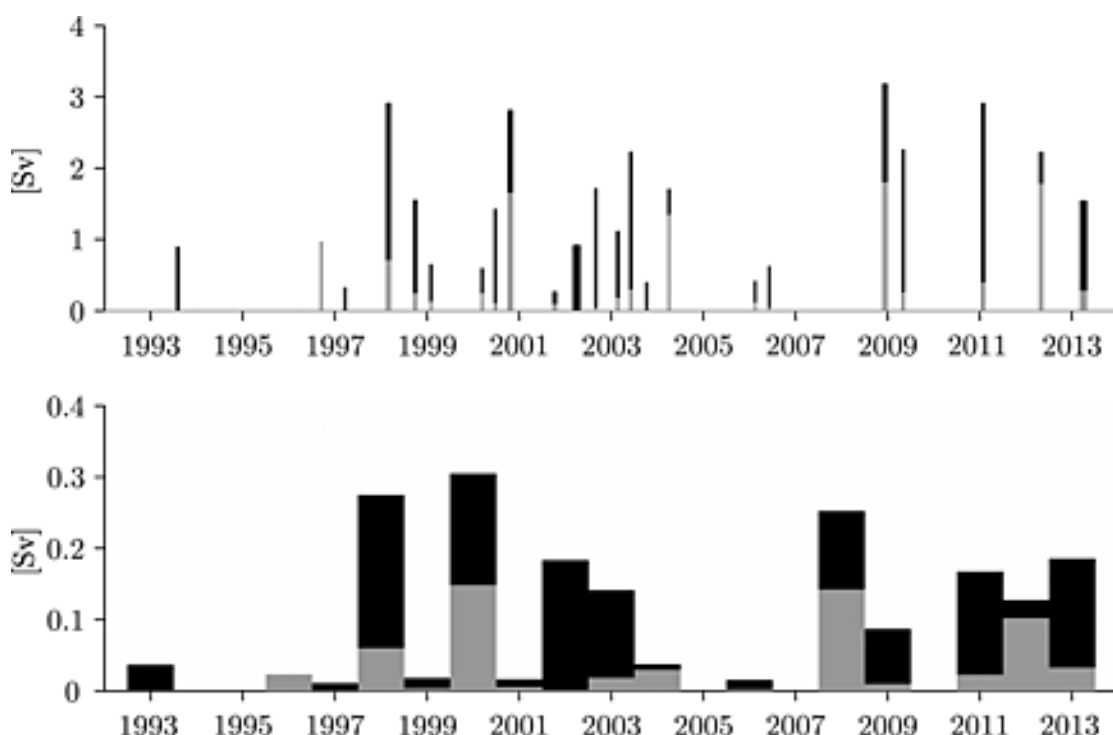


Figure 4.6: (top) Instantaneous and (bottom) annual average time series of transport produced by 360-day coherent material eddies crossing the reference section indicated by the dashed segment in the bottom left of Figure 4.3. Gray-shaded bar portions correspond to transport of Indian Ocean water trapped inside the eddies. From Wang et al. [2015b].

is on the rings that are most capable of traversing the South Atlantic basin, the average diameter and number of which are inherently smaller than young and short-lived rings. Moreover, earlier estimates implicitly assume that eddy signatures whose diameters at detection time are 250 km or so can reflect material fluid evolution to some extent. This cannot be guaranteed by Eulerian analysis of altimetry or the inspection of in situ and profiling-float hydrography, and drifter and float trajectories, which led to the earlier transport estimates. Truly material eddies as large as 250 km in diameter revealed from altimetry in the region of interest are very rare. Most such eddy signatures do not transport fluid and tend to disperse rather quickly [Beron-Vera, Wang et al., 2013]. The maximum annual transport of Indian Ocean water trapped inside 360 day coherent material eddies does not exceed 0.2 Sv. This is also smaller, by 2 orders of magnitude, than the annual Agulhas leakage estimates obtained from numerical simulations [Doglioli et al., 2006; Biastoch et al., 2009; Le Bars et al., 2014]. While these Agulhas leakage estimates still lack observational support, the noted large mismatch suggests that cross-basin trapping by rings is not a major mechanism through which Agulhas leakage enters the AMOC.

Finally, we turn to discussing aspects of the evolution of detected coherent material eddies. As before we focus on 360 day eddies, the most persistent of all eddies detected. Figure 4.7 shows snapshots of the long-term evolution of two eddies selected according to their behavior during their early and late evolution stages. The eddy in Figure 4.7 (left column) illustrates typical behavior, while the eddy in Figure 4.7 (right column) illustrates exceptional behavior. The evolutions are constructed by advecting passive tracers inside each eddy boundary (indicated in black) at detection time in backward time for as long as at least 90% reversibility is attained and also in forward time beyond the theoretical coherence time lengths. The typical behavior is characterized

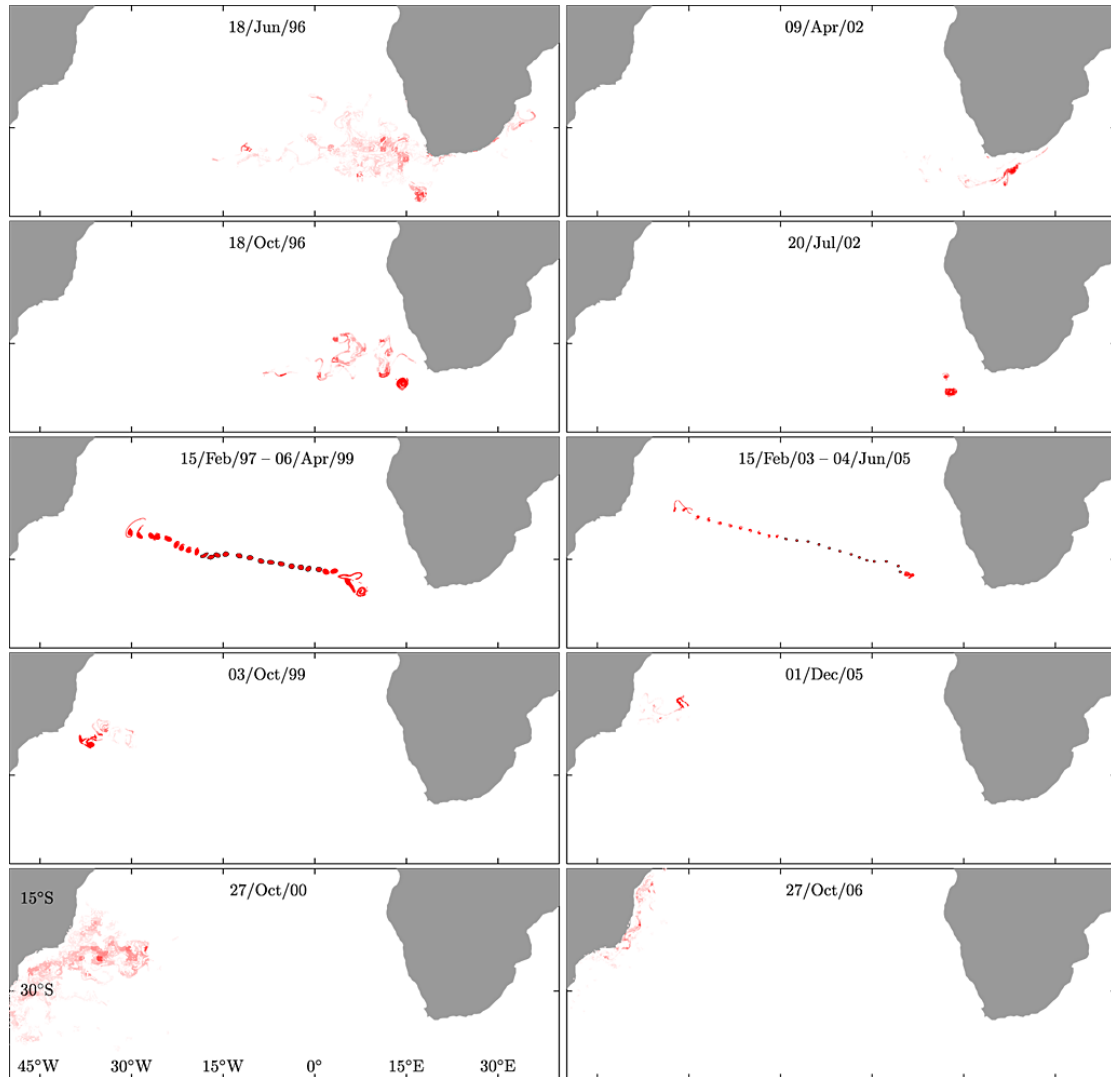


Figure 4.7: Snapshots of the long-term evolution of two 360-day coherent material eddies with (left column) typical and (right column) exceptional genesis and demise stages. The boundaries of the eddies while they constitute coherent material eddies are indicated in black. Indicated in red are passive tracers that completely fill these eddies during their coherent material stage. From Wang et al. [2015b].

by organization into small coherent material eddies (the specific eddy depicted in left column of Figure 4.7 is approximately 90 km in diameter) from rather incoherent fluid composed of a mixture mainly of water that resides in the South Atlantic and a much smaller fraction of water traceable into the Indian Ocean. Typical coherent material eddies emerge away from the Southern tip of Africa, just east of the Walvis Ridge in the South Atlantic. This genesis picture does not adhere to the commonly accepted conceptual picture in which Agulhas rings are shed from the Agulhas retroflection as a result of eventual Indian-Ocean-entrapping occlusions [Pichevin et al., 1999]. Our results are more consistent with those from earlier works [Schouten et al., 2000; Boebel et al., 2003] reporting intense mixing in the Cape Basin. But coherence eventually emerges from the mostly incoherent water resulting from this process close to the Walvis Ridge and is followed by propagation of small eddy cores with minor filamentation across the subtropical gyre. Coherence is eventually lost, the contents of the eddies are mixed with the ambient water in the vicinity of the bifurcation of the subtropical gyre, and finally transported mostly southward by the Brazil Current. Out of a total of 23 eddies detected, 15 adhere to this picture. The exceptional behavior, observed by only one eddy, is also characterized by emergence of small coherent material eddies (the particular eddy shown in right column of Figure 4.7 has roughly 40 km in diameter) out of rather incoherent water, the only difference being that most of the water inside this eddy is traceable into the Indian Ocean. This is still different from the widely accepted ring genesis picture inasmuch as material coherence is not acquired immediately but rather after some time, near the Walvis Ridge. Propagation across the subtropical gyre then follows with minor filamentation until coherence starts to be gradually lost. The eddy contents mix with the surrounding water near the bifurcation of the subtropical gyre. The majority of these is then transported northward close to the coast by North Brazil

Current. This behavior most closely adheres to the scenario put forward by Gordon and Haxby [1990] (Figure 4.1). The behavior of the remaining seven eddies detected shares aspects of the two markedly distinct behaviors just described.

4.5 Concluding remarks

Aided by a recently developed Lagrangian technique from nonlinear dynamical systems theory, we have extracted from geostrophic velocities derived from nearly two decades of altimetry measurements a coherent transport signal across the South Atlantic through the so-called Agulhas corridor. The technique enables accurate, frame-independent identification of mesoscale eddies with cores whose material boundaries remain coherent, i.e., without showing noticeable signs of filamentation, for up to 1 year. These coherent material eddies were used in the coherent transport computation, which turned out to be smaller (by at least 2 orders of magnitude) than earlier ring transport estimates. The main reason is that those transport estimates implicitly assumed material coherence for eddies revealed from their Eulerian footsteps in the altimetry data set. Such eddies are either too large (by 1 order of magnitude) for long-range material coherence to be guaranteed or simply do not represent coherent material eddies. The portion of Indian Ocean water annually carried within the coherent material eddies was also identified and found to be small (by 2 orders of magnitude) compared to recent estimates of total Agulhas leakage based on numerical simulations. This result suggests a reduced role of Agulhas rings in transporting leaked Indian Ocean water. We also investigated the evolution of the detected coherent material eddies. We found that the conceptual picture in which Agulhas rings are shed from the Agulhas retroflection as a result of episodic Indian-Ocean-water-trapping occlusions is, in general, not valid. Coherent material eddies tend to emerge near the Walvis Ridge from rather incoherent water, mostly resid-

ing in the South Atlantic and to a small extent traceable into the Indian Ocean. How this precisely happens is not known and is subject of ongoing investigation. The majority of the coherent material eddies formed this way (15 out of a total of 23) was found to cross the subtropical gyre and eventually to be absorbed into the Brazil Current. However, only one eddy consisting of mainly Indian Ocean water was seen to pour its contents on the North Brazil Current. This suggests that the contribution by coherent material Agulhas rings through advective trapping across the South Atlantic to the global thermodynamical budget is much less significant than originally thought [Gordon and Haxby, 1990]. While we find ability of eddies to transport water over long distances, this is less important than recently argued for eddies beyond Agulhas rings based on lax assumptions about material coherence [Dong et al., 2014; Zhang et al., 2014]. Finally, explicit resolution of three-dimensional aspects of ring transport, which can be done by applying extensions of the technique employed here [Blazevski and Haller, 2014; Haller, 2014] to an ocean general circulation model, is not expected to substantively modify our results. Indeed, these may be actually more constrained by diffusion induced by submesoscale turbulence unresolved by altimetry and most models.

Chapter 5

Life cycle of a material Agulhas Current ring

5.1 Overview

At the time of writing, results from additional research are being prepared for publication [Wang et al., 2015a]. This publication in preparation, whose main findings so far are reported here, is aimed at providing a detailed characterization of the life cycle of a long-lived Agulhas ring. These findings concern the evolution of the ring as a quite coherent material entity for a period of about 2 years after the initial coherence is lost upon crossing the Walvis Ridge. We attribute this to the continual development of short-term coherent material boundaries around the ring. These boundaries provide continual short-term shields for the ring, which prevent its interior from being mixed with the ambient turbulent flow. We show that such coherence regaining cannot be inferred from Eulerian analysis. These findings complement the study on the ability of Agulhas rings in transporting fluid across the South Atlantic.

5.2 Background

The ability of Agulhas rings detected from satellite altimetry measurements of sea surface height (SSH) to maintain long-term Lagrangian (i.e., material) coherence has been

subject of recent investigation using nonlinear dynamical systems techniques that enable objective (i.e., observer-independent) framing of Lagrangian coherence. Lehahn et al. [2011] demonstrated the significance of such rings using satellite ocean color imagery, which provides an assessment of Lagrangian coherence independent of the analysis of satellite altimetry. Using the over two-decade-long altimetry record, Wang et al. [2015b] found that long-lived (of up to at least 1 year of duration) rings have small (about 50-km in diameter) coherent Lagrangian cores, suggesting a fast decay for the rings. On the other hand, they found that such cores carry a small (about 30%) fraction of water traceable into the Indian Ocean. The two findings together question the long-range ability of rings in transporting Agulhas leakage that Eulerian analysis of SSH appear to suggest [Zhang et al., 2014]. In turn, Froyland et al. [2015], through the application of a probabilistic method on satellite altimetry data, found that the rings decay slowly, enabling long-range Agulhas leakage transport.

The goal of the present paper is to bridge the gap between the latter two contradicting results by carrying out a detailed objective investigation of the evolution of the ring studied by Froyland et al. [2015]. This is done using geodesic eddy detection method [Haller and Beron-Vera, 2013, 2014], which enables optimal detection of rings with Lagrangian boundaries that exhibit no signs of filamentation over the coherence assessment time interval.

Initial coherence of the ring is abruptly disrupted upon traversing the Walvis Ridge, which is qualitatively in line with the SSH anomaly response. Beyond the Walvis Ridge a large fraction of the ring (about 300 km^3 , corresponding to an at least 2-km-deep ring of 150-km of diameter) is observed to stay as a compact Lagrangian entity far beyond the theoretical Lagrangian coherence horizon. This is shown to be caused by successive short-term coherence regain events. Demise of the ring eventually occurs after a rapid

decay of the area enclosed by coherent Lagrangian loops that provide the fluid in their interior successive short-term shielding from turbulent mixing with the ambient fluid. Not all aspects of the life cycle of the ring are inferable from Eulerian analysis of SSH anomaly, which signals coherence gain upon crossing the Walvis Ridge and slow decay thereafter. It is noted finally that even if this behavior generalizes to all Agulhas rings, which needs to be verified, their long-range transport ability is still limited.

5.3 Methodology

We are concerned with fluid regions enclosed by exceptional material loops that defy the exponential stretching that a typical loop will experience in turbulent flow. As Haller and Beron-Vera [2013, 2014] have shown, such loops have small annular neighborhoods exhibiting no leading-order variation in averaged material stretching.

More specifically, solving the above variational problem reveals that the loops in question are uniformly stretching: any of their subsets are stretched by the same factor λ under advection by the flow from time t_0 to time t . The time t_0 positions of λ -stretching material loops turn out to be limit cycles of one of the following two equations for parametric curves $s \mapsto x_0(s)$:

$$\frac{dx_0}{ds} = \sqrt{\frac{\lambda_2(x_0) - \lambda^2}{\lambda_2(x_0) - \lambda_1(x_0)}} \xi_1(x_0) \pm \sqrt{\frac{\lambda^2 - \lambda_1(x_0)}{\lambda_2(x_0) - \lambda_1(x_0)}} \xi_2(x_0). \quad (5.1)$$

Here $\lambda_1(x_0) < \lambda^2 < \lambda_2(x_0)$, where $\{\lambda_i(x_0)\}$ and $\{\xi_i(x_0)\}$, satisfying

$$0 < \lambda_1(x_0) \equiv \frac{1}{\lambda_2(x_0)} < 1, \quad \xi_i(x_0) \cdot \xi_j(x_0) = \delta_{ij} \quad i, j = 1, 2, \quad (5.2)$$

are eigenvalues and (normalized) eigenvectors, respectively, of the Cauchy–Green tensor,

$$C_{t_0}^t(x_0) := DF_{t_0}^t(x_0)^\top DF_{t_0}^t(x_0), \quad (5.3)$$

an objective (i.e., independent of the observer) measure of material deformation, where $F_{t_0}^t : x_0 \mapsto x(t; x_0, t_0)$ is the flow map that takes time t_0 positions to time t positions of fluid particles, which obey

$$\frac{dx}{dt} = v(x, t), \quad (5.4)$$

where $v(x, t)$ is a two-dimensional velocity field assumed divergence free.

Limit cycles of (5.1) either grow or shrink under changes in λ , forming smooth annular regions of nonintersecting loops. The outermost member of such a band of material loops is observed physically as the boundary of a *coherent Lagrangian eddy*. Limit cycles of (5.1) tend to exist only for $\lambda \approx 1$. Material loops characterized by $\lambda = 1$ resist the universally observed material stretching in turbulence: they reassume their initial arclength at time t . This conservation of arclength, along with enclosed area preservation (which holds by assumption), produces extraordinary coherence [Beron-Vera et al., 2013]. Finally, limit cycles of (5.1) are (null) geodesics of the generalized Green–Lagrange tensor $C_{t_0}^t(x_0) - \lambda^2$, which must necessarily contain degenerate points of $C_{t_0}^t(x_0)$ where its eigenvector field is isotropic. For this reason the above procedure is known as *geodesic eddy detection*.

The specific form of the velocity field considered here is given by

$$v(x, t) = \frac{g}{f} \nabla^\perp \eta(x, t), \quad (5.5)$$

where g is the acceleration of gravity, f stands for Coriolis parameter, and $\eta(x, t)$ is the SSH, taken as the sum of a (steady) mean dynamic topography and the (transient) altimetric SSH anomaly. The mean dynamic topography is constructed from satellite altimetry data, in-situ measurements, and a geoid model [Rio and Hernandez, 2004]. The SSH anomaly is provided weekly on a 0.25° -resolution longitude–latitude grid. This is referenced to a 20-year (1993–2012) mean, obtained from the combined processing of

data collected by altimeters on the constellation of available satellites [Le Traon et al., 1998].

For the purpose of the present investigation we have chosen to focus on the ring detected and tracked by Froyland et al. [2015] over the period 1999–2001. This ring was considered by Wang et al. [2015b] in their coherent transport calculations. The numerical implementation of geodesic eddy detection is documented at length [Haller and Beron-Vera, 2013, 2014; Beron-Vera et al., 2015; Wang et al., 2015b; Karrasch et al., 2014] and a software tool is now available [Onu et al., 2015]. Reproducibility of the results only requires one to know that the width of the computational grid was set to 0.5 km. This enabled us to push the Lagrangian coherence detectability horizon close to 1.5 years.

5.4 Preliminary results

Instead of extracting the boundary of a coherent Lagrangian eddy, the coherent set approach [Froyland and Padberg-Gehle, 2014] isolates a series of regions in time such that fluid particles initialized in one region are most probable to fall inside its neighboring one in a non-dispersive fashion under the flow map. Using such an approach, Froyland et al. [2015] detected an Auglhas ring able to travel across the South Atlantic subtropical gyre for over 2 years from satellite altimetry data. The monthly positions of coherent sets associated with this ring are shown in Figure 5.1. The coherent sets are not truly material patches in that the areas of these sets are not conserved over time under the geostrophic assumption. Nonetheless, fluid particles flowing from the initial coherent set into successive ones are well retained, given that only a total of 15% to 20% of these particles are found to reside out of the final coherent set after more than 2 years [Froyland et al., 2015].

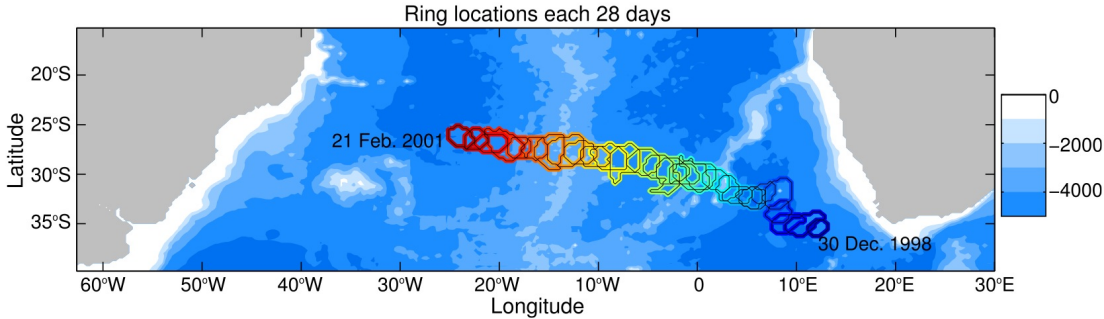


Figure 5.1: Monthly positions of an Agulhas ring over more than 2 years. Colored contours denotes the boundaries of coherent sets, going from green to red as time progresses. Blue shading indicates the bathymetric features. From Froyland et al. [2015].

An observation from the inspection of the monthly positions of coherent sets (Figure 5.1) is that the size of the ring only changes slightly over the whole ring lifetime, which appears to contradict the results of Wang et al. [2015b], who find that long-lived material rings decay at a rate of around $40 \text{ km}^2 \text{d}^{-1}$ in horizontal area over the first year of detection.

With the purpose of resolving these seemingly contradicting results, we begin by applying geodesic eddy detection on $t_0 = 31 \text{ March } 1999$, date by which the ring in question is in a sufficiently mature Lagrangian coherence stage. On that date the ring is found inside the region indicated by the square in the left panel of Figure 5.2a. Geodesic eddy detection was carried over t_0 through $t = t_0 + T$ for T increasing from 30 d in steps of 30 d out to 480 d, the longest T from which it was possible to extract a coherent Lagrangian eddy boundary. This is a very long Lagrangian coherence time scale, consistent with the statement above that the ring is in a mature Lagrangian coherence stage. Application of geodesic eddy detection resulted in a nested family of Lagrangian boundaries with coherence time scale increasing inward (for each T considered there is a nested family of λ -loops; the boundary shown is the outermost one in each family). These boundaries are indicated in red on the detection date in Figure 5.2a (the

right panel is a blowup of the region indicated by the rectangle in the left panel). The outer, shorter-lived boundaries provide a shield to the inner, longer-lived boundaries surrounding the core of the coherent Lagrangian ring. This is evident in the successive advected images of the boundaries under the flow. These are shown in Figs. 5.2b–f on selected dates over more than 2 years of evolution. An advected boundary is depicted red when it is within its theoretical Lagrangian coherence horizon and in a blue tone when is beyond it. As predicted, no signs of filamentation are observed up to that time scale (i.e., boundaries do not shed any filament when they are depicted red). The filamentation observed beyond the theoretical Lagrangian coherence time scale reveals that the evolution of the ring is characterized by a clear decay process.

The large gap separating the boundaries occurs as Lagrangian coherence time scales are set to $T = 270$ and 300 d on 31 March 1999 (cf. Figure 5.2a, right panel). Such a gap indicates an abrupt loss of Lagrangian coherence. Inspection of Figure 5.2g allows one to identify in space where this abrupt Lagrangian coherence loss takes place. This plot shows the area enclosed by the largest boundary that are theoretically coherent evolving from t_0 as a function of geographical longitude. Note that the area drops abruptly right after the ring traverses the Walvis Ridge. This is a sign of destabilization, in this case likely resulting from interaction of the ring with the bottom topography. A large vertical extent for the ring is therefore suggested given that this ring must feel the Walvis ridge, the characteristic depth of which is over 2 km [Byrne et al., 1995] within the Agulhas ring corridor [Goni et al., 1997]. Such a large vertical extent is in line with in-situ observations [van Aken et al., 2003] and qualitatively consistent with the SSH anomaly evolution of this ring upon encountering the ridge. Note that the amplitude of SSH anomaly (Figure 5.3b), after decaying at a rate of roughly 5 cm per month from 31 March 1999, increases upon crossing the Walvis Ridge, recovering nearly 85% of

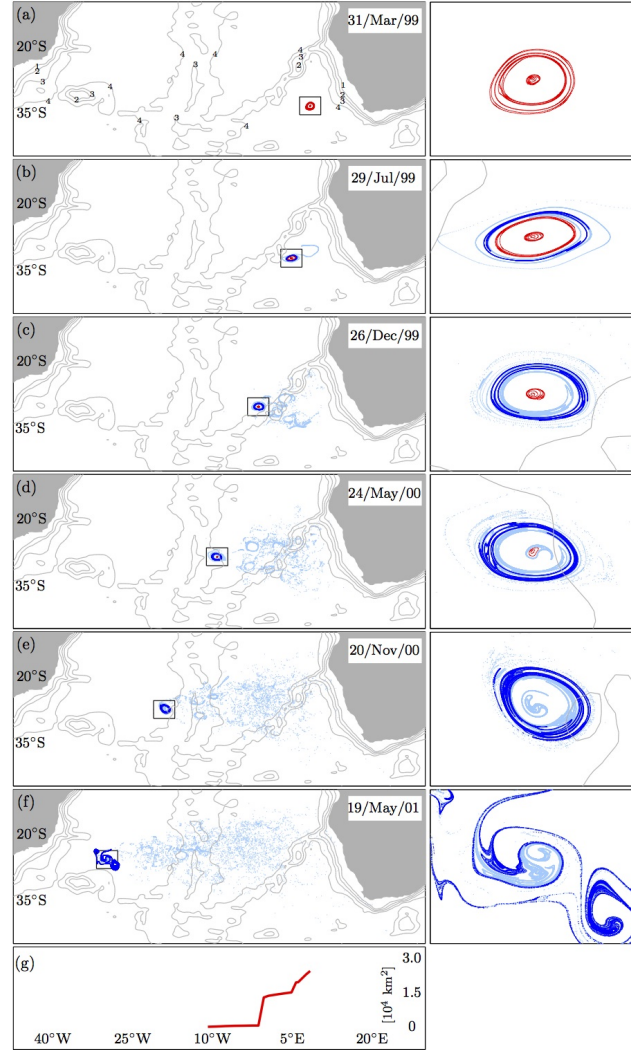


Figure 5.2: (a) Nested family of coherent Lagrangian eddy boundaries extracted from altimetry-derived velocity by applying geodesic eddy detection on $t_0 = 31$ March 1999 inside the region indicated by a rectangle. Each member of the family has a different Lagrangian coherence time scale T ranging from 30 d (outermost) to 40 d (innermost) in steps of 30 d. Selected isobaths (in km) are indicated in gray. The outset is a blowup of the indicated region. (b–f) Adverted images under the flow (i.e., evolution) of the coherent Lagrangian eddy boundaries in (a) on selected dates. An advected boundary is depicted red when it is within its theoretical Lagrangian coherence horizon and in a blue tone when is beyond it. (g) As a function of longitude, area of the largest domain enclosed by advected boundaries within their theoretical Lagrangian coherence horizon. From Wang et al. [2015a].

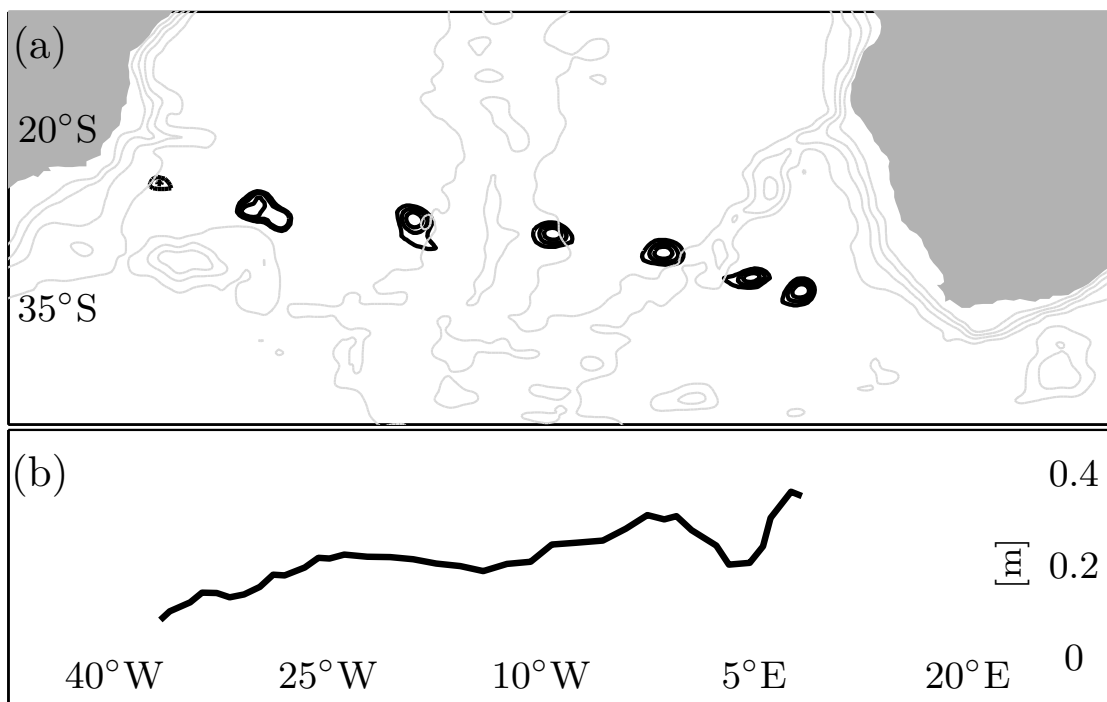


Figure 5.3: (a) Streamlines of the altimetric sea surface height (SSH) field in each rectangular region indicated in Figure 5.2a–f plus the streamline snapshot when no short-term coherence is detectable any more. (b) As a function of longitude, maximum SSH anomaly in each such region. From Wang et al. [2015a].

its amplitude on 26 December 1999, to about 35 cm. Schouten et al. [2000] speculated that such a behavior is a reflection of ring being able to contact with the Walvis Ridge directly. This speculation is supported by de Steur and van Leeuwen [2009], who used numerical experiments to find that a ring transfers its kinetic energy from lower to upper layer upon traversing a meridional ridge, which tends to intensify the SSH amplitude through geostrophy.

Beyond the Walvis Ridge, the amplitude of the SSH anomaly falls at a rate of about 1 cm per month, suggesting decay of the ring, albeit slow (Figure 5.3b). While filamentation of the ring is observed starting 30 d after detection on 31 March 1999, and abrupt Lagrangian coherence loss happens about 10 months after that date, a large fraction of the ring’s fluid preserves a strikingly compact entity over almost 2 years of evolution.

This is manifested by the tendency of the second-to-outermost Lagrangian eddy boundary (depicted in dark blue in Figure 5.2b–f) to develop mainly tangential filamentation beyond its theoretical coherence horizon (60 d) and for nearly 2 years. This boundary encloses nearly 95% of the total area of the ring detected on 31 March 1999. We explain the enduring Lagrangian coherence of the ring as a consequence of successive short-time Lagrangian coherence regain events.

To illustrate this, in Figure 5.4a we show (in blue) selected advected positions of the 60-d coherent Lagrangian ring boundary detected on 31 March 1999 (second-to-outermost boundary in Figure 5.2a). Overlaid on each we depict (in red) a 30-d coherent Lagrangian ring boundary identified on the date that advected 60-d boundary is shown. For nearly 2 years the advected 60-d boundary is instantaneously very closely shadowed by a 30-d boundary, which provides an effective short-term shield to mixing of the fluid inside the advected 60-d boundary with the ambient fluid stirred by turbulence. Beyond approximately 2 years filamentation of the advected 60-d boundary ceases to be tangential, signaling more intense mixing with the ambient fluid. Consistent with this the 30-d boundaries start to shrink, loosing their shielding power, until no 30-d boundary can be detected. This happens on 18 February 2001. Beyond this date only 15-d boundaries can be extracted. Eventually by 1 September 2001 no short-term boundary is possible to be identified, the ring detected on 31 March 1999 loses Lagrangian entity completely, and can be declared dead prior to reaching the South American coast.

Plotting the area of the short-term shielding boundaries as a function of longitude (Figure 5.4b) helps visualize the two stages that typify the Lagrangian evolution of the Agulhas ring under investigation. This is characterized by a stage of extended period of sustained coherence revealed by a nearly constant area enclosed by the short-term shielding boundaries, ranging from 31 March 1999 to 18 February 2001, about 2 years.

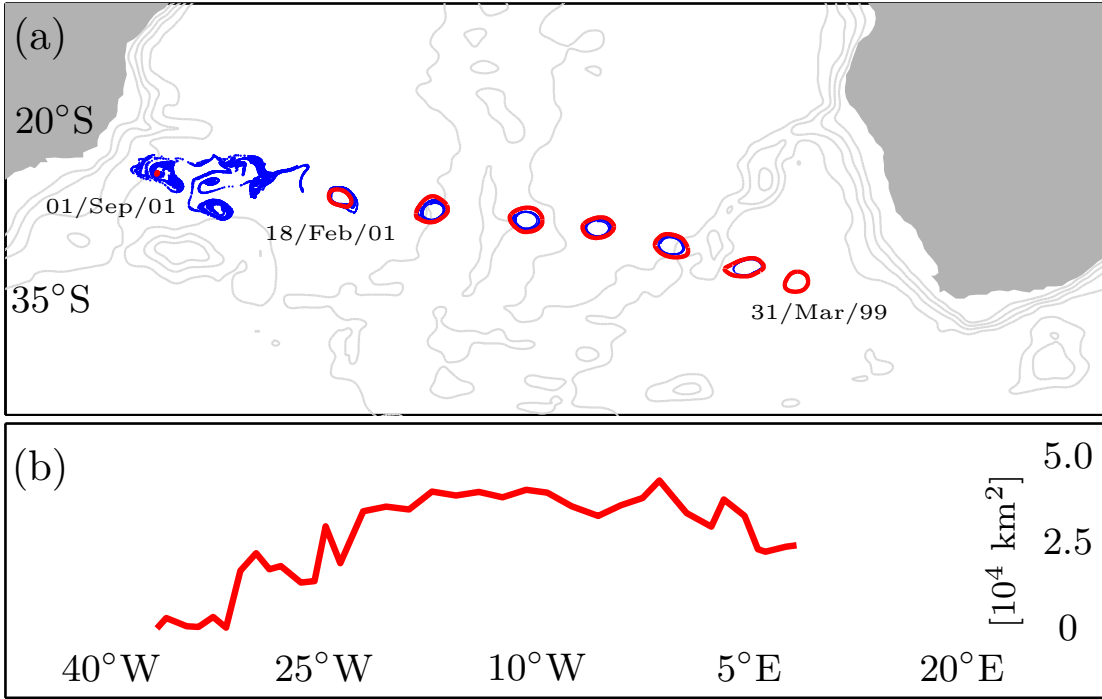


Figure 5.4: (a) In blue, selected advected positions of the second-to-outermost material loop in fig:evola, corresponding to the Lagrangian ring boundary with coherence time scale $T = 60$ d detected on 31 March 1999. In red, short-time boundaries detected on the dates the advected loop positions are shown. From 31 March 1999 to 18 February 2001, $T = 30$ d, and from 18 February 2001 to 1 September 2001, $T = 15$ d. (b) Area enclosed by the short-time boundaries as a function of longitude. From Wang et al. [2015a].

This stage is followed by fast coherence decay revealed by a rapid drop in the area enclosed by the shielding boundaries, from 18 February 2001 to 1 September 2001, just a bit over 6 months.

Certain behavior of the Lagrangian ring is qualitatively reflected in the SSH field. The SSH anomaly exhibits a clear oscillation in amplitude when the ring traverses the Walvis Ridge and experiences sudden loss of coherence. Nevertheless, the slow decay of SSH anomaly beyond the ridge masks the fact that coherence is eventually regained by the ring. For almost 2 years after crossing the ridge, the ring does not exhibit any sign of material decay, as successive short-term boundaries over this period fully shield

the ring (cf. Figure 5.4a). A compact region of closed SSH streamlines exists even when the ring has completely filamented (cf. Figures. 5.3a and 5.2f). As argued before, this is a manifestation of the ambiguity of Eulerian analysis in making mature coherence assessments, which is attributable to its observer dependence.

5.5 Concluding remarks

The continual emergence of short-term coherent material boundaries around the Agulhas ring unveiled in this work provides an objective (observer-independent) explanation for the extended stability (about 2 years) of the size of the ring as inferred by the probabilistic coherent set approach [Froyland et al., 2015]. These successive short-term boundaries prevent the mixing of the ring's interior with the ambient fluid, and mainly develop to the west of Walvis Ridge, which may be favored by the more quiescent environmental conditions there than in the Cape Basin [Schouten et al., 2000; Boebel et al., 2003]. Our results suggest that not all Agulhas rings decay as fast as argued in previous studies based on numerical simulations [van Sebille et al., 2010]. Whether the reported behavior is typical among all altimetry-derived material rings is yet to be determined. Also, the mechanism of the coherence regain described here and how this may influence coherent transport of Agulhas rings are unclear and deserve to be investigated.

An important question is how these results may affect those of Wang et al. [2015b] (Chapter 4) if they were extensible to all Agulhas rings. A quick computation reveals that material rings would carry yearly about 5 Sv of water across the South Atlantic. This rough estimate follows from assuming that the coherence response at the surface extends down to 2 km, the ring trapping depth for rings behaving as reported here, and that about 3 material rings with 150 km in diameter are formed annually, an estimate made by Wang et al. [2015b]. If we further assume that about half of the rings' contents

are traceable into the Indian Ocean, as is applicable to the ring investigated here, then the Agulhas leakage trapped in rings which is able to traverse the South Atlantic would amount up to 2.5 Sv. Overall, the transport results of Wang et al. [2015b] may be underestimated by one order of magnitude. Despite this the main conclusions of Wang et al. [2015b] remain unaltered because Eulerian annual ring transport estimates and Agulhas leakage estimates are still almost an order of magnitude bigger. On the other hand, there is large uncertainty around the behavior of the rings below the surface. For instance, according to numerical simulations [de Steur et al., 2004], the vertical structure of a ring may decay much faster than its surface signature. Moreover, Wang et al. [2015b] show that only a small fraction (less than 50%) of the water trapped inside material rings detected over the last two decades is traceable into the Indian Ocean. As a result, while Agulhas rings do provide a direct route for Agulhas leakage waters across the subtropical gyre, the majority of Indian Ocean waters are advected outside coherent rings by slower and more turbulent processes.

Chapter 6

Conclusions

The ability of Agulhas Current rings in transporting the Agulhas leakage across the South Atlantic has been debated over the past few decades. Most ring transport estimates in the literature are based on Eulerian criteria, the output of which either depends on choice of the reference frame, or fails to reveal long-term Lagrangian response of the flow field. In effect, even in simple analytical flows, a strong Eulerian eddy signal may mask the underlying hyperbolic structure truly controlling material evolution. As a result, fluid initially residing within the eddy may disperse fast while the eddy signal remains.

To objectively (i.e., in a frame-invariant fashion) identify and track oceanic eddies, geodesic eddy detection, a novel method rooted in nonlinear dynamical systems theory, is employed in this thesis. Geodesic eddy boundaries are sought as very special closed material curves which can neither stretch into nor break away from the eddy interior. In two-dimensional incompressible flows, geodesic eddy boundaries preserve their enclosed areas and nearly resume their initial arclength over the time interval they are detected, acting as impenetrable islands of minimal deformation in an otherwise turbulent field. This potentially enables them to preserve the concentration of non-passive

tracers for extended periods.

Using geodesic eddy detection, we have isolated highly coherent Agulhas rings capable of carrying fluid over long distances. Remarkably, some geodesic eddies show no visible sign of filamentation beyond their coherence time scales. By comparison, eddies uncovered by Eulerian methods and nonobjective Lagrangian diagnostics disperse quickly within weeks. The inconsistency of Eulerian signal coherence and Lagrangian deformation is critical to consider when quantifying eddy transport, as in the case of Agulhas rings executing the Agulhas leakage. Satellite observations of highly concentrated chlorophyll patches provided independent confirmation that geodesic eddies carry non-passive tracers over long distances.

To evaluate the validity of the widely accepted long-term transport view of Agulhas rings, we have extracted from geostrophic velocity fields derived from nearly two decades of satellite altimetry measurements coherent material eddies across the Agulhas corridor. These eddies contain material cores whose boundaries exhibit no noticeable sign of filamentation for up to one year. The transport by such material cores turns out to be smaller than earlier ring transport estimates. Although the choice of reference location where ring transport is evaluated (mid-Atlantic in our case) will cause discrepancy in the final results, we argue that previous studies inevitably overestimate ring transport by using Eulerian footprints in the altimetry dataset, which do not constitute the true material structures. The portion of Indian Ocean water annually carried within the coherent material eddies is also identified and found to be small compared to recent estimates of total Agulhas leakage based on numerical simulations. Even assuming that coherence is continually regained over time and these eddies possess a deep vertical structure in a long run, we find that Agulhas leakage trapped and transported by such eddies is still limited.

Material Agulhas rings tend to emerge spontaneously near the Walvis Ridge from rather incoherent water, most of which resides in the South Atlantic. This finding contradicts the widely accepted scenario in which Agulhas rings are shed directly from the Agulhas retroflection, but is more consistent with the fact that turbulent stirring within the Cape Basin is extremely strong, thereby constraining the emergence of material coherence. Successive coherence regain events occur when a material Agulhas ring traverses the Walvis Ridge and loses its initial coherence. This resolves the paradox between the conclusions on long-term evolution of Agulhas rings based on the geodesic eddy detection method and the coherent set approach. Most coherent material rings are found to cross the subtropical gyre and enter the Brazil Current eventually. However, only one ring consisting of mainly Indian Ocean water is seen to pour its contents on the North Brazil Current. This suggests that the contribution of coherent material Agulhas rings to the global thermodynamical budget by trapping the Agulhas leakage across the South Atlantic is not as significant as originally thought [Gordon and Haxby, 1990].

Geodesic eddy detection has been mostly applied to the South Atlantic in recent years [Beron-Vera, Wang et al., 2013; Haller and Beron-Vera, 2013; Wang et al., 2015a,b], yet is applicable to any region globally. Global assessments of transport of fluid and thermodynamic properties by mesoscale eddies have been a topic of rising interest in physical oceanography, yet latest assessments are invariably nonobjective [Chelton et al., 2011b; Dong et al., 2014; Zhang et al., 2014]. Given the shortcomings of Eulerian eddy criteria, these results are subject to question and thus should be revised.

Bibliography

- Arnold, V. I. (1973). *Ordinary Differential Equations*. Massachussets Institute of Technology.
- Arnold, V. I., Kozlov, V. V., and Neishtadt, A. I. (2006). Mathematical aspects of classical and celestial mechanics. In *Dynamical Systems III*, volume 3 of *Encyclopedia of Mathematical Sciences*, page 518. Springer-Verlag, Berlin Heidelberg, third edition.
- Batchelor, G. K. (1964). *An Introduction to Fluid Dynamics*. Cambridge University Press, Cambridge.
- Beal, L. M., de Ruijter, W. P. M., Biastoch, A., Zahn, R., and SCOR/WCRP/IAPSO Working Group 136 (2011). On the role of the Agulhas system in ocean circulation and climate. *Nature*, 472:429–436.
- Beron-Vera, F. J. (2015). Flow coherence: Distinguishing cause from effect. In Klapp, G., Chavarria, A. M. R., Ovando, A., Villa, L. L., and Sigalotti, D. G., editors, *Selected Topics of Computational and Experimental Fluid Mechanics*, Environmental Science and Engineering, Switzerland. Springer International Publishing.
- Beron-Vera, F. J., Olascoaga, M. J., Brown, M. G., and Koçak, H. (2012). Zonal jets as meridional transport barriers in the subtropical and polar lower stratosphere. *J. Atmos Sci.*, 69:753–767.
- Beron-Vera, F. J., Olascoaga, M. J., and Goni, G. J. (2008). Oceanic mesoscale vortices as revealed by Lagrangian coherent structures. *Geophys. Res. Lett.*, 35:L12603.
- Beron-Vera, F. J., Olascoaga, M. J., Haller, G., Farazmand, M., Triñanes, J., and Wang, Y. (2015). Dissipative inertial transport patterns near coherent Lagrangian eddies in the ocean. *Chaos*, 25:087412.
- Beron-Vera, F. J., Wang, Y., Olascoaga, M. J., Goni, G. J., and Haller, G. (2013). Objective detection of oceanic eddies and the Agulhas leakage. *J. Phys. Oceanogr.*, 43:1426–1438.

- Biastoch, A., Boning, C. W., Schwarzkopf, F. U., and Lutjeharms, J. R. E. (2009). Increase in Agulhas leakage due to poleward shift of Southern Hemisphere westerlies. *Nature*, 462:495–498.
- Blazevski, D. and Haller, G. (2014). Hyperbolic and elliptic transport barriers in three-dimensional unsteady flows. *Physica D*, 273-274:46–62.
- Boebel, O., Lutjeharms, J. R. E., Schmid, C., Zenk, W., Rossby, T., and Barron, C. (2003). The Cape Cauldron: a regime of turbulent inter-ocean exchange. *Deep-Sea Res. II*, 50:57–86.
- Byrne, D. A., Gordon, A. L., and Haxby, W. F. (1995). Agulhas eddies: A synoptic view using Geosat ERM data. *J. Phys. Oceanogr.*, 25:902–917.
- Chelton, D. B., Gaube, P., Schlax, M. G., Early, J. J., and Samelson, R. M. (2011a). The influence of nonlinear mesoscale eddies on near-surface oceanic chlorophyll. *Science*, 334:328–332.
- Chelton, D. B., Schlax, M. G., and Samelson, R. M. (2011b). Global observations of nonlinear mesoscale eddies. *Prog. Oceanogr.*, 91:167–216.
- Chelton, D. B., Schlax, M. G., Samelson, R. M., and de-Szoeke, R. A. (2007). Global observations of large oceanic eddies. *Geophys. Res. Lett.*, 34:L5606.
- Conti, C., Rossinelli, D., and Koumoutsakos, P. (2012). GPU and APU computations of Finite Time Lyapunov Exponent fields. *J. Comp. Phys.*, 231:2229–224.
- de Ruijter, W. P. M., Biastoch, A., Drijfhout, S. S., Lutjeharms, J. R. E., Matano, R. P., Pichevin, T., van Leeuwen, P. J., and Weijer, W. (1999). Indian-atlantic interocean exchange: Dynamics, estimation and impact. *J. Geophys. Res.*, 104:20,885–20,910.
- de Steur, L. and van Leeuwen, P. J. (2009). The influence of bottom topography on the decay of modeled Agulhas rings. *Deep-Sea Res. I*, 56:471–494.
- de Steur, L., van Leeuwen, P. J., and Drijfhout, S. S. (2004). Tracer leakage from modeled Agulhas rings. *J. Phys. Oceanogr.*, 34:1387–1399.
- Dencausse, G., Arhan, M., and Speich, S. (2010). Spatio-temporal characteristics of the Agulhas Current retroflection. *Deep Sea Res. I*, 57:1392–1405.
- Dencausse, G., Arhan, M., and Speich, S. (2011). Routes of Agulhas rings in the southeastern Cape Basin. *Deep-Sea Res. I*, 57:1406–1421.
- Doglioli, A. M., Blanke, B., Speich, S., , and Lapeyre, G. (2007). Tracking coherent structures in a regional ocean model with wavelet analysis: Application to Cape Basin eddies. *J. Geophys. Res.*, 112:C050432007.

- Doglioli, A. M., Veneziani, M., Blanke, B., Speich, S., and Griffa, A. (2006). A Lagrangian analysis of the Indian–Atlantic interocean exchange in a regional model. *Geophys. Res. Lett.*, 33:L14611.
- Dong, C., McWilliams, J. C., Liu, Y., and Chen, D. (2014). Global heat and salt transports by eddy movement. *Nature Comm.*, 5:3294.
- d’Ovidio, F., Monte, S. D., Penna, A. D., Cotté, C., and Guinet, C. (2013). Ecological implications of eddy retention in the open ocean: a lagrangian approach. *J. Physica A: Math. Theor.*, 46:254023.
- Early, J. J., Samelson, R. M., and Chelton, D. B. (2011). The evolution and propagation of quasigeostrophic ocean eddies. *J. Phys. Oceanogr.*, 41:1535–1555.
- Fang, F. and Morrow, R. (2003). Evolution, movement and decay of warm-core Leeuwin Current eddies. *Deep-Sea Res. II*, 50:2245–2261.
- Froyland, G., Horenkamp, C., Rossi, V., Santitissadeekorn, N., and Gupta, A. S. (2012). Three-dimensional characterization and tracking of an Agulhas Ring. *Ocean Modell.*, 52-53:69–75, 2012.
- Froyland, G., Horenkamp, C., Rossi, V., and van Sebille, E. (2015). Studying an Agulhas rings long-term pathway and decay with finite-time coherent sets. *Chaos*, 0:0–0.
- Froyland, G. and Padberg-Gehle, K. (2014). Almost-invariant and finite-time coherent sets: Directionality, duration, and diffusion. In Bahsoun, W., Bose, C., and Froyland, G., editors, *Ergodic Theory, Open Dynamics, and Coherent Structures*, volume 70 of *Springer Proceedings in Mathematics Statistics*, pages 171–216. Springer New York.
- Fu, L. L., Chelton, D. B., Le Traon, P.-Y., and Morrow, R. (2010). Eddy dynamics from satellite altimetry. *Oceanography*, 23:14–25.
- Garth, C., Gerhardt, F., Tricoche, X., and Hans, H. (2007). Efficient computation and visualization of coherent structures in fluid flow applications. *IEEE Trans. on Visualization and Computer Graphics*, 13:1464–1471.
- Garzoli, S. L., Richardson, P. L., Duncombe Rae, C. M., Fratantoni, D. M., Goni, G. J., and Roubicek, A. J. (1999). Three Agulhas rings observed during the Benguela Current Experiment. *J. Geophys. Res.*, 104:20971–20985.
- Goni, G. and Johns, W. (2001). Census of warm rings and eddies in the North Brazil Current retroflection region from 1992 through 1998 using TOPEX/Poseidon altimeter data. *Geophys. Res. Lett.*, 28:1–4.

- Goni, G. J., Garzoli, S. L., Roubicek, A. J., Olson, D. B., and Brown, O. B. (1997). Agulhas ring dynamics from TOPEX/POSEIDON satellite altimeter data. *J. Mar. Res.*, 55:861–883.
- Gordon, A. (1986). Interocean exchange of thermocline water. *J. Geophys. Res.*, 91:5037–5046.
- Gordon, A. L. and Haxby, W. F. (1990). Agulhas eddies invade the South Atlantic: Evidence from Geosat altimeter and shipboard conductivity-temperature-depth survey. *J. Geophys. Res.*, 95:3117–3125.
- Haller, G. (2001). Distinguished material surfaces and coherent structures in 3D fluid flows. *Physica D*, 149:248–277.
- Haller, G. (2005). An objective definition of a vortex. *J. Fluid Mech.*, 525:1–26.
- Haller, G. (2014). Lagrangian coherent structures. *Ann. Rev. Fluid Mech.*, 47:137–162.
- Haller, G. and Beron-Vera, F. J. (2012). Geodesic theory of transport barriers in two-dimensional flows. *Physica D*, 241:1680–1702.
- Haller, G. and Beron-Vera, F. J. (2013). Coherent Lagrangian vortices: The black holes of turbulence. *J. Fluid Mech.*, 731:R4.
- Haller, G. and Beron-Vera, F. J. (2014). Addendum to ‘Coherent Lagrangian vortices: The black holes of turbulence’. *J. Fluid Mech.*, 755:R3.
- Henson, S. A. and Thomas, A. C. (2008). A census of oceanic anticyclonic eddies in the Gulf of Alaska. *Deep-Sea Res. I*, 55:163–176.
- Isern-Fontanet, J., García-Ladona, E., and Font, J. (2003). Identification of marine eddies from altimetric maps. *J. Atmos. Oceanic Technol.*, 20:772–778.
- Jorba, À. and Simó, C. (1996). On quasi-periodic perturbations of elliptic equilibrium points. *SIAM J. Math. Anal.*, 27:1,704–1,737.
- Karrasch, D., Huhn, F., and Haller, G. (2014). Automated detection of coherent Lagrangian vortices in two-dimensional unsteady flows. *Proc. Royal Soc. A*, 471:20140639.
- Keating, S. R., Smith, K. S., and Kramer, P. R. (2011). Diagnosing lateral mixing in the upper ocean with virtual tracers: Spatial and temporal resolution dependence. *J. Phys. Oceanogr.*, 41:1512–1534.
- Knorr, G. and Lohmann, G. (2003). Southern Ocean origin for the resumption of Atlantic thermohaline circulation during deglaciation. *Nature*, 424:532–536.

- Le Bars, D., Durgadoo, J. V., Dijkstra, H. A., Biastoch, A., and de Ruijter, W. P. M. (2014). An observed 20-year time series of Agulhas leakage. *Ocean Sci. Discuss.*, 10:601–609.
- Le Traon, P. Y., Nadal, F., and Ducet, N. (1998). An improved mapping method of multisatellite altimeter data. *J. Atmos. Oceanic Technol.*, 15:522–534.
- Lehahn, Y., d’Ovidio, F., Lévy, M., Amitai, Y., and Heifetz, E. (2011). Long range transport of a quasi isolated chlorophyll patch by an Agulhas ring. *Geophys. Res. Lett.*, 38:L16610.
- Lugt, H. J. (1979). The dilemma of defining a vortex. In Muller, U., Riesner, K. G., and Schmidt, B., editors, *Recent Developments in Theoretical and Experimental Fluid Mechanics*, pages 309–321. Springer-Verlag.
- Lutjeharms, J. R. E. (2006). *The Agulhas Current*. Springer, Berlin.
- McWilliams, J. C. (1984). The emergence of isolated coherent vortices in turbulent flow. *J. Fluid Mech.*, 146:21–43.
- Mézic, I., S. Loire, V. A. F., and Hogan, P. (2010). A new mixing diagnostic and the Gulf of Mexico oil spill. *Science*, 330:486.
- Morrow, R., Birol, F., and Griffin, D. (2004). Divergent pathways of cyclonic and anti-cyclonic ocean eddies. *Geophys. Res. Lett.*, 31:L24311.
- Okubo, A. (1970). Horizontal dispersion of flotable particles in the vicinity of velocity singularity such as convergences. *Deep-Sea Res. Oceanogr. Abstr.*, 12:445–454.
- Olson, D. and Evans, R. (1986). Rings of the Agulhas Current. *Deep-Sea Res.*, 33:2742.
- Onu, K., Huhn, F., and Haller, G. (2015). LCS Tool: A computational platform for Lagrangian coherent structures. *J. Comp. Sci.*, 7:26–36.
- Ottino, J. (1989). *The Kinematics of Mixing: Stretching, Chaos and Transport*. Cambridge Texts in Applied Mathematics. Cambridge University Press, Cambridge.
- Peacock, T. and Dabiri, J. (2010). Introduction to Focus Issue: Lagrangian Coherent Structures. *Chaos*, 20:017501.
- Peacock, T., Froyland, G., and Haller, G. (2015). Introduction to focus issue: objective detection of coherent structures. *Chaos*, 25:087201.
- Peacock, T. and Haller, G. (2013). Lagrangian Coherent Structures: The hidden skeleton of fluid flows. *Phys. Today*, 66:41–47.

- Peeters, F., Acheson, R., Brummer, G., de Ruijter, W., Schneider, R., Ganssen, G., Ufkes, E., and Kroon, D. (2004). Vigorous exchange between the Indian and Atlantic oceans at the end of the past five glacial periods. *Nature*, 430:661–665.
- Pichevin, T., Nof, D., and Lutjeharms, J. R. E. (1999). Why are there Agulhas rings? *J. Phys. Oceanogr.*, 29:693–707.
- Provenzale, A. (1999). Transport by coherent barotropic vortices. *Ann. Rev. Fluid Mech.*, 31:55–93.
- Richardson, P. L. (2007). Agulhas leakage into the Atlantic estimated with subsurface floats and surface drifters. *Deep Sea Res. I*, 54:1361–1389.
- Ridgway, K. R. and Dunn, J. R. (2007). Observational evidence for a Southern Hemisphere oceanic supergyre. *Geophys. Res. Lett.*, 34:L13612.
- Rio, M.-H. and Hernandez, F. (2004). A mean dynamic topography computed over the world ocean from altimetry, in situ measurements, and a geoid model. *J. Geophys. Res.*, 109:C12032.
- Robinson, A. R., editor (1983). *Eddies in Marine Science*. Springer-Verlag.
- Rühs, S., Durgadoo, J. V., Behrens, E., and Biastoch, A. (2013). Advective timescales and pathways of agulhas leakage. *Geophys. Res. Lett.*, 40(15):3997–4000.
- Schouten, M. W., de Ruijter, W. P. M., and van Leeuwen, P. J. (2000). Translation, decay, and splitting of Agulhas rings in the southeastern Atlantic Ocean. *J. Geophys. Res.*, 105:21913–21925.
- Souza, J. M. A. C., de Boyer Montégut, C., Cabanes, C., and Klein, P. (2011a). Estimation of the Agulhas ring impacts on meridional heat fluxes and transport using ARGO floats and satellite data. *Geophys. Res. Lett.*, 38:L21602.
- Souza, J. M. A. C., de Boyer Montegut, C., and Le Traon, P. Y. (2011b). Comparison between three implementations of automatic identification algorithms for the quantification and characterization of mesoscale eddies in the South Atlantic Ocean. *Ocean Sci. Discuss.*, 8:483–531.
- Truesdell, C. and Noll, W. (2004). *The Non-Linear Field Theories of Mechanics*. Springer, New York.
- Turiel, A., Isern-Fontanet, J., and Garcia-Ladona, E. (2007). Wavelet filtering to extract coherent vortices from altimetric data. *J. Atmos. Ocean. Techn.*, 24:2103–2119.
- van Aken, H. M., van Veldhoven, A. K., Veth, C., de Ruijter, W. P. M., van Leeuwen, P. J., Drijfhout, S. S., Whittle, C. P., and Rouault, M. (2003). Observations of a young Agulhas ring, Astrid, during MARE in March 2000. *Deep-Sea Res. II*, 50:167–195.

- van Sebille, E. and van Leeuwen, P. J. (2007). Fast northward energy transfer in the Atlantic due to Agulhas rings. *J. Phys. Oceanogr.*, 37:2305–2315.
- van Sebille, E., van Leeuwen, P. J., Biastoch, A., and de Ruijter, W. P. M. (2010). On the fast decay of Agulhas rings. *J. Geophys. Res.*, 115:C03010.
- Wang, Y., Beron-Vera, F. J., and Olascoaga, M. J. (2015a). The life cycle of a coherent Lagrangian Agulhas ring. *In preparation*.
- Wang, Y., Olascoaga, M. J., and Beron-Vera, F. J. (2015b). Coherent water transport across the South Atlantic. *Geophys. Res. Lett.*, 42:4072–4079.
- Weijer, W., de Ruijter, W. P. M., Sterl, A., and Drijfhout, S. S. (2002). Response of the Atlantic overturning circulation to South Atlantic sources of buoyancy. *Glob. and Planet. Change*, 34:293–311.
- Weiss, J. (1991). The dynamics of enstrophy transfer in two-dimensional hydrodynamics. *Physica D*, 48:273–294.
- Zhang, Z., Wang, W., and Qiu, B. (2014). Oceanic mass transport by mesoscale eddies. *Science*, 345:322–324.